Alma Mater Studiorum · University of Bologna

School of Science
Department of Physics and Astronomy
Master Degree in Physics

ASSESSMENT OF THE REPEATABILITY AND STABILITY OF NODDI DIFFUSION MODELLING USING PHANTOMS AND IN-VIVO ACQUISITIONS

Supervisor:
Prof. Claudia Testa

Co-supervisor:
Dr. James Grist

Submitted by:
Mattia Ricchi

Academic Year 2022/2023

Abstract

MRI is a commonly used clinical tool for diagnosing, evaluating, and monitoring neurodegenerative diseases. One of the key contrast mechanisms in MRI is diffusion-weighted imaging (DWI), which measures the signal attenuation caused by water molecule displacement within brain tissues. This technique allows for the analysis of the brain tissue structure, specifically the white matter tracts where water diffusion aligns with the direction of the fibres. A new model called neurite orientation dispersion and density imaging (NODDI) has been proposed for characterizing brain tissue at a microscopic level. However, there is no gold standard for validating diffusion measures due to factors such as scanner type, scanning protocols, software methods, and observers. The aim of this work is to evaluate the repeatability and stability of NODDI diffusion modelling using phantoms and *in vivo* acquisitions. Phantoms and healthy volunteers are scanned multiple times on different days, and the acquired data is fitted to the NODDI model. The coefficient of variation is computed for phantoms to assess the consistency of the model over time, and the p-value of the paired t-test is calculated. The Bland-Altman analysis is performed for *in vivo* acquisitions to assess the stability and repeatability of NODDI over time. Results showed a great consistency of the NODDI metrics over time for both phantoms and *in vivo* acquisitions. The results also indicated stability even with magnetic field gradient coil heating, which can affect the acquired images and cause the model to not fit well. Additionally, the analysis showed that the hydration state of a healthy participant does not influence the outcome of the analysis. In conclusion, the proven stability of the NODDI model over time and under different acquisition conditions opens the way to several applications for clinical patients to study the effect and the progression of neurodegenerative diseases at a microscopic level.

Contents

List of Figures

List of Tables

Introduction

The technique of nuclear magnetic resonance (NMR) and especially its extension toward imaging, denoted as magnetic resonance imaging (MRI), is the most used clinical tool for non-invasive diagnosis, evaluation, and monitoring of neurodegenerative diseases. This advanced imaging technique relies on the use of strong magnetic fields, magnetic field gradients, and radio waves to generate detailed images of organs without the use of ionising radiation, setting it apart from CT and PET scans [1, 2]. Furthermore, it is more advantageous than traditional radiography and computed tomography (CT) due to its exceptional soft-tissue contrast and multi-planar capability. Magnetic resonance imaging has a wide range of contrast mechanisms that make it an extraordinary tool for diagnostic and research imaging. One of the key contrast mechanisms in MRI is the measurement of signal attenuation caused by water diffusion within brain tissues and structures.

Diffusion-weighted imaging (DWI) is an MRI technique that has become more commonly used as both a scientific and clinical tool over the past years. DWI relies on the diffusion properties of water molecules and allows for the exploration of the structure of the biological environment that is not visible through traditional MRI methods. In particular, DWI is used to visualise and analyse white matter tracts in which water diffusion aligns with the direction of fibres [3].

Currently, the gold standard metrics in diffusion analysis are fractional anisotropy (FA) and mean diffusivity (MD), also known as apparent diffusion coefficient (ADC). These metrics are obtained from the diffusion tensor model, a formalism introduced by Basser et al. [4, 5] to characterise diffusion anisotropy in the brain. FA is a measure of the degree of diffusion anisotropy, and MD describes the average diffusion [3]. Diffusion tensor imaging (DTI) measures water diffusion along different directions within tissues, particularly in the brain. It characterises the diffusion behaviour by fitting the diffusion tensor, a symmetric positive-defined 3×3 matrix, to the acquired data at each voxel in the MR image. To characterise water molecule diffusion within the brain tissues, fractional anisotropy and mean diffusivity can be obtained starting from the diffusion tensor.

The metrics of diffusion can be used for examining the condition of tissues at a microscopic level, specifically the white matter tracts in healthy brains and pathological conditions [4, 5]. Changes in FA and MD have been observed in various white matter diseases. For instance, a decrease in FA values and an increase in MD values can indicate a breakdown of tissue microstructure in white matter tracts [6]. Although these markers are characterised by great sensitivity, they are inherently non-specific [7]. For example, a decrease in FA could be caused by a decrease in neurite density, an increase in the dispersion of neurite orientation distribution, or other changes in tissue microstructure [8]. Therefore, changes in these statistics cannot be attributed to a specific change in the tissue microstructure.

Zhang et al. [8] proposed a new model to address the limitations of the tensor model and developed a clinically feasible technique for *in vivo* neurite orientation dispersion and density imaging (NODDI). This technique combines a three-compartment tissue model with a two-shell high-angular-resolution diffusion imaging (HARDI) protocol, which is optimised for clinical feasibility, to map neurite orientation dispersion and density *in vivo* [8]. In particular, the first implementation of the NODDI model uses the Watson distribution as the orientation distribution function, to characterise the neurite dispersion. NODDI imaging has been quickly adopted in the field of neuroimaging because it can measure changes in microstructures in both grey matter (GM) and white matter (WM) with an efficient imaging processing technique. However, one limitation of Watson-NODDI is that it cannot accurately model intricate neurite configurations that result from the fanning

and bending of axons. In these fibre configurations, the dispersion around the dominant orientation is highest in the plane of fanning and bending, but lowest in the plane perpendicular to it, causing anisotropic fibre dispersion [9].

Tariq et al. [9] introduced an extension to the NODDI formalism, using the Bingham distribution to characterise the neurite dispersion. The new model, the Bingham-NODDI, estimates the extent of dispersion about the dominant orientation, separately along the primary and secondary dispersion orientations, enabling the characterisation of anisotropic orientation dispersion [9].

Although quantitative DTI is a powerful tool for characterising brain tissue at a microscopic level, it is a relatively new method and has certain variables and limitations that need to be considered. There is limited understanding of the various factors that may influence the results of brain structure measurements, including hydration and blood pressure. Additionally, physiological changes can potentially interfere with the analysis results. For instance, age can impact both FA and MD values, and there may be slight variations throughout one's life, which may differ between genders [10]. Furthermore, there is a possibility that small changes in brain volume estimates caused by physiological factors such as dehydration, blood pressure, caffeine levels, and circadian rhythm could confound FA and MD values [11]. Accounting for physiological changes could significantly increase the sensitivity of future diffusion MRI studies and increase the reliability of serial measures using diffusion MRI.

In addition to that, there is yet no gold standard for validating diffusion measures, as they may vary depending on factors such as the type of scanner, scanning protocols, methods of the software and observers. Currently, only a limited number of studies have evaluated the reliability of DTI metrics using HARDI [12, 13]. Additionally, according to the literature, there is a lack of research examining the consistency and repeatability over time of NODDI fit results. As a result, it is crucial to thoroughly evaluate the typical fluctuations and consistency of the most used diffusion magnetic resonance measures [14]. Furthermore, there is currently no established protocol for preparing patients before undergoing a DTI brain scan. Specifically, further investigation is needed to clarify the impact of hydration on clinical study results, as it may affect the accuracy of findings, thereby reducing statistical power and increasing the need for many more patients to be scanned to detect a given effect size. This, in turn, increases the cost and time required to complete neuroimaging studies (such as to assess whether a new treatment is working) and so slows patient benefit from new therapies.

The purpose of this work is to evaluate the consistency and stability of DTI fit results over time, particularly in relation to FA and MD. In addition to FA and MD, the study also examines the NODDI (neurite orientation dispersion and density imaging) fit parameters, such as Orientation Dispersion Index (ODI), tissue volume fraction and intra-neurite volume fraction. These parameters are relevant indicators of the underlying microstructural features of brain tissue, and they can provide valuable insights into the pathophysiology of various neurological disorders.

To assess the repeatability of the results, the study employs two DTI phantoms that mimic restricted anisotropic diffusion in the brain, in particular in white matter. Each phantom is scanned four times on different days, and multiple times during the same day using the same scanner and the same acquisition protocol. After evaluating the repeatability of DTI fit results on the phantoms, a group of four healthy volunteers is scanned twice to verify the consistency over time of the results *in vivo*. The volunteers are scanned

using the same scanner and acquisition protocol as the phantoms. Lastly, a final analysis is conducted on a single healthy volunteer to determine whether their hydration level could impact the outcome. The volunteer undergoes two scans, one in a dehydrated state after abstaining from water overnight, and another after consuming water and waiting 10 minutes before rescan. By a final comparison of the results obtained in the two scans, it is possible to determine if the hydration level of the participant may influence the outcome of the study.

The thesis is structured as follows:

- Chapter 1 covers the basis and the principles of nuclear magnetic resonance and magnetic resonance imaging, together with an explanation of how the image is obtained and a brief overview of a clinical magnetic resonance imaging scanner.
- Chapter 2 provides a comprehensive overview of diffusion-weighted imaging, including an in-depth explanation of the tensor model, the process of acquiring diffusion-weighted images, and the correction of distortions. The chapter concludes by discussing the Bingham-NODDI model and its linear implementation, AMICO-NODDI.
- Chapter 3 contains a detailed description of the two phantoms used in the analysis. The chapter also provides a few details about the healthy volunteers. The second part of the chapter covers the explanation of the sequence acquisition used to acquire the diffusion-weighted images for both the phantoms and the healthy volunteers.
- Chapter 4 provides an explanation of the implementation of the software developed to analyse the acquired diffusion data. In particular, the chapter describes the implementation of the Bingham-NODDI and AMICO-NODDI models.
- Chapter 5 describes how the acquired data is processed and the metrics of interest are obtained. In particular, the last part of the chapter describes how the ROIs, from which the metrics are extracted, are created.
- Finally, Chapter 6 and 7 present the obtained results both in the case of the phantom study and in the *in vivo* study, and the influence that these results might have on future studies. Moreover, the last chapter also presents the hydration level study performed on a single healthy volunteer.

Chapter 1

Magnetic Resonance Imaging

MRI is a medical imaging technique that produces detailed 3D images of the human body without using ionising radiation. It is non-invasive and commonly used to detect illnesses, diagnose diseases, and monitor treatments. This advanced imaging method relies on the use of strong magnetic fields, magnetic field gradients, and radio waves to generate detailed images of organs without the need for X-rays or ionising radiation, setting it apart from CT and PET scans. MRI is based on the concept of nuclear magnetic resonance (NMR), that is a physical phenomenon in which nuclei in a strong, constant magnetic field are perturbed by a weak, oscillating magnetic field and respond by producing an electromagnetic signal with a frequency characteristic of the magnetic field of the nucleus.

In this chapter, the basic principles of MRI are treated. Detailed and advanced concepts can be found in *Foltz et al.* [2] and in *Haacke et al.* [1].

1.1 Physics of magnetic resonance imaging

MRI technology exploits the principle of nuclear magnetic resonance (NMR). This principle refers to a physical phenomenon in which nuclei within a strong, steady magnetic field B_0 are affected by a weaker, oscillating magnetic field B_1, that is perpendicular to the former.

For a nucleus to interact with the uniform magnetic field B_0, it needs to have an intrinsic nuclear magnetic moment and angular momentum, referred to as spin $\vec{I}$. This happens when an isotope contains an odd number of protons or neutrons. Hydrogen nuclei ^1H, made of one proton only, are largely used in clinical and research MRI as they generate a detectable radio-frequency signal and are naturally abundant in people and other biological organisms, especially in water and fat. Therefore, MRI scans primarily map the location of water and fat in the body.

A non-zero spin $\vec{I}$ is associated with a non-zero magnetic dipole moment $\vec{\mu}$ through the following relation (1.1), where γ is the gyromagnetic ratio, a constant characteristic of the given nucleus.

$$\vec{\mu} = \gamma \vec{I} \tag{1.1}$$

The nuclear spin is a type of angular momentum that is quantized. This means that the magnitude and components of this momentum can only take on certain values, which are restricted to integer or half-integer multiples of $\hbar$. The magnetic quantum number m is associated with the spin component along the z-axis of the applied magnetic field, and it

ranges in value from $+I$ to $-I$, in integer steps. For this reason, the z-component of the magnetic moment is simply:

$$\mu_z = \gamma m \hbar \tag{1.2}$$

The spin of a hydrogen nucleus is one-half, and it has two distinct spin states which are linearly independent. These states are commonly known as the spin-up state with $m = 1/2$ and the spin-down state with $m = -1/2$.

In the absence of a magnetic field, the two energy states are degenerate, meaning that they have the same energy. This leads to an almost equal number of nuclei existing in both states at thermal equilibrium. In other words, the magnetic moments of the hydrogen nuclei are distributed randomly and independently.
When a nucleus is exposed to an external magnetic field B_0, the two states no longer have the same energy due to the interaction between the nuclear magnetic dipole moment with the magnetic field. As explained in [2], the interaction energy of the nucleus is described by the Zeeman Hamiltonian, defined in Equation (1.3).

$$H_Z = -\frac{\gamma B_0 h I_z}{2\pi} \tag{1.3}$$

The eigenvalues of the Zeeman Hamiltonian are shown in Equation (1.4), and they represent the allowed values of energy for a free nucleus with spin quantum number I and gyromagnetic ratio γ, in the magnetic field B_0.

$$E_m = -\frac{\gamma B_0 h m}{2\pi} = -\gamma B_0 \hbar m \tag{1.4}$$

If a nucleus with spin 1/2 is found within a magnetic field B_0 along the z axis, the Zeeman interaction causes the nucleus's energy level to split into two new energy levels, as shown in Figure 1.1, with energy given by Equation (1.4). The Zeeman energy is also called the energy of spin interaction with the magnetic field. The energy levels are equally spaced because the consecutive values of m differ by 1 [2]. As a result, the different nuclear spin states have different energies in a non-zero magnetic field. In other words, the two spin states of a spin 1/2 can be seen as being aligned either with or against the external magnetic field. If γ is positive, then $m = 1/2$ is the lower energy state.

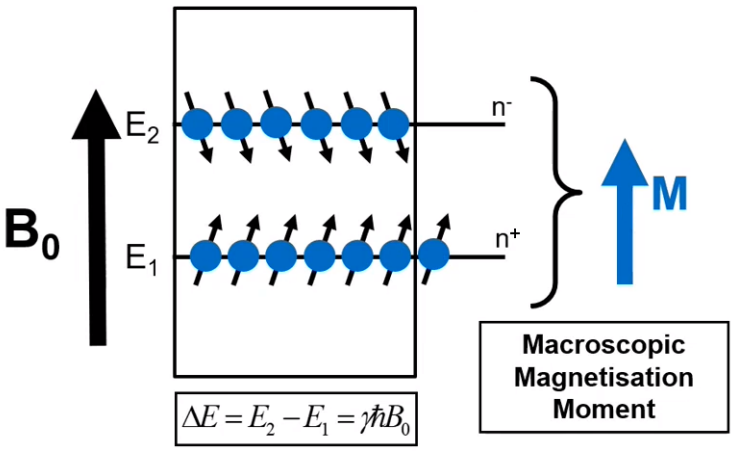

Figure 1.1: Zeeman levels of a nucleus with spin 1/2 caused by the interaction of the nuclear magnetic moment and the external magnetic field B_0.

From Equation (1.4), it can be easily calculated that the energy difference between neighbouring levels is given by:

$$\Delta E = \frac{\gamma B_0 h}{2\pi} = \gamma \hbar B_0 \tag{1.5}$$

As a general rule, the nuclei are distributed among energy levels based on the Boltzmann distribution, with the most populated levels being those with the lowest energy. This indicates that a larger number of spins will be found in the energy level of $m = 1/2$. Although it is quite small at room temperature, the difference in population between the two energy levels gives rise to a macroscopic quantity known as bulk magnetisation $\vec{M}$, which is the observable of the nuclear magnetic resonance phenomenon [15].

$$M_0 \propto \frac{\gamma^2 B_0}{K_B T} \tag{1.6}$$

As Equation (1.6) shows, the bulk magnetization $\vec{M}$, defined as the volume density of the spin magnetic moments, is aligned and proportional to the magnetic field and its intensity characterises the imbalance between the two spin populations.

A central concept in NMR is the precession of the spin magnetisation around the magnetic field at the nucleus, with the angular frequency given by the Larmour frequency:

$$\omega_L = \gamma B_0 \tag{1.7}$$

This indicates that every spin rotates in a cone around the direction set by the B_0 field with a frequency given by Equation (1.7), similar to how a tilted spinning top's axis precesses around the gravitational field, as shown in Figure 1.2.

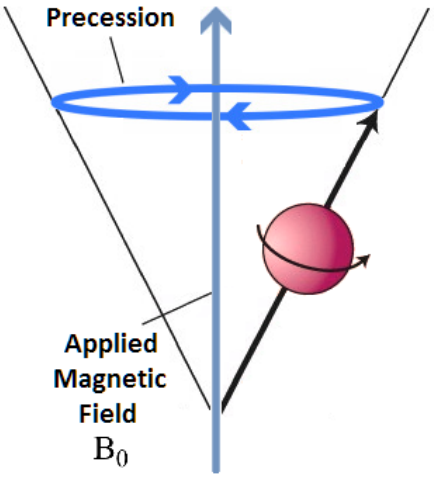

Figure 1.2: Precession of a ^1H nucleus about the applied magnetic field B_0.

Considering the macroscopic bulk magnetisation, the Bloch equation (1.8) expresses how $\vec{M}$ evolves in time.

$$\frac{d\vec{M}}{dt} = \gamma \vec{M} \times B_0 \hat{z} \tag{1.8}$$

In particular, Equation (1.8) describes how the macroscopic magnetisation interacts with the static magnetic field B_0. When the magnetisation is completely aligned with the direction of the magnetic field, there will be no effect due to the vector product. However,

if the magnetisation is tilted with respect to the direction of the B_0 field, it will begin to precess around the static magnetic field and the frequency of this precession will be given by the Larmor frequency from Equation (1.7).

When referring to the static magnetic field, its direction is known as the longitudinal axis, while the perpendicular plane is called the transverse plane. During thermal equilibrium, the magnetisation is aligned with the static magnetic field along the longitudinal axis due to the uncorrelated phases of the spin magnetic moments. However, detecting the magnetisation is challenging in this circumstance. The phenomenon of nuclear magnetic resonance can be used to measure the magnetisation. This was first observed by Rabi [16] and later characterised by Purcell and Bloch [15, 17] a few years later.

An oscillating magnetic field in the transverse plane, also known as the B_1 field or RF pulse, can disrupt the spin system. The B_1 field has a frequency within the radio frequency range and lasts for a specific period. If the B_1 field frequency matches the Larmor frequency of the spin system, it induces transitions between the Zeeman levels, perturbing the magnetisation $\vec{M}$ and tilting it away from its equilibrium towards the transverse plane.

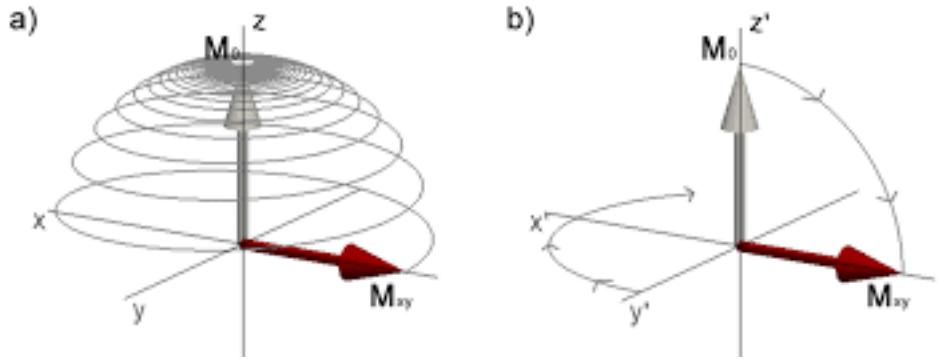

Figure 1.3: In (a), the net magnetization vector (M_{xy}) is shown precessing around the magnetic field after being tilted into the transverse plane. In (b), the same scenario is viewed from a rotating frame of reference.

Considering also the presence of the oscillating field B_1, Equation (1.8) becomes:

$$\frac{d\vec{M}}{dt} = \gamma\vec{M} \times (B_{1x}(t)\hat{x} + B_{1y}(t)\hat{y} + B_0\hat{z}) \tag{1.9}$$

Figure 1.3a, represents the result of the interaction between the magnetisation and the RF pulse in the transverse plane.

The same interaction can be described in the so-called rotating reference frame, which rotates in the transverse plane together with the B_1 field. In this case, B_1 will appear stationary and the effective longitudinal magnetic field will be zero. As a consequence, Equation (1.9) can be rewritten as:

$$\frac{d\vec{M}}{dt} = \gamma\vec{M} \times B_{1y}(t)\hat{y} \tag{1.10}$$

In Figure 1.3b, it can be seen that instead of precessing around $\hat{z}$, the magnetisation processes around $\hat{y}$, which is the direction of the RF wave in the rotating frame. By adjusting the magnitude and/or the duration of the RF, the flip angle α can be changed, which corresponds to the angle of the magnetisation tilt:

$$\alpha = \gamma B_1 t \tag{1.11}$$

Typical values for α are 90° and 180°.

After being excited, meaning tilted in the transverse plane, the magnetisation begins to return to its original state. This is known as relaxation and it restores the thermal equilibrium distribution of spins while building up the equilibrium magnetisation. The evolution in time of $\vec{M}$ can be described by the Bloch equation:

$$\frac{d\vec{M}}{dt} = \gamma\left(\vec{M} \times B_0\hat{z}\right) - \frac{M_x\hat{i} + M_y\hat{j}}{T_2} - \frac{M_z - M_0}{T_1}\hat{k} \tag{1.12}$$

Equation (1.12) illustrates how the bulk magnetisation evolves over time. This evolution is influenced not just by precession around the B_0 field, but also by the magnetisation's relaxation processes as it returns to its equilibrium state. There are two types of relaxation: longitudinal and transverse.

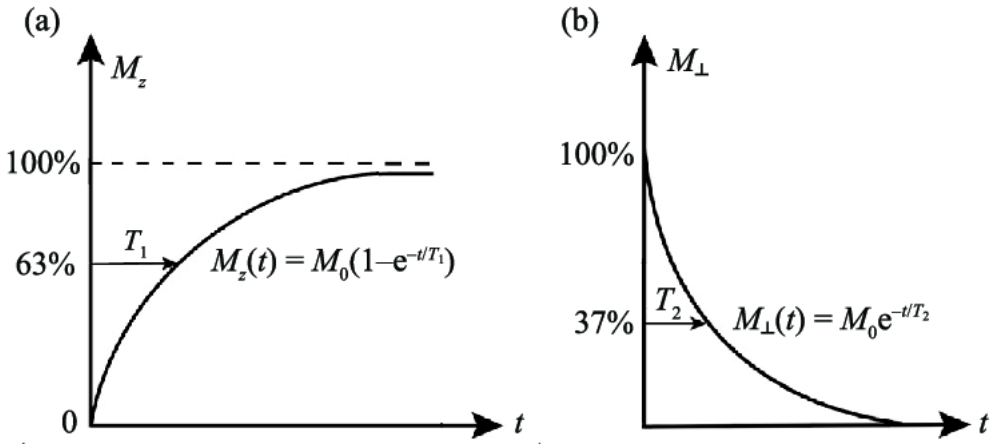

Figure 1.4: Diagram of the longitudinal (a) and transverse (b) relaxation. Image credit to *"Application of nuclear magnetic resonance technology in geologic carbon dioxide utilization and storage: A review"* [18].

Longitudinal relaxation, which is governed by the T_1 time constant, affects the longitudinal component of the magnetisation M_z. It is an energetic process that involves an exchange of energy between the spin system and the bulk. For this reason, it is also called spin-lattice relaxation. In particular, this process regulates the restoration of a group of nuclear spins to their original state of equilibrium in the direction of the external magnetic field. In contrast, transverse relaxation is controlled by the T_2 time constant and affects the transverse component of the magnetisation M_{xy}. It is an entropic process that arises from the loss of coherence of the spins in the transverse plane, caused by the interaction between adjacent spins. Therefore, transverse relaxation is the process by which nuclear spins reach thermal equilibrium among themselves.

With the Bloch equation (1.12), it is possible to compute both the longitudinal $M_z(t)$ and transverse $M_{xy}(t)$ magnetisation components in the rotating reference frame as a function of time. The components of the magnetisation over time are also shown in Figure 1.4.

$$\begin{cases} M_z(t) &= M_z(0)e^{-\frac{t}{T_1}} + M_0\left(1 - e^{-\frac{t}{T_1}}\right) \\ M_{xy}(t) &= M_0 e^{-\frac{t}{T_2}} \end{cases} \tag{1.13}$$

When the nuclear spins realign to the B_0 field, during their precession motion, they induce an electric signal that can be detected by a coil surrounding the sample. This signal is known as the Free Induction Decay (FID), and it is commonly observed in MRI experiments. The FID, shown in Figure 1.5, is a complex time-domain signal that contains information about the sample's nuclear properties and local environment. In MRI, the FID is used to create images by spatially encoding the signal and employing various reconstruction algorithms.

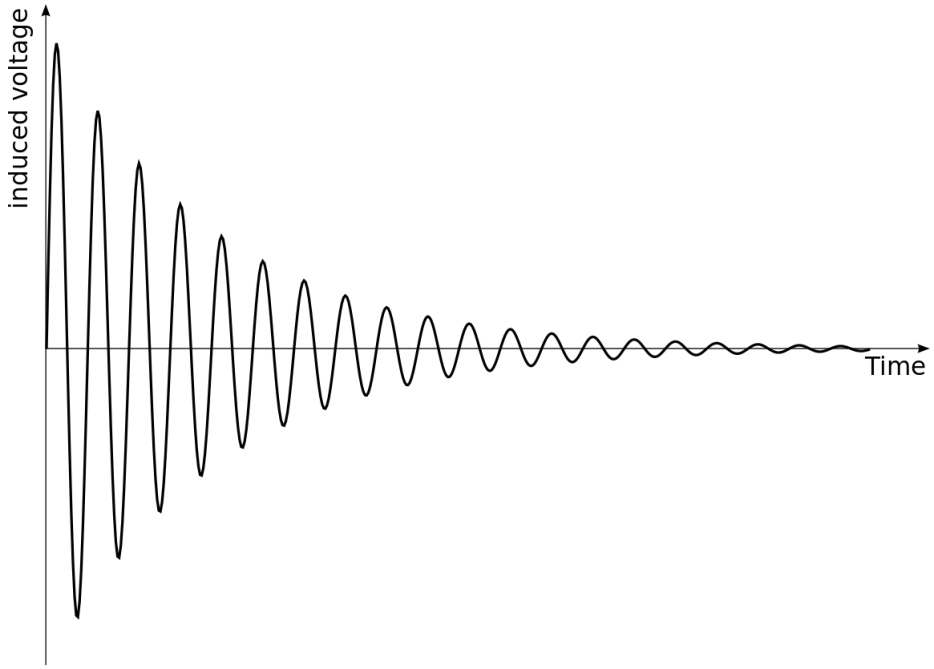

Figure 1.5: Example of the Free Induction Decay (FID). The signal is produced when the transverse magnetization returns to its original equilibrium state after a radio frequency pulse. This signal is used to gather important information in NMR and MRI experiments.

The relaxation times T_1 and T_2 are unique to each type of tissue, meaning that different tissues are characterised by different relaxation times. For example, the more complex and intricate the tissue, the quicker the longitudinal relaxation occurs. Figure 1.6 shows how white matter (WM), grey matter (GM) and cerebrospinal fluid (CSF) have different relaxation times. The image in Figure 1.6 a clearly shows that white matter and grey matter have a faster longitudinal relaxation than CSF. This difference in relaxation time can be used to create contrast in the final image, as faster relaxation means a higher signal is detected. As a result, in T_1-weighted images (images where the contrast is based on the difference in T_1 relaxation time), white matter will appear brighter than grey matter, which will appear brighter than CSF. T_1-weighted images provide good anatomical detail and are commonly used to visualize normal anatomy. An example of a T_1-weighted image is shown in Figure 1.7.

In the final image, the difference in the transverse relaxation time, denoted as T_2, can also determine the contrast between various tissues. Figure 1.6b shows that cerebrospinal fluid (CSF) has the longest T_2, making it appear very bright in a T_2-weighted image. In contrast, white matter will appear the darkest as it has a relatively fast spin-spin relaxation. An example of a T_2-weighted image is shown in Figure 1.7.

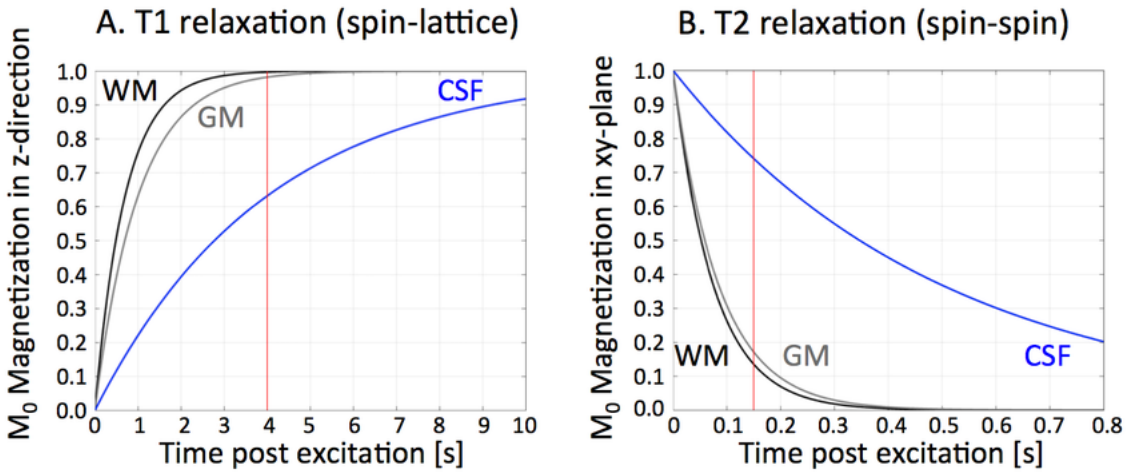

Figure 1.6: MRI uses different time constants (T_1 and T_2) to create relaxation curves for different tissues. This produces contrast between tissues, leading to clear images. The magnetisation represents the signal emitted from the tissues, and the red line shows the time point to receive the MRI signal. T_1 images show tissue-specific net magnetization in the z-direction, while T_2 images show net magnetisation rotating in the transversal (xy) plane. M_0 is the net magnetisation after the slice excitation. Image credit to [19].

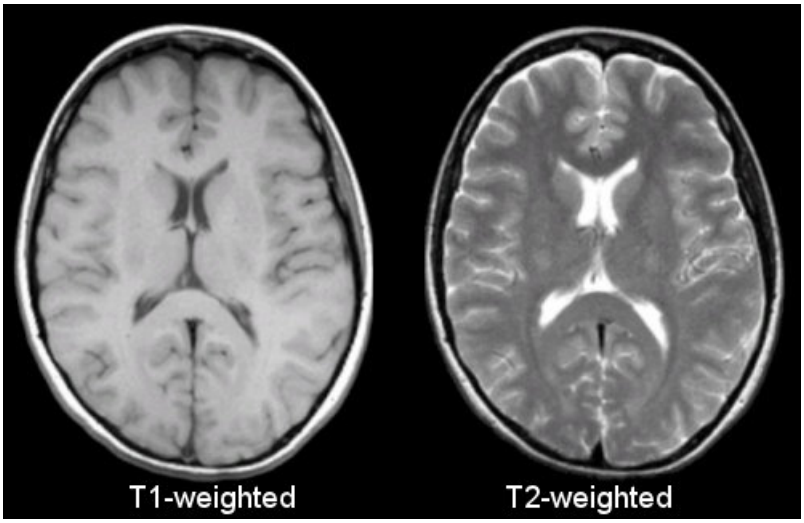

Figure 1.7: Example of T_1 (left) and T_2 (right) weighted images. Image taken from *"MRI Basics"* [20].

1.2 Spatial encoding

Spatial encoding in MRI is a fundamental principle that allows the reconstruction of images based on the spatial distribution of hydrogen spins within the body. This is achieved through the use of magnetic field gradients, in addition to the static magnetic field B_0 and the RF pulse B_1.

The magnetic field gradients cause the static magnetic field to change linearly in space, which affects the frequency with which the single spin precesses. From Equation (1.7) it is clear that the precession frequency of the single spin is proportional to the strength of the magnetic field B_0. If the B_0 field changes linearly within space, then the spins will

precess with different frequencies, depending on their position.

Considering a B_0 field and a magnetic field gradient applied along the $\hat{z}$ direction,

$$G_z = \frac{\Delta B_0}{\Delta z} \tag{1.14}$$

then, the magnetic field along $\hat{z}$ will be given by:

$$B_0(z) = B_0(0) + G_z \cdot z \tag{1.15}$$

Using Equation (1.15) to express the Larmor frequency in Equation (1.7), it becomes clear how the precession frequency changes linearly in space:

$$\omega(z) = \gamma \left(B_0(0) + G_z \cdot z\right) \tag{1.16}$$

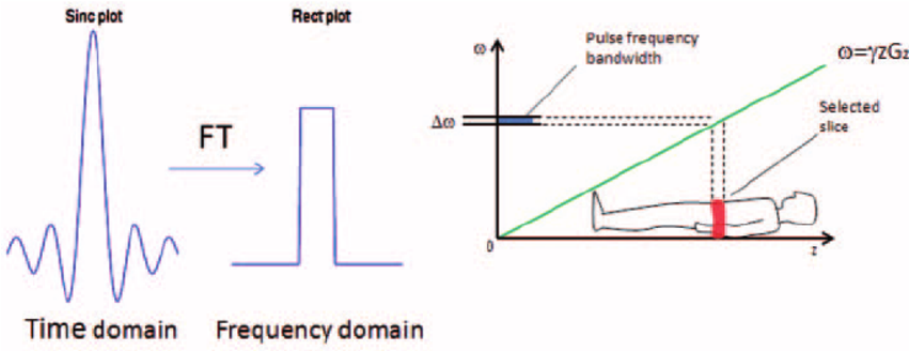

Figure 1.8: The slice selection technique: on the left, a rectangular frequency pulse is generated by a $sinc(t)$ time modulated pulse; on the right it is shown that the frequency pulse excites a slice of finite thickness in the patient's body. Image credit to [21].

The imaging technique known as Zeugmatography was first described by Lauterbur [22]. The term derives from Greek roots indicating the magnetic field gradient's role in connecting the RF magnetic field to a specific local spatial region via magnetic resonance. This relationship between the Larmor frequency and the position of the spins in space can be exploited to stimulate a thin plane along the $\hat{z}$ axis, rather than the entire brain volume. This specific plane of stimulation is commonly referred to as a "slice".

In general, the RF pulse is a magnetic field that oscillates over time. By using the Fourier transform (1.17), it becomes possible to acquire the frequency elements of the excitation pulse.

$$F(\omega) = \int_{-\infty}^{+\infty} f(t) e^{-2\pi i \omega t} dt \tag{1.17}$$

In particular, when considering a B_1 field with the shape of a sinc function, its Fourier transform will correspond to a boxcar function in the frequency domain, centred around $\omega(z^*) \pm \dfrac{\Delta\omega(z^*)}{2}$. This means that only spins with a Larmor frequency within the RF pulse's frequency range will be excited. Figure 1.8 shows that the RF pulse excites a slice with a finite thickness in the patient's body, and this thickness is related to the strength of the magnetic field gradient, also known as the slice selection gradient.

After selecting the slice, it is essential to encode the signal within it to obtain the brain's

volume image. This is accomplished using two gradients: the frequency and phase-encoding gradients.

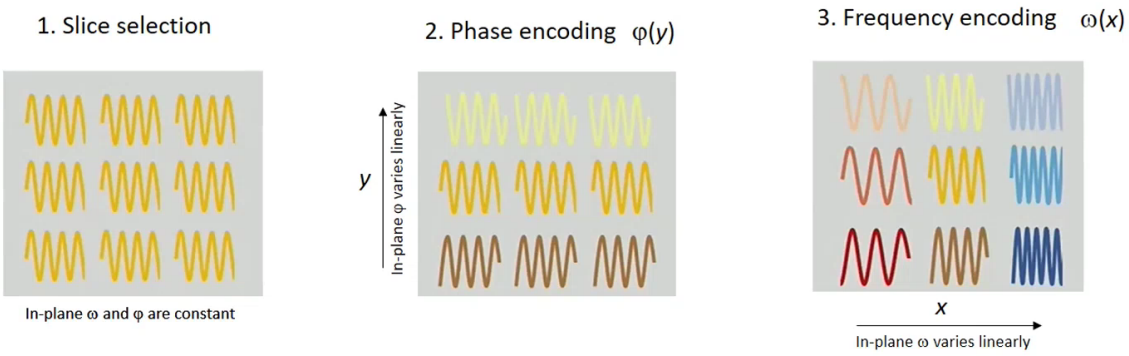

Figure 1.9: Space encoding procedure. First, the slice is selected by applying the slice selection gradient, typically along the $\hat{z}$ direction. Then, the signal within the slice is encoded by using the phase and frequency encoding gradients.

The frequency encoding gradient is applied along the direction of $\hat{x}$, causing the Larmor frequency to increase linearly in the same direction. As a result, an x-dependent Larmor frequency $\omega(x)$ is produced.
Similarly, the phase encoding gradient is applied along the $\hat{y}$ direction for a specific duration in time. Due to the varying magnetic field at different positions, the spins will exhibit different frequencies at different y locations. After the application of the pulse, the result is a y-dependent phase of the spins. In this way, each hydrogen nucleus can be distinguished from the others, allowing for the reconstruction of a map of the spins in space, resulting in the final image.

The Fourier transform (1.17) is used to encode the signal in space, meaning that the MR signal is acquired in the frequency domain. The vector $\vec{k}$ in Equation (1.18) relates reciprocal space and real space, with dimensions that are the inverse of a length.

$$\vec{k} = \frac{\gamma \vec{G}}{2\pi} t \tag{1.18}$$

Using the $\vec{k}$ formalism, each signal acquisition in time is represented by a point in $\vec{k}$-space. By applying magnetic field gradients, it's possible to move along the $\hat{k_x}$, $\hat{k_y}$, and $\hat{k_z}$ axes, ultimately sampling the entire reciprocal space. Finally, the reconstructed image of the scanned sample is obtained through an inverse Fourier transform, as illustrated in Figure 1.10.

1.3 Hardware of a clinical MRI scanner

A clinical MRI scanner is made up of several crucial components that allow for the acquisition of highly detailed images of the inner workings of the human body. Figure 1.11 shows a cutaway view of a standard clinical MRI scanner.

To make a clinical MRI scanner, the first essential component is the magnet. Its function is to create a static and uniform magnetic field called B_0. For medical purposes, the common B_0 values are $1.5\,T$ or $3\,T$, but they can be as high as $7\,T$. Higher field

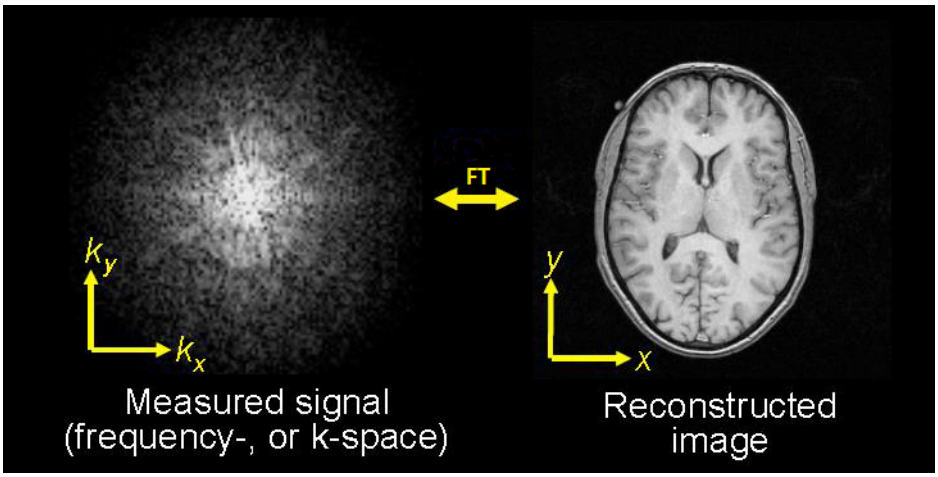

Figure 1.10: Example of signal acquired in the $\vec{k}$-space. The final image is reconstructed by the application of the Fourier transform to the acquired signal.

strengths provide better image quality and enable advanced imaging techniques. Therefore, a permanent magnet alone cannot serve the purpose. Generally, a superconducting electromagnet made of Niobium-titanium (Nb-Ti) is used to generate static magnetic fields with an intensity greater than $0.5\,T$.

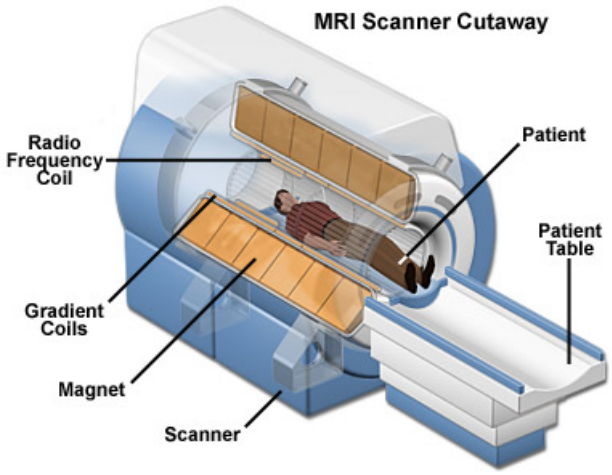

Figure 1.11: Schematic illustration of the MRI system that outlines the primary components.

Superconductors are materials that lose all electrical resistance when cooled below a critical temperature. This unique characteristic allows superconducting magnets to generate strong, uniform magnetic fields while operating with minimal energy loss. Additionally, they can sustain a steady magnetic field for extended periods of time.

The superconductive electromagnet in a clinical scanner is kept at a temperature of around $4\,K$ by being immersed in liquid helium. The scanner is designed with multiple layers to provide thermal insulation for the magnet. A layer of liquid helium surrounds the superconductive electromagnet, followed by a vacuum layer, and then another layer of liquid nitrogen to further enhance thermal shielding.

To create the necessary gradients of the B_0 field for spatial encoding of the signal within the envelope, multiple magnetic field gradient coils are utilized. These coils, as depicted

in Figure 1.12, are responsible for inducing changes in the static magnetic field along the primary spatial axes. By allowing the flow of high currents, the coils produce variations in the B_0 field, which change rapidly over time.

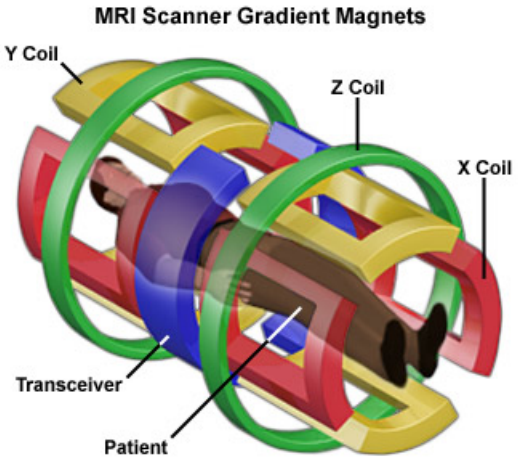

Figure 1.12: Schematic representation of the magnetic field gradient coils inside a clinical MRI scanner. Image credit to [23].

Due to the rapid change in the current flux, the magnetic field gradient coils in magnetic resonance imaging create noise. The intense current changes generate the Lorentz force, which causes the coils to move and produce noise. As the noise can be very loud, patients are usually provided with earplugs before the scan.

When a sample or patient is placed inside the scanner, it can cause variations in the B_0 field, which may lead to distorted images. To solve this issue, shim coils are placed within the scanner. These coils produce static magnetic fields to correct the local B_0 field and improve image quality.

Figure 1.13: RF coil used to scan the brain in a 3T scanner.

The final components of a clinical scanner are the RF coils. These coils play a crucial role in producing the excitation pulse to stimulate the magnetisation of the sample. They

also function as an antenna to detect and receive the MR signal emitted by the sample. Different RF coils are available for scanning different parts of the body, such as the head coil shown in Figure 1.13. To increase the detected signal intensity and improve the SNR, the coils must be placed as close as possible to the surface of the body, as the signal is acquired against thermal noise.

Chapter 2

Diffusion Weighted Imaging

Magnetic Resonance Imaging (MRI) has a wide range of contrast mechanisms that make it an exceptional tool for diagnostic and research imaging. One of the key contrast mechanisms in Magnetic Resonance Imaging is the measurement of signal attenuation caused by water diffusion within brain tissues and structures. Specifically, diffusion-weighted imaging (DWI) can be used to map and characterise the three-dimensional diffusion of water according to its spatial location [4].

Diffusion is a stochastic process that characterises the movement of particles or molecules, specifically water molecules, from one position to another over a given period. Water molecule diffusion is primarily caused by random thermal fluctuations. In three-dimensional space, the unrestricted isotropic diffusion, schematised in Figure 2.1, can be described by the Einstein diffusion equation:

$$D = \frac{\langle \Delta r^2 \rangle}{2n\Delta t} \tag{2.1}$$

In Equation (2.1), the diffusion coefficient D, typically expressed in units of square millimetres per second (mm^2/s), relates the average displacement of a molecule over an area to the observation time, with higher values of this constant indicating more mobile water molecules [24]. Equation (2.1) elucidates the direct proportionality between the diffusion coefficient D and the mean square displacement $\langle \Delta r^2 \rangle$, divided by the product of the number of dimensions n and the diffusion time Δt. This proportionality establishes a quantitative connection between the rate of diffusion and the extent of particle displacement over a given time period.

In the absence of boundaries, the molecular displacement of water is described by a Gaussian probability density function, as in Equation (2.2) [25].

$$P(\Delta r, \Delta t) = \frac{1}{\sqrt{(2\pi D\Delta t)^3}} \exp\left(\frac{-\Delta r^2}{4D\Delta t}\right) \tag{2.2}$$

Water diffusion occurs within, outside, around, and through cellular structures in biological tissues. As a result, the movement of water molecules is additionally influenced by interactions with cellular membranes and organelles. Specifically, cellular membranes impede the diffusion of molecules, leading to water following more intricate routes, thereby decreasing the average squared displacement. Furthermore, water within cells tends to encounter greater constraints imposed by cellular membranes, resulting in reduced diffusivity [25]. In general, the existence of membranes and organelles alters the observed

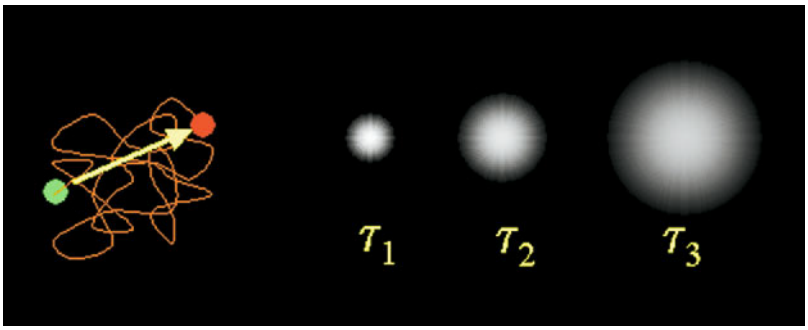

Figure 2.1: *Left*: Illustration of the diffusion random walk for a single water molecule from the green location to the red location. The displacement is indicated by the yellow arrow. *Right*: Diffusion describes the probability of displacement with time τ for a group or ensemble of water molecules. For short diffusion times, the predicted spread is compact but increases with longer diffusion times. Image credit to "*Diffusion Tensor Imaging of the Brain*" [25].

diffusion, referred to as the apparent diffusion coefficient (ADC).

Within the brain, neurons are organised primarily into two main tissue types: grey matter and white matter, each made of distinct components of the cell. Grey matter predominantly consists of neuronal cell bodies [26], indicating that diffusion in this tissue type is constrained by cell membranes but remains isotropic. White matter primarily consists of axons that extend from neuronal cell bodies, establishing connections with neurons in other regions of the brain. These axons are enveloped by a protective layer of glial cells [26], leading to a constrained diffusion of water molecules. Specifically, water diffusion is highly restricted and hindered in directions perpendicular to the fibres, but it is relatively unimpeded in the direction parallel to the fibre orientation [25]. Consequently, as shown in Figure 2.2, the diffusion of water molecules in white matter exhibits anisotropy, with a clear preference for diffusion aligned along the fibre orientation. This characteristic of anisotropy can be exploited to accurately map the spatial orientation of white matter pathways in the brain, assuming that the direction of the fastest diffusion reflects the overall alignment of the fibre tracts [27].

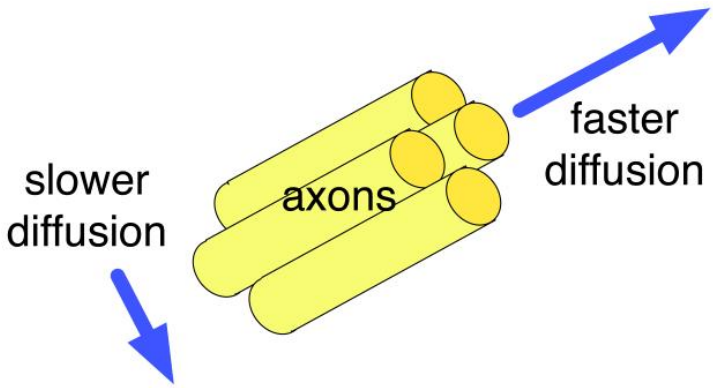

Figure 2.2: Illustration of anisotropic diffusion, in the ideal case of a coherently oriented tissue. This example compares the diffusion measured parallel and perpendicular to the axons in a white matter fibre tract. Image credit to *"An introduction to diffusion tensor image analysis"* [28].

2.1 Diffusion Tensor model

To characterise diffusion anisotropy in the brain, Basser et al. introduced the *diffusion tensor* formalism [4, 5]. With diffusion tensor imaging (DTI), diffusion anisotropy effects in diffusion MRI data could be fully extracted and characterised, providing new insights into tissue microstructure [29]. In the diffusion tensor model, diffusion is described by a multivariate normal distribution, shown in Equation (2.3).

$$P(\Delta\vec{r}, \Delta t) = \frac{1}{\sqrt{(4\pi\Delta t)^3 \left|\mathbf{D}\right|}} \exp\left(\frac{-\Delta\vec{r}^{\,T}\mathbf{D}^{-1}\Delta\vec{r}}{4\Delta t}\right) \tag{2.3}$$

In this equation, $\mathbf{D}$ represents the diffusion tensor, a 3×3 covariance matrix, defined in Equation (2.4), which describes molecular mobility along each direction and the correlation between molecular diffusion along these directions [29].

$$\mathbf{D} = \begin{pmatrix} D_{xx} & D_{xy} & D_{xz} \\ D_{yx} & D_{yy} & D_{yz} \\ D_{zx} & D_{zy} & D_{zz} \end{pmatrix} \tag{2.4}$$

The diagonal elements ($D_{ii} > 0$) are the diffusion variances along the axes x, y and z, while the off-diagonal terms are the covariances and are symmetric about the diagonal ($D_{ij} = D_{ji}$) [25]. In other words, each element of the diffusion tensor represents a diffusion coefficient along a particular axis: the diagonal terms of the diffusion tensor $\mathbf{D}$ represent the diffusion coefficients along the principal axes of diffusion, specifically along x, y and z; the off-diagonal terms of the diffusion tensor describe the cross-diffusion effects, or diffusion anisotropy, and provide additional information about the relationships between different diffusion directions.

The diffusion tensor can be diagonalised to establish a reference frame with axes that align with the principal directions of diffusion. As shown in Equation (2.5), diagonalising the diffusion tensor, the eigenvalues $(\lambda_1, \lambda_2, \lambda_3)$ and their corresponding eigenvectors $(\vec{V_1}, \vec{V_2}, \vec{V_3})$ are obtained, which depict the apparent diffusion coefficient along the principal diffusion axes and their directions.

$$\mathbf{D} = \begin{pmatrix} V_{1x} & V_{1y} & V_{1z} \\ V_{2x} & V_{2y} & V_{2z} \\ V_{3x} & V_{3y} & V_{3z} \end{pmatrix} \cdot \begin{pmatrix} \lambda_1 & 0 & 0 \\ 0 & \lambda_2 & 0 \\ 0 & 0 & \lambda_3 \end{pmatrix} \cdot \begin{pmatrix} V_{1x} & V_{2x} & V_{3x} \\ V_{1y} & V_{2y} & V_{3y} \\ V_{1z} & V_{2z} & V_{3z} \end{pmatrix} \tag{2.5}$$

Once diagonalised, the diffusion tensor can be represented as an ellipsoid [5]: the three perpendicular axes of the ellipsoid are aligned with the directions given by the eigenvectors, and their length is determined by the corresponding eigenvalues. An example of the diffusion ellipsoid is shown in Figure 2.3.

Diffusion is considered isotropic when all eigenvalues are nearly equal, that is, $\lambda_1 \approx \lambda_2 \approx \lambda_3$. On the contrary, the diffusion tensor is anisotropic when the eigenvalues are significantly different in magnitude, that is, $\lambda_1 > \lambda_2 > \lambda_3$.

In the central nervous system, water diffusion tends to exhibit greater anisotropy in white matter regions, while being more isotropic in both grey matter and cerebrospinal fluid (CSF). In regions of homogeneous white matter, the primary diffusion eigenvector $\vec{V_1}$, representing the direction of the most significant diffusion, is assumed to align parallel to the tract orientation, as shown in Figure 2.2.

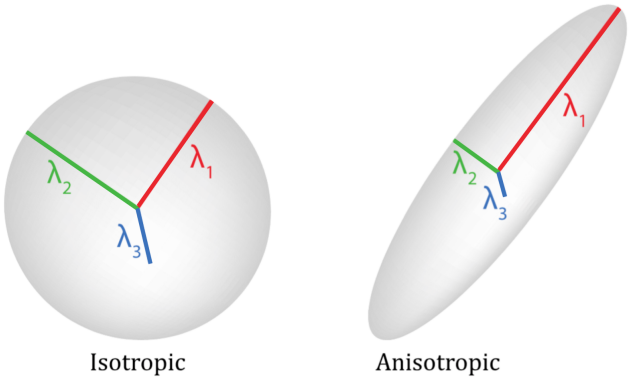

Figure 2.3: Graphical representation of the diffusion ellipsoid. On the left, the ellipsoid represents isotropic diffusion with $\lambda_1 \approx \lambda_2 \approx \lambda_3$. On the right, the diffusion tensor represents anisotropic diffusion with $\lambda_1 > \lambda_2 \approx \lambda_3$.

Numerous scalar indices have been proposed to quantify diffusion anisotropy and extract inherent structural information. Invariant indices are derived from combinations of the eigenvalues (λ_1, λ_2, and λ_3) of the diagonalised diffusion tensor [29].

The first scalar index that can be introduced is the *mean diffusivity* (MD) - also referred to as the apparent diffusion coefficient (ADC). It is calculated as the trace of the diffusion tensor divided by 3, which is equivalent to the average of the eigenvalues, as shown in Equation (2.6).

$$MD = \frac{Tr(\mathbf{D})}{3} = \frac{\lambda_1 + \lambda_2 + \lambda_3}{3} \tag{2.6}$$

The mean diffusivity (MD) is a measure of the overall diffusion magnitude within a voxel. It quantifies the average molecular motion of water in all directions and provides information about the overall diffusion characteristics, such as the extent of diffusion restriction or hindrance. On the other hand, MD does not provide any information about anisotropy or the directionality of diffusion.

Currently, the *fractional anisotropy* (FA) stands as the most extensively employed invariant measure of anisotropy. It was initially introduced by Basser and Pierpaoli [30] and has gained wide recognition in diffusion imaging studies.

$$FA = \sqrt{\frac{3\sum_{i=1}^{3}(\lambda_i - \langle\lambda\rangle)^2}{2(\lambda_1^2 + \lambda_2^2 + \lambda 3^2)}} \tag{2.7}$$

FA, defined in Equation (2.7), is a measure of the directionality or anisotropy of water diffusion within a voxel. It provides information about the coherence and organization of tissue microstructure. FA values range from 0 to 1, where 0 indicates isotropic diffusion, equal diffusion in all directions, and 1 indicates fully anisotropic diffusion, diffusion restricted to a specific direction [7]. Overall, MD and FA provide complementary information on tissue microstructure and can be used to characterise different types of tissues or pathological conditions in diffusion imaging studies. It is important to note that, while FA provides valuable insights into diffusion anisotropy, it does not fully describe the complete tensor shape or distribution. This is because various combinations of eigenvalues can produce identical FA values [31].

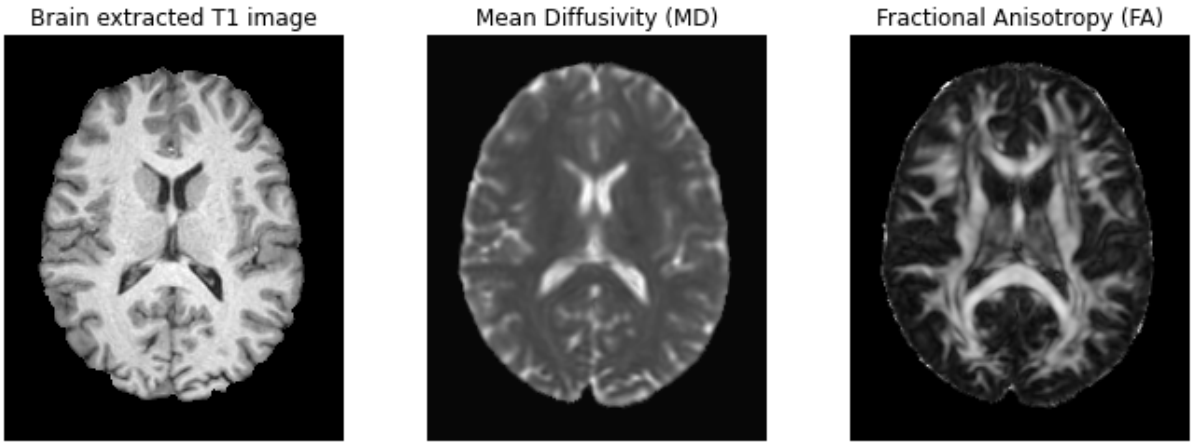

(a) Structural T1 image (b) MD map (c) FA map

Figure 2.4: Example of quantitative maps from a diffusion tensor imaging (DTI) experiment.

Figure 2.4 presents an example that includes maps of mean diffusivity (MD) and fractional anisotropy (FA), along with a structural T1-weighted image to be used as a reference. The mean diffusivity map, illustrated in Figure 2.4b, is displayed as a grey-scale image, where the intensity of each voxel reflects its corresponding mean diffusivity value in mm^2/s. In the MD map, cerebrospinal fluid (CSF) appears bright, indicating high diffusion due to its unrestricted movement. On the other hand, white matter appears dark, reflecting restricted diffusion caused by the presence of densely packed axonal fibres and myelin sheaths. It's worth noting that the MD map provides valuable insights into the microstructural properties of tissues. The bright appearance of CSF highlights its fluid nature and free diffusion, while the dark appearance of white matter indicates its organised structure with limited water diffusion.

Figure 2.4 also includes a map of fractional anisotropy (FA) as part of the example. The fractional anisotropy map, shown in Figure 2.4c, provides information on the directionality and coherence of water diffusion within tissues. In the FA map, each voxel's intensity represents the degree of anisotropy, ranging from 0 to 1. Higher FA values indicate greater directionality and alignment of water diffusion, often observed in regions with well-organized structures such as white matter tracts. Lower FA values suggest less directionality and more isotropic diffusion, commonly seen in regions with disorganized or heterogeneous tissue composition.

2.2 Diffusion-weighted image acquisition

To fully determine the diffusion tensor, it is necessary to collect diffusion-weighted images along several directions. The pulsed-gradient spin echo pulse sequence with a single-shot, echo-planar imaging (EPI) readout is widely recognised as the most common approach for diffusion-weighted imaging (DWI). The acquisition protocol is summarised in Figure 2.5.

The most simple arrangement of this pulse sequence consists of a slice selection gradient, a frequency and a phase encoding gradients, along with a pair of large-gradient pulses positioned on either side of the 180° refocusing pulse. The initial gradient pulse causes the

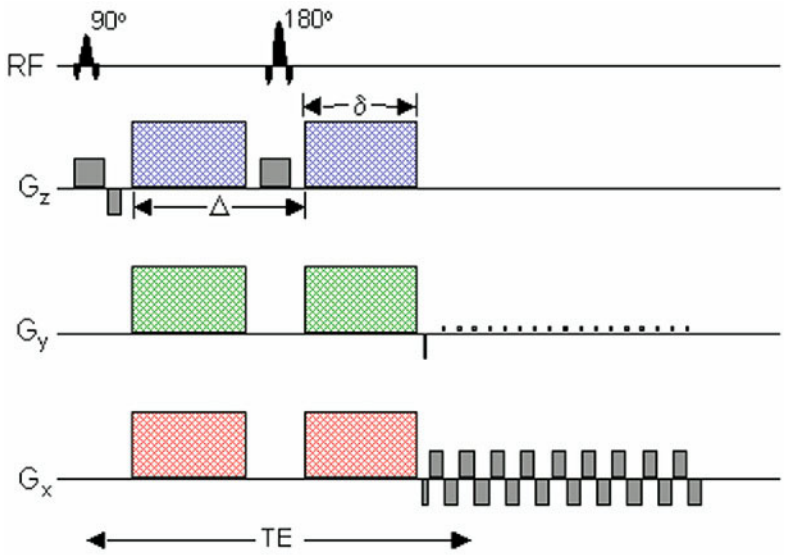

Figure 2.5: Schematic of a diffusion-weighted echo-planar imaging (DW-EPI) pulse sequence. A spin-echo is used to achieve diffusion weighting from the gradient pulse pairs (coloured). The imaging gradients are shown in grey. Diffusion weighting gradients can be applied in any arbitrary direction using combinations of G_x (red), G_y (green), and G_z (blue). Image credit to *"Diffusion Tensor Imaging of the Brain"* [25]

magnetisation to lose coherence throughout the sample, whereas the subsequent gradient pulse restores magnetisation coherence.

In the presence of gradient pulses, the loss of spin coherence varies depending on the position of the spin. When dealing with stationary molecules, the induced phases of both gradients cancel each other out completely. Consequently, the magnetisation of these molecules achieves optimal coherence, which leads to no signal attenuation. Conversely, in the case of coherent diffusion of molecules along the direction of the applied gradient, the bulk motion induces distinct phase changes for each pulse, as shown in Figure 2.6. As a result, the phases introduced by both gradients do not cancel out entirely, resulting in a net phase difference. The final phase difference will be proportional to the displacement, described by Equation (2.3), the amplitude of the diffusion gradients G, the duration of the diffusion gradients δ, and the time interval between the two gradients Δ, also called mixing time.
Therefore, when diffusion gradients are present, water molecules tend to accumulate in different phases. The MRI signals produced are directly related to the combined magnetisation of all water molecules within a voxel. Consequently, the dispersion of phases as a result of diffusion leads to signal attenuation.

$$S = S_0 \cdot e^{-bD} \tag{2.8}$$

The signal attenuation for diffusion gradient pulses in the case of simple isotropic Gaussian diffusion can be mathematically described by Equation (2.8). In this equation, S represents the diffusion-weighted signal, S_0 denotes the signal measurement obtained without applying any diffusion gradient, D corresponds to the apparent diffusion coefficient and b is referred to as the "b-value." The b-value, as defined in Equation (2.9), determines the sensitivity of the signal to diffusion [33].

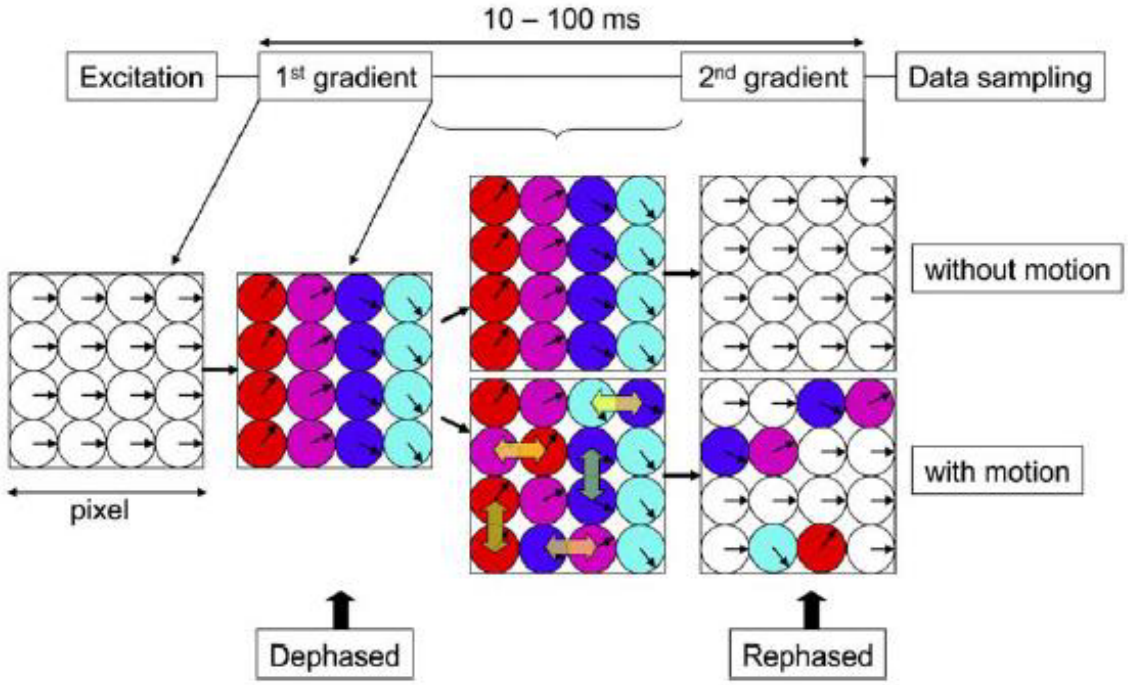

Figure 2.6: Schematic representation of diffusing spins. If spins diffuse during the time in between the two diffusion gradients, according to the principles of Brownian movement, the rephasing gradient will not lead to a realignment of the hydrogen atoms. Rather, they will be out of alignment in proportion to how much they have diffused in the time between the gradients, leading to a signal loss. Image credit to *"Principles of diffusion tensor imaging and its applications to basic neuroscience research"* [32].

$$b = (\gamma G \delta)^2 \cdot \left(\Delta - \frac{\delta}{3} \right) \tag{2.9}$$

The signal attenuation, as described in Equation (2.8), applies specifically to the isotropic Gaussian distribution and requires adjustments to accurately describe the signal attenuation for anisotropic diffusion involving the diffusion tensor. To account for anisotropic diffusion, the measured attenuation signal in each voxel, following the application of gradient j with direction $\mathbf{x}_j$ and b-value b_j, can be characterised using Equation (2.10) [4].

$$S_j = S_0 \exp\left(-b_j \mathbf{x}_j^T \mathbf{D} \mathbf{x}_j\right) \tag{2.10}$$

In Equation (2.10), the diffusion tensor $\mathbf{D}$ is a fundamental component that must be fully determined. To achieve this, a minimum of seven measurements are required, which involves the acquisition of multiple diffusion directions along with, at least, one unweighted ($b = 0$) image. This combination of measurements allows for accurate estimation and determination of the diffusion tensor, enabling a comprehensive characterisation of diffusion properties within the tissue of interest.

2.3 Distortions correction

Measurements of diffusion anisotropy can be susceptible to image noise, which can potentially introduce biases in the estimated anisotropy values. The inherent sensitivity of these measurements to noise can result in variations and inaccuracies in the quantification of diffusion anisotropy [34]. Moreover, the application of large diffusion weighting gradients in DW-MRI makes the technique highly sensitive to subject motion [35]. Any movement occurring during the acquisition can lead to severe image artefacts and distortions in the diffusion-weighted images, compromising the quality and reliability of the data.

The scan time can be shortened to reduce the influence of motion artefacts. An approach to achieve this is to use single-shot echo planar imaging (EPI) in diffusion-weighted MRI. EPI is a rapid imaging technique that acquires a complete readout of k-space in a single shot, allowing fast data acquisition [36]. By acquiring the diffusion-weighted images quickly, the likelihood of motion artefacts is reduced as there is less time for motion-related distortions to occur. However, it's important to note that shorter scan times can also introduce other challenges, such as field inhomogeneities at B_0 (especially at higher fields), and eddy-current induced distortions [37]. In DWI, the diffusion gradients used are typically longer compared to other MRI techniques. This increased gradient duration can lead to perturbations in the local magnetic field, which in turn can induce currents in the various conducting surfaces of the MRI scanner. These induced currents can cause image distortions, including contraction, overall shift, and shear, which are usually visually detectable [38]. Figure 2.7 shows an example of a DWI image.

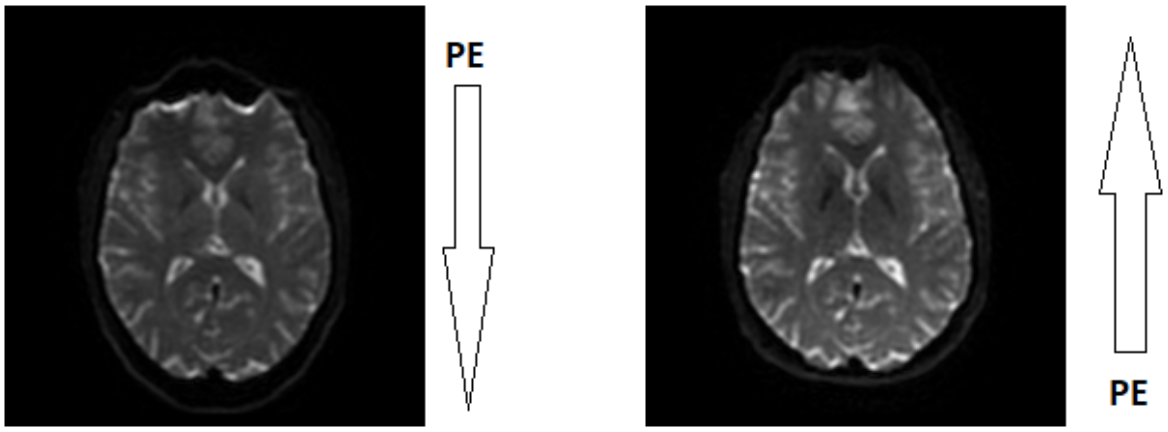

(a) Phase Encoding gradient AP (b) Phase Encoding gradient PA

Figure 2.7: Example of DWI images exhibiting notable distortions due to B_0 inhomogeneities. The image on the left displays compression of the frontal area, attributed to the application of a phase encoding gradient directed from the Anterior to the Posterior part of the brain. Conversely, the image on the right demonstrates elongation of the frontal area due to the application of a phase encoding gradient directed from the Posterior to the Anterior part of the brain.

As shown in Figure 2.7, the distortions in DWI images are clearly observed along the direction of the phase encoding gradient. This gradient plays a crucial role in spatial encoding and determines the location of each pixel in the image. Figure 2.7a illustrates an image acquired with a phase encoding gradient directed from the anterior to the posterior part of the brain. As a consequence, the frontal area appears compressed in the

final image. On the other hand, Figure 2.7b presents an image acquired with the opposite phase encoding gradient, resulting in an elongation of the frontal area in the final image. These observations highlight the impact of the phase encoding gradient on the spatial distortion characteristics of DWI images.

The presence of artefacts in DWI acquisitions can indeed introduce errors in tensor estimation, affecting the accuracy of derived diffusion maps such as fractional anisotropy (FA) and mean diffusivity (MD). These errors can subsequently lead to erroneous fibre reconstruction, affecting both the orientation and length of reconstructed fibres [38]. By implementing appropriate distortion correction methods, the accuracy and reliability of diffusion tensor estimation can be improved, leading to more accurate diffusion maps and more reliable fibre reconstruction.

As diffusion imaging is performed using diffusion-weighted spin-echo EPI, the most common artefacts affecting these images are the inhomogeneities of the B_0 field, typically caused by the susceptibility distribution of the subject's head (known as a susceptibility-induced off-resonance field), and eddy currents from the rapid switching of the diffusion weighting gradients.

To a first approximation, the susceptibility-induced field will be constant for all acquired images, implying that the set of images will be internally consistent. It is a problem because it will result in a geometric mismatch between the structural images (which are typically unaffected by distortions) and the diffusion image. TOPUP [39] is a method, implemented in FSL [40], for estimating the susceptibility-induced field. To estimate the susceptibility-induced off-resonance field, the TOPUP method uses two or more acquisitions with different acquisition parameters. The most common approach is to acquire two images with opposing polarities of the phase-encoding gradient. This way, the same field leads to distortions in opposite directions in the two acquisitions, as shown in Figure 2.7. Using these acquired images and known acquisition parameters, TOPUP aims to estimate the field by finding the field that, when applied to the two volumes, maximises the similarity of the unwarped volumes. The similarity is assessed by measuring the sum-of-squared differences between the unwarped images. By iteratively refining the field estimation, TOPUP aims to minimize the distortions caused by the susceptibility-induced off-resonance field.

Figure 2.8 shows an example of the output of TOPUP. In particular, Figure 2.8a shows the fieldmap image that represents the estimated susceptibility-induced off-resonance field. This field map provides information about the spatial variations in the field due to susceptibility effects. Figure 2.8b instead shows the unwarped (corrected) image, providing a corrected representation of the acquired data with reduced geometric distortions caused by the susceptibility field. In addition to these two images, TOPUP also generates coefficient maps that describe the voxel-wise mapping of the susceptibility field to the distortions observed in the acquired images.

To correct for eddy currents instead, one can use the tool EDDY [41], implemented by FSL [42]. Starting from the estimated fieldmap by TOPUP, EDDY estimates the eddy current-induced distortions and any potential subject motion that may have occurred during the DWI acquisition. The primary output of "eddy" is the corrected DWI dataset. This dataset comprises the original DWI volumes with the eddy current-induced distortions corrected. The correction aligns the volumes and reduces the artefacts, resulting in improved spatial accuracy and image quality. Figure 2.9 shows a comparison between the original diffusion-weighted image and the final EDDY-corrected image.

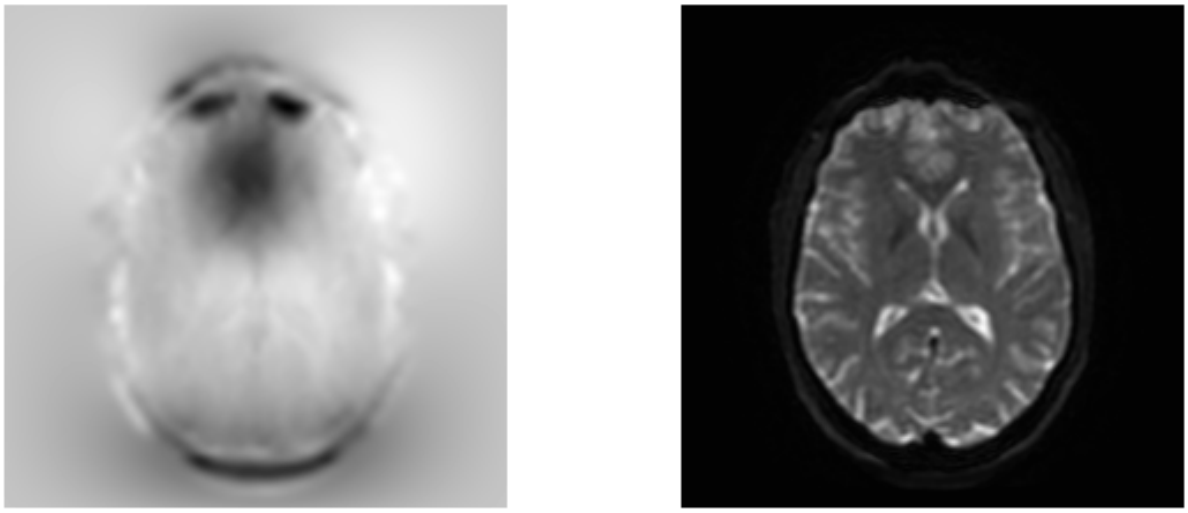

(a) TOPUP fieldmap (b) Unwarped image

Figure 2.8: Example of the output from TOPUP. The image on the left shows the fieldmap image that represents the estimated susceptibility-induced off-resonance field. The image on the right instead shows the unwarped (corrected) image, providing a corrected representation of the acquired data with reduced geometric distortions caused by the susceptibility field.

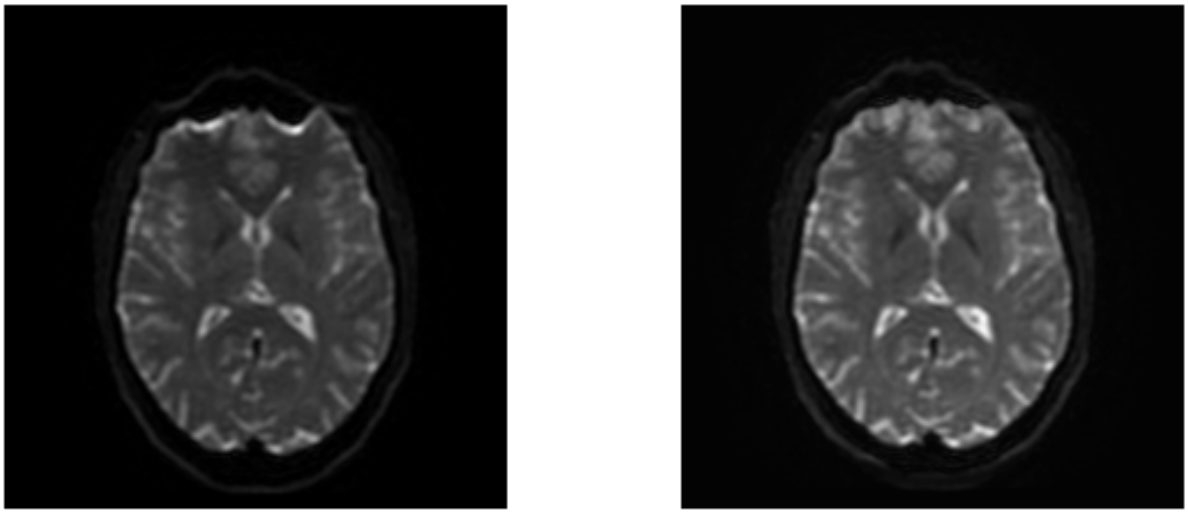

(a) Original DWI image (b) EDDY-corrected image

Figure 2.9: Comparison between the original DWI image and the corresponding eddy-corrected image.

2.4 Bingham NODDI model

Among all the different models proposed and used to fit the diffusion MRI data, Zhang et al. [8] introduced Neurite Orientation Dispersion and Density Imaging (NODDI), a clinically feasible diffusion MRI technique for estimating the microstructural complexity of dendrites and axons *in vivo* on clinical magnetic resonance scanners.

Dendrites and axons, the projections of neurons, are collectively known as neurites, and

their morphology is a key marker of brain development and ageing. Changes in the dispersion of the orientation or morphology of the neurites could indicate the emergence of neurological diseases such as multiple sclerosis [43] or Alzheimer's disease [44].

The NODDI model [8] is a two-level multi-compartment model, depicted in Figure 2.10, in which all compartments are considered non-exchanging.

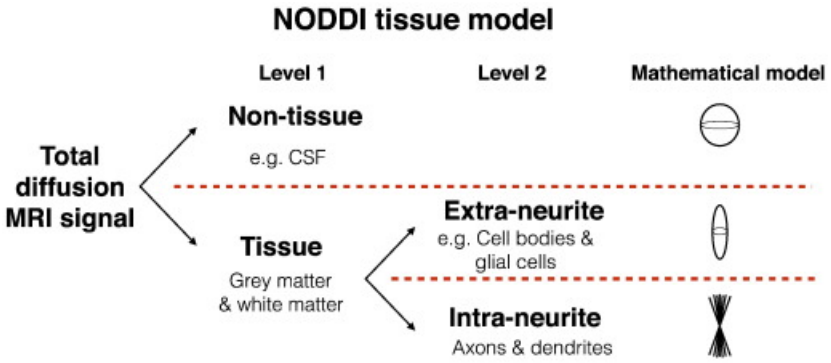

Figure 2.10: Breakdown of the total normalised diffusion MRI signal as modelled by NODDI. The contributions of the tissue and non-tissue components of the brain are modelled separately. The tissue signal is further broken down to account for the signal originating from the highly restricted neurites and the hindered space outside the neurites. The non-tissue compartment is modelled by isotropic Gaussian diffusion. The intra-neurite compartment models the neurites as orientationally dispersed sticks, while the space around the neurites is described an anisotropic diffusion model. Image credit to *"Bingham–NODDI: Mapping anisotropic orientation dispersion of neurites using diffusion MRI"* [9].

At the first level, the NODDI model distinguishes between the tissue and non-tissue components within the brain. The non-tissue compartment specifically represents the cerebrospinal fluid (CSF), which accounts for the freely diffusing water in the brain. This compartment is modelled as free isotropic Gaussian diffusion, with a diffusivity denoted as d_{iso}.

The second level of the NODDI model focuses on modelling the diffusion MRI signal originating from the tissue compartment, which includes both grey and white matter. Within the tissue compartment, a further breakdown is performed to capture the signal contributions from two distinct components: the highly restricted neurites and the hindered space surrounding the neurites. The intra-neurite volume fraction ν_{in} gives an estimate of the density of the neurites while, by construction, the extra-neurite volume fraction is $(1 - \nu_{in})$. Thus, the total normalised signal S is modelled as the signal contribution from the tissue and non-tissue components of the brain, weighted by their respective volume fractions, as in Equation (2.11) [8].

$$S = (\nu_{iso})\, S_{iso} + (1 - \nu_{iso})\, (\nu_{in} S_{in} + (1 - \nu_{in})\, S_{en}) \tag{2.11}$$

In Equation (2.11), S_{in} and ν_{in} are the normalised signal and volume fraction of the intra-neurite compartment; S_{en} is the normalised signal of the extra-neurite compartment; S_{iso} and ν_{iso} are the normalised signal and volume fraction of the CSF compartment [8].

Neurites are modelled in NODDI as sticks (cylinders with zero radius), taking into account the restriction of their membranes and their impact on the diffusion of water molecules

throughout their length [45]. During typical diffusion MRI experiments, water diffusion predominantly occurs along the longitudinal axis of neurites. Consequently, the diffusion signal arising from a neurite with a specific orientation $\hat{n}$ is characterised by the attenuation resulting from hindered diffusion along its length, parallel to the applied gradient direction.

$$S_{in} = \int_{\mathbb{S}^2} f(\hat{n}) e^{-bd_{\parallel}(\mathbf{q}\cdot\hat{n})^2} dn \tag{2.12}$$

To accommodate the orientational dispersion of the neurites, the signal originating from the intra-neurite volume fraction is calculated by summing this attenuation across all possible orientations, as expressed in Equation (2.12). In the equation, $\mathbf{q}$ and b represent the direction of the diffusion weighting gradient and the b-value, respectively. The term $f(\hat{n})dn$ denotes the probability of finding sticks orientated along the direction $\hat{n}$, while $e^{-bd_{\parallel}(\mathbf{q}\cdot\hat{n})^2}$ represents the signal attenuation resulting from the unrestricted diffusion along a stick with an intrinsic diffusivity of $d_{\parallel} = 1.7 \cdot 10^{-9}\ \frac{m^2}{s}$ and an orientation $\hat{n}$ [8, 46, 9].

The extra-neurite compartment refers to the space around the neurites, in which the diffusion of water molecules is hindered by the presence of neurites, but not restricted. Thus, it is modelled with Gaussian anisotropic diffusion [8].

$$\log S_{en} = -b\mathbf{q}^T \left(\int_{\mathbb{S}^2} f(\hat{n}) D(\hat{n}) dn \right) \mathbf{q} \tag{2.13}$$

Equation (2.13) defines the normalised signal of the extra-neurite compartment. In this equation, $D(\hat{n})$ is a cylindrical symmetric tensor with the principal direction of diffusion $\hat{n}$, diffusion coefficients $d_{\parallel}$ parallel to $\hat{n}$ and $d_{\perp} = d_{\parallel}(1 - \nu_{in})$ perpendicular to $\hat{n}$ [8].

When it was first introduced in [8], the NODDI model used the Watson distribution [47], Equation (2.14), as the orientation distribution function.

$$f(\hat{n}) = M\left(\frac{1}{2}; \frac{3}{2}; \kappa\right)^{-1} e^{\kappa(\boldsymbol{\mu}\cdot\hat{n})^2} \tag{2.14}$$

In Equation (2.14), M is a confluent hypergeometric function, $\boldsymbol{\mu}$ is the mean orientation and κ is the concentration parameter, which quantifies the degree of orientation dispersion about $\boldsymbol{\mu}$. The Watson distribution was chosen in [8] as the orientation distribution function in the NODDI model because it was considered the most straightforward distribution that may take into account orientation dispersion. The Watson distribution provides an appropriate representation for both cases of low orientation dispersion in highly coherent white matter and cases of large orientation dispersion in grey matter. As a result, it offers a flexible framework for simulating different tissue microstructures in diffusion MRI.

Despite its strengths, the Watson-NODDI model has a limitation in characterising complex neurite configurations, such as those involving fanning and bending axons [46]. This originates from the fact that the Watson distribution constrains the dispersion about the dominant orientation to be isotropic, as shown in Figure 2.11.
For fanning and bending axons, the dispersion about the dominant orientation is typically anisotropic: the dispersion is the highest along the plane of fanning and bending but the lowest perpendicular to the plane. This type of anisotropy cannot be characterised by the Watson-NODDI.

Tariq et al. [46] proposed a new NODDI model that incorporates the Bingham distribution [47] as the orientation distribution function, to enable the quantification of dispersion

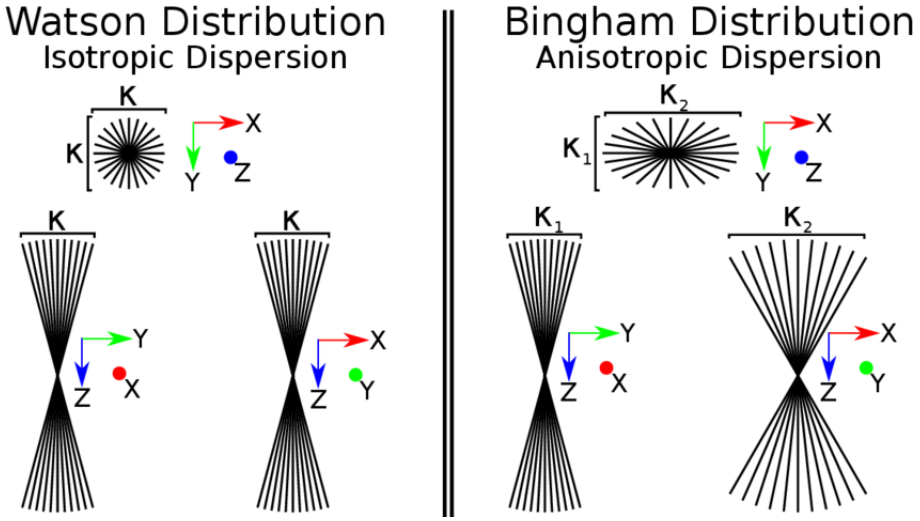

Figure 2.11: Schematic representations of Watson and Bingham distributions of sticks. Watson models isotropic dispersion and is a particular case of Bingham when concentration parameters $\kappa_1 = \kappa_2$. In the Bingham distribution instead $\kappa_1 > \kappa_2$. Image credit to *"Advanced dMRI Signal Modeling for Tissue Microstructure Characterization"* [48].

anisotropy of neurites. As shown in Figure 2.12, because Watson is a particular case of the Bingham distribution, the Bingham-NODDI provides an important alternative to overcome the isotropic dispersion limitation of the Watson-NODDI model. Unlike the Watson distribution, the Bingham distribution can capture anisotropic orientation dispersion at several levels as well as isotropic dispersion. As a result, a wider range of microstructural characteristics in neurite configurations can be efficiently modelled.

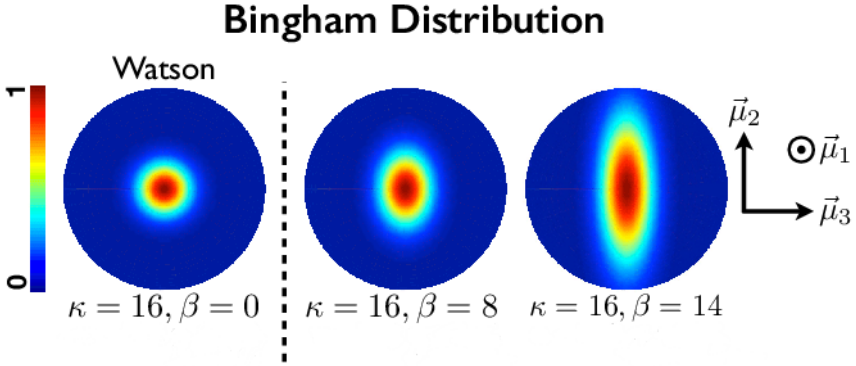

Figure 2.12: Probability density plots for Bingham distribution. From left to right, increasing dispersion anisotropy about the dominant orientation $\boldsymbol{\mu}_1$. The primary dispersion orientation, $\boldsymbol{\mu}_2$, represents the orientation of dispersion anisotropy about $\boldsymbol{\mu}_1$. Watson is a special case of Bingham distribution. Image credit to *"In vivo Estimation of Dispersion Anisotropy of Neurites Using Diffusion MRI"* [46].

The Bingham distribution is the spherical analogue of a two-dimensional Gaussian distribution. The probability density of orientation along a direction $\hat{n}$ for the Bingham distribution is defined in terms of a symmetric matrix 3×3 $\mathbf{B}$ [9], as in Equation (2.15) where c_B is the normalisation constant.

$$f(\hat{n};\mathbf{B}) = \frac{1}{c_B} e^{\left(\hat{n}^T \mathbf{B} \hat{n}\right)} \tag{2.15}$$

A more intuitive definition of the Bingham distribution can be obtained by diagonalising the tensor $\mathbf{B}$ [9], as done in Equation (2.16).

$$\mathbf{B} = \begin{pmatrix} \hat{\mu}_1 & \hat{\mu}_2 & \hat{\mu}_3 \end{pmatrix} \cdot \begin{pmatrix} \kappa_1 & 0 & 0 \\ 0 & \kappa_2 & 0 \\ 0 & 0 & \kappa_3 \end{pmatrix} \cdot \begin{pmatrix} \hat{\mu}_1^T \\ \hat{\mu}_2^T \\ \hat{\mu}_3^T \end{pmatrix} \tag{2.16}$$

In this equation, the diagonal terms reflect the concentrations of orientations about the principal axes, $\hat{\mu}_1$, $\hat{\mu}_2$ and $\hat{\mu}_3$, as shown in Figure 2.12, with $\kappa_1 > \kappa_2 > \kappa_3$ [9].

The Bingham distribution is invariant to the addition of an arbitrary constant to its eigenvalues [47]. By choosing $-\kappa_3$ as the arbitrary constant, Equation (2.15) can be rewritten as in Equation (2.17), where $\kappa = \kappa_1 - \kappa_3$ and $\beta = \kappa_2 - \kappa_3$.

$$f(\hat{n};\mathbf{B}) = \frac{1}{c_B} \exp\left(\kappa \left(\hat{\mu}_1 \cdot \hat{n}\right)^2 + \beta \left(\hat{\mu}_2 \cdot \hat{n}\right)^2\right) \tag{2.17}$$

In Tariq et al. [9], A more intuitive description of the orientation distribution is derived by rewriting Equation (2.15) in a form that is analogous to the two-dimensional Gaussian distribution, obtaining the function written in Equation (2.18).

$$f(\hat{n};\mathbf{B}) = \frac{e^{\kappa}}{c_B} \exp\left(-\frac{\left(\hat{\mu}_2 \cdot \hat{n}\right)^2}{1/\left(\kappa - \beta\right)}\right) \exp\left(-\frac{\left(\hat{\mu}_3 \cdot \hat{n}\right)^2}{1/\kappa}\right) \tag{2.18}$$

In the given equation, $1/\left(\kappa - \beta\right)$ and $1/\kappa$ represent the dispersion about the dominant orientation $\hat{\mu}_1$, specifically along $\hat{\mu}_2$ and $\hat{\mu}_3$ respectively. These dispersion parameters can be seen as analogous to the variance parameters in a Gaussian distribution, and they are inversely proportional to the concentration parameters κ and β. In particular, since $\kappa \geq \beta$, the dispersion along $\hat{\mu}_3$ is either less than or equal to that along $\hat{\mu}_2$, as visually demonstrated in the density plot presented in Figure 2.12. Consequently, we refer to $\hat{\mu}_2$ as the primary dispersion orientation and $\hat{\mu}_3$ as the secondary dispersion orientation [9].

To quantify the dispersion characteristics of neurites using Bingham-NODDI, the Bingham distribution allows for the calculation of two Orientation Dispersion Indices (ODIs). These indices provide measures of dispersion along the primary dispersion orientation and the secondary dispersion orientation, respectively, shown in Equations (2.19) and (2.20).

$$ODI_P = \frac{2}{\pi} \arctan\left(\frac{1}{\kappa - \beta}\right) \tag{2.19}$$

$$ODI_S = \frac{2}{\pi} \arctan\left(\frac{1}{\kappa}\right) \tag{2.20}$$

Figure 2.12 illustrates that as the value of β increases while keeping κ constant, there is an increase in the anisotropic dispersion. Specifically, this leads to an increase in ODI_P, while ODI_S remains constant. Therefore, while the absolute values of ODI_P and ODI_S indicate the overall level of dispersion, the relative values of these indices serve as an indicator of dispersion anisotropy.

To estimate the overall orientation dispersion, Tariq et al. [9] observed that the overall spread, or dispersion, of a multivariate normal distribution can be quantified as the determinant of its covariance matrix, thus defining the index in Equation (2.21),

$$|\Sigma_{Bing}| = \sqrt{\left(\frac{1}{\kappa - \beta}\right)\left(\frac{1}{\kappa}\right)} \tag{2.21}$$

which can be mapped to a finite range giving a measure of total dispersion:

$$ODI = \frac{2}{\pi} \arctan\left(|\Sigma_{Bing}|\right) \tag{2.22}$$

The Orientation Dispersion Index (ODI), defined in Equation (2.22), can be used to characterise the degree of dispersion or alignment of neurite orientations within a voxel of brain tissue. It ranges from 0 to 1, where 0 indicates a perfect alignment of neurite orientations (such as in highly organised fibre bundles), and 1 indicates complete dispersion or isotropic diffusion (such as in regions with crossing or complex fibre configurations). The ODI can provide important information about tissue microstructure and can be used to extract properties such as fibre coherence, axonal packing density, and white matter integrity. Among other things, it can be used in various studies to investigate how the brain connects or to determine the effects of neurodegenerative diseases.

2.5 AMICO-NODDI model

Watson-NODDI is a microstructural diffusion-based modelling technique that is able to provide useful microstructural quantification with a relatively simple diffusion acquisition protocol. Despite its great potential for clinical feasibility, the model currently demands a significant amount of time to complete its fitting process. Daducci et al. [49] introduced the Accelerated Microstructural Imaging via Convex Optimisation (AMICO), in which they reformulated the NODDI model as a linear model. In this way, the fitting procedure was reduced from about 13 hours to 10 minutes, thus meeting real application demands.

The objective of AMICO-NODDI is to remodel Equation (2.11) as a system of linear equations as follows:

$$\mathbf{y} = \Phi\mathbf{x} + \eta \tag{2.23}$$

As explained in [49], Equation (2.23) includes three variables. The first variable, $\mathbf{y}$, represents the measured signal. The second variable, Φ, is a dictionary of pre-generated signals that can be combined in a linear manner to estimate the measurement $\mathbf{x}$. The third variable, η, accounts for any noise that may be present during the acquisition process.

In order to deal with signals arising from different compartments, Daducci et al. [49] partitioned the dictionary into the following two blocks:

$$\Phi_N = \left[\Phi_N^t | \Phi_N^i\right] \tag{2.24}$$

In Equation (2.24) Φ_N^i models the isotropic contribution to the signal, while Φ_N^t accounts explicitly for the coupled intra- and extra-cellular compartments in the tissue. Each column in Φ_N^t represents the signal attenuation that results from a micro-environment with a unique density and orientation dispersion of the axons. In the context of the AMICO-NODDI model, the dictionary terms Φ_N are referred to as "atoms". Each "atom" is a pre-generated signal that corresponds to a specific micro-environment with unique characteristics. These characteristics may include features like axon density and orientation

dispersion. The dictionary is constructed by generating a range of these pre-defined signals, each representing a potential microstructural configuration in the tissue.

As in Zhang et al. [8], the Watson distribution [47] is used to model the dispersion of white matter and the longitudinal diffusivity is set to $d_{\parallel} = 1.7 \cdot 10^{-3}\, mm^2/s$. On the other hand, Φ_N^i is used to describe the signal attenuation that comes from the isotropic compartment. Similar to Zhang et al.'s approach in [8], the intrinsic diffusivity is set to the standard *in vivo* value of $d_{iso} = 3.0 \cdot 10^{-3}\, mm^2/s$.

Having defined the linear dictionary, NODDI can be formulated as a convex optimization problem:

$$\arg\min_{x \geq 0} \frac{1}{2} \left\| \tilde{\Phi}_N \mathbf{x} - \mathbf{y} \right\|_2^2 + \lambda \left(\frac{1}{2} \|\mathbf{x}\|_2^2 \right) + \gamma \left(\|\mathbf{x}\|_1 \right) \tag{2.25}$$

Equation (2.25) shows that the classical Tikhonov regularization is used in conjunction with the $\mathcal{L}_1$ norm to enhance problem stability.

Daducci et al. [49] developed an optimization routine that consists of three steps. First, they estimate the volume fraction of the isotropic compartment ν_{iso} by solving Equation (2.25) without regularization (i.e., $\lambda = \gamma = 0$). Next, they remove the isotropic contribution to the dMRI signal by subtracting $\tilde{\Phi}_N^i \nu_{iso}$ from $\mathbf{y}$ and solving Equation (2.25) with regularization terms. This step identifies the smallest subset of atoms needed to represent the signal, but the fitted coefficients $\mathbf{x}$ are not directly usable as they tend to be biased due to the underestimation by the $\mathcal{L}_1$ norm. The final step involves debiasing the previously found solutions by solving Equation (2.25) again without regularization over the set of solutions already identified.

After following the procedure outlined above to determine the weights of specific atoms, the NODDI model parameters can be extracted using the following methods:

$$\nu_{ic} = \frac{\sum_{j=1}^{N_t} f_j \mathbf{x}_j^t}{\sum_{j=1}^{N_t} \mathbf{x}_j^t} \tag{2.26}$$

$$\kappa_{ic} = \frac{\sum_{j=1}^{N_t} \kappa_j \mathbf{x}_j^t}{\sum_{j=1}^{N_t} \mathbf{x}_j^t} \tag{2.27}$$

$$\nu_{iso} = \sum_{j=1}^{N_t} \mathbf{x}_j^t \tag{2.28}$$

The notation f_j and k_j is used to refer to the intra-cellular volume fraction and concentration parameter of the j-th atom in Φ_N^t, for $j \in \{1, \ldots, Nt\}$.

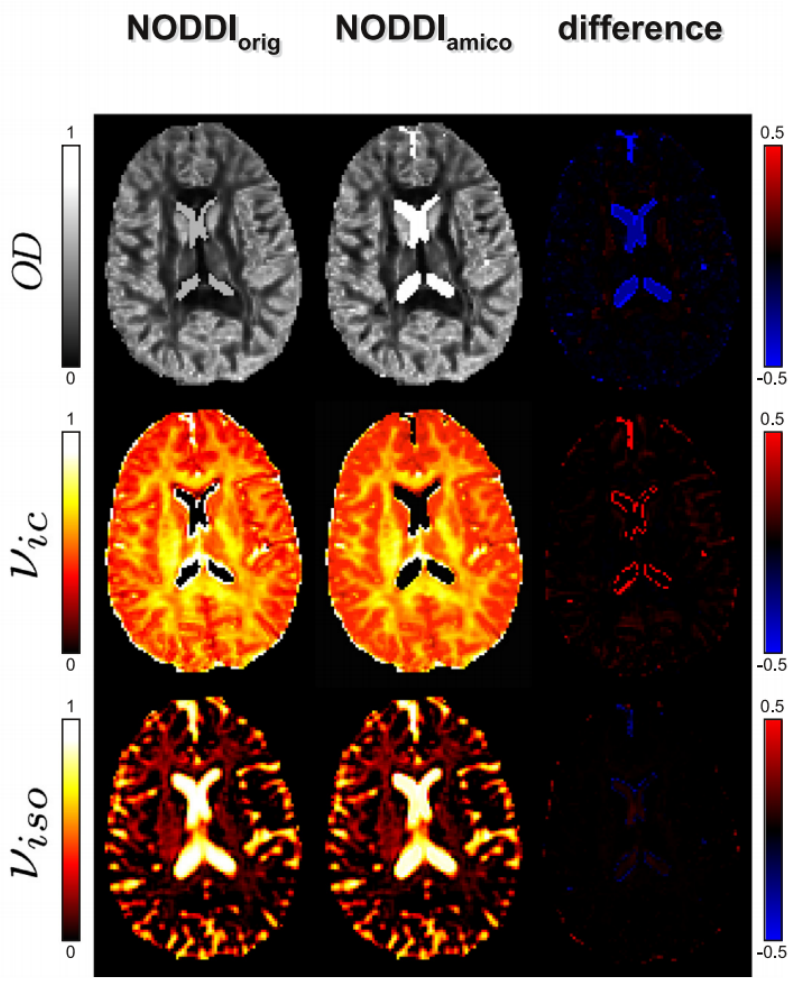

Figure 2.13: NODDI metrics compared for a healthy subject with both the original formulation and the AMICO linear framework. Near each parameter image, the difference map is shown. Image credit to *"Accelerated Microstructure Imaging via Convex Optimization (AMICO) from diffusion MRI data"* [49].

Materials and Methods

Chapter 3

Phantoms, subjects and sequence acquisition

This chapter presents a detailed description of the phantoms employed in the study.

Phantoms play an important role in this research as they enable the examination of diffusion outcomes without relying on healthy volunteers. This ensures that the results are not influenced by any physiological change that may occur in healthy volunteers, which could potentially impact the outcome of the analysis. These phantoms are designed to replicate the diffusion properties in brain tissue, particularly in white matter. If the study was successful, the phantoms could become an essential part of a calibration process of different MRI scanners.

Moreover, this study involves four healthy volunteers to look for the repeatability of the results also *in vivo*. The involvement of healthy volunteers in the study is crucial since it allows to evaluate the potential impact of physiological parameters on analytic outcomes, such as the participant's hydration level. These physiological factors may, in fact, affect the measurement results. A few details about the volunteers are presented in the second part of the chapter.

Finally, the last part of the chapter is dedicated to a detailed description of the MRI sequence used to acquire the images with the locally available 3 T GE Premier scanner at the Oxford Centre for Clinical Magnetic Resonance Research (OCMR).

3.1 DTI Phantoms

Two phantoms are used in this study to assess the consistency and stability of diffusion results over time. The phantoms, shown in Figure 3.1, are scanned several times on different days using the same scanner and acquisition protocol to evaluate the repeatability of the results. Moreover, the phantoms undergo multiple scans on the same day, with one acquisition after another, to investigate if the gradient heating affects in any way the results.

The first phantom used in the study is called the "basic phantom", shown in Figure 3.2a, and it was manufactured by the German Cancer Research Center, Heidelberg (DKFZ) [50]. It is composed of a fibre ring with uniform anisotropy at each position, which is embedded in a homogeneous medium. Specifically, the phantom is made by winding polyamide fibres around an acrylic plastic spindle. The fibres are made of a synthetic, extremely fine polyester fiberfill of diameter 15 μm. The polyfill is made of filament yarn,

Figure 3.1: Top vision of the DTI phantoms. On the left is shown the crossing phantom, with fibres crossing at 60°, while on the right is shown the basic phantom, with a single fibre ring mimicking restricted anisotropic diffusion.

specifically known as Filamentgarn TYPE 611. This type of yarn consists of continuous, long strands of polyester fibres, with a linear mass density of 50 decitex (dtex), indicating that 10000 meters of this yarn weigh 50 grams. Trevira GmbH, a company based in Bobingen, Germany, produces this polyfill. The fluid portion of the phantom is a mixture of distilled water and an aqueous sodium chloride solution (83 g NaCl per kilogram of water). This fluid constitution enables an orientation-independent and reliable use of DTI phantoms for evaluation purposes [50].

In Figure 3.2b, it can be observed that the outer fibre strand has a diameter of 60 mm and a thickness of 10 mm. Water is present between the fibres to simulate restricted anisotropic diffusion in the brain's white matter. The polyamide fibres winded around the plastic spindle are contained inside a cylindrical phantom container, shown in Figure 3.2a, of diameter 150 mm and height 150 mm. As per the information provided by the manufacturer [50], the phantom was crafted using an automatic winding machine. This machine ensured a constant rotation speed and controlled horizontal movement that resulted in an even distribution of the thread over the spindle's width. Additionally, a counter kept track of the total amount of thread used. The achieved fractional anisotropy is 0.78 ± 0.02.

The second phantom used in this work is the "Q-Ball phantom", also referred to as the "crossing phantom". This phantom is shown in Figure 3.3a and it was manufactured by Moussavi-Biugui et al. [51]. For the production of the phantom, polyfill fibres (50 dtex, consisting of several 15 μm fibres, Filamentgarn TYPE 611, Trevira GmbH, Bobingen, Germany) were wound on a spherical polyamide spindle. According to the manufacturer [51], phantom winding was performed using a semiautomatic winding machine driven by electric motors, and the guidance of the thread was performed manually. During the winding process, the fibre was passed through a solution containing 83 grams per litre of NaCl. This resulted in a better quality of the phantom compared to dry winding,

(a) (b)

Figure 3.2: (a) Picture of the basic phantom that shows the part in which the fibre bundle is contained and the liquid in which it is immersed. (b) detailed view of the plastic spindle, with the region of anisotropic diffusion highlighted in blue.

where the air between the fibres is removed in a fluid bath afterwards [51]. As shown in Figure 3.3b, the two fibre bundles cross each other at 60°. This way, the restricted diffusion in fibre crossing in the white matter of the brain can be modelled. As in the basic phantom, the spherical spindle is embedded in a fluid made of a mixture of distilled water and sodium chloride (83 g NaCl per kilogram of water). The concentration of NaCl was adapted to minimise the susceptibility difference between fluid and fibres and to eliminate orientation-dependent transversal relaxation times [51]. In Figure 3.3b, it can be observed that the spherical spindle has an outer diameter of 60 mm and the thickness of the two fibres is 10 mm. Additionally, Figure 3.3a shows that the cylindrical container has a diameter of 150 mm and a height of 150 mm.

The phantoms are scanned at the Oxford Centre for Clinical Magnetic Resonance Research (OCMR) - University of Oxford, using the locally available 21-channel head and neck coil (General Electric Healthcare, Waukesha, WI, USA), an example of which is shown in Figure 1.13. The phantoms are placed inside the head coil in such a way that the cylindrical container's axis is parallel to the B_0 field of the clinical scanner. Additionally, the part of the phantom that contains the fibres is positioned at the scanner's isocenter.

3.2 Healthy volunteers

As the aim of this study is to investigate the reliability of diffusion results, also obtained from *in vivo* scans, in order to evaluate the reproducibility of the diffusion results over time *in vivo*, four healthy volunteers are scanned along with the phantoms. Just as the phantoms, the participants are scanned with the same sequence acquisition and using the same 21-channel head and neck coil from GE (General Electric Healthcare, Waukesha, WI, USA), which can be observed in Figure 1.13.

This study also aims to assess whether the hydration state of participants can affect the outcome of diffusion analysis, as it is unknown if physiological factors like hydration could confound the results. An additional participant is scanned twice with the same scanner

(a)

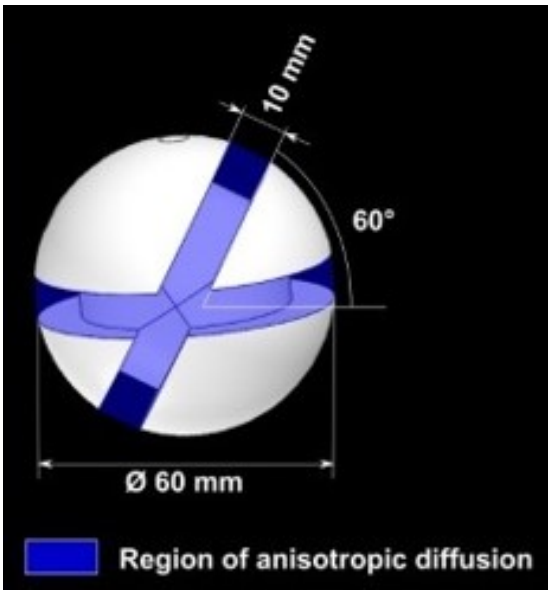

(b)

Figure 3.3: (a) Picture of the crossing phantom that shows the part in which the fibre bundle is contained and the liquid in which it is immersed. (b) Detailed view of the plastic ball spindle, with the region of anisotropic diffusion highlighted in blue.

and sequence as the phantoms and the other participants. The first scan is done after fasting and refraining from drinking water all night. The second scan is performed after drinking 500 mL of water and waiting for 10 minutes, right after the first scan.

The age range of the volunteers is 24 to 30, with three males and one female included in the study. The study involves University staff volunteers who have no prior experience with neurological or psychiatric illnesses. The ethics committee of the research centre approved the study, and each subject provided informed consent before undergoing scanning.

The phantoms and the healthy volunteers are all scanned with the same 3 T GE Premier (General Electric Healthcare, Waukesha, WI, USA) scanner, an example of which is shown in Figure 3.4. Specifically, the phantoms are scanned four times on different days within a month to determine the consistency of the results over time. Additionally, eight scans are conducted on the same day, one after the other, to investigate any potential magnetic field gradient coil heating effect on the results. The healthy volunteers, instead, are scanned twice on the same day. After each volunteer is scanned the first time, they are taken out of the scanner, given some time to move around the scan room, repositioned, and scanned again.

3.3 Sequence acquisition

The phantoms and the participants are scanned using the same 3 T GE Premier scanner (General Electric Healthcare, Waukesha, WI, USA) at the Oxford Centre for Clinical Magnetic Resonance Research (OCMR) - University of Oxford.

The DTI protocol for the phantoms consists of a single-shot, spin echo-based, and diffusion-weighted echo planar imaging sequence. The sequence includes a single refocusing pulse (180° pulse) with a repetition time (TR) equal to 6000 ms to allow for the acquisition of

Figure 3.4: Example of a GE 3 T scanner.

multiple slices during a single TR. The echo time (TE) is chosen to be 70.1 ms. Additionally, diffusion data is acquired with a multi-shell protocol, meaning data acquisition along various diffusion directions with different b-values to provide a comprehensive view of the diffusion process. Specifically, data acquisition is performed along 90 distinct diffusion directions with two corresponding b-values: 30 directions with a b-value = 1000 mm/s^2 and 60 directions with a b-value = 2600 mm/s^2. In addition, 9 $b = 0$ images are randomly dispersed in between the diffusion-weighted images. The inclusion of the $b = 0$ images is critical for the assessment of signal intensity in the absence of diffusion weighting and for the correction of artefacts due to B_0 inhomogeneities, eddy currents and subject movements. To improve acquisition efficiency without compromising image quality, an ASSET (Array Spatial Sensitivity Encoding Technique) factor of 2 is applied. This parallel imaging technique effectively reduces scan time allowing for the acquisition of more than one slice per excitation. Additionally, the field of view is set to 240×240 mm^2, with a matrix size of 96×96. The slice thickness is optimised at 2.5 mm with a total number of slices equal to 32, and a bandwidth of 250 kHz is employed. Furthermore, to enhance image quality, spectral fat saturation with non-spectral selective excitation is included in the sequence. This technique selectively suppresses fat signals, thus avoiding N/2 chemical shift ghosting artifacts which can cause the fat signal to appear displaced from its actual location, creating a duplication of structures and reducing image quality. Finally, the sequence is adapted to output the reversed polarity phase encode acquisition, which is a $b = 0$ volume acquired with the opposite phase encoding gradient direction compared to the diffusion-weighted volumes. This acquisition helps in the distortion correction step, in particular, the correction of artefacts due to the B_0 field inhomogeneities along the direction of application of the phase encoding gradient.

Imaging protocol for healthy volunteers includes a T1-weighted and a diffusion-weighted scan. After a subject is scanned with all MR sequences in a scan session, the subject leaves the scanner table and is then repositioned for the second scan session, where the

same sequences used in the first session are repeated. Whole-brain T1 weighted 3D volumes are acquired with a Magnetization Prepared RApid Gradient Echo sequence (MP-RAGE) with the following parameters: repetition time (TR) = 2584 ms, Inversion Time of 1058 ms, Echo Time (TE) = 2.9 ms, Pixel Bandwidth = 244 Hz, 80% Phase Field of View, Acquired and reconstructed Voxel Volume = 1 mm^3, Averages = 1, Flip angle = 8°, Field of view = 256 mm.

The diffusion-weighted sequence includes a single refocusing pulse with a repetition time (TR) of 6000 ms and an echo time (TE) of 71 ms. Diffusion data is acquired along 90 different directions with distinct b-values: 30 directions with a b-value = 1000 mm/s^2, 60 directions with a b-value = 2600 mm/s^2 and 9 $b = 0$ images randomly dispersed in between the diffusion-weighted images. Just as for the phantoms, the ASSET factor is set to 2 with a multiband factor equal to 2. This allows for a faster volume reconstruction by acquiring more than one slice per excitation. The field of view is chosen to be $240 \times 240\,mm^2$ and a matrix size of 96×96. The slice thickness is set to be 2.5 mm with a total number of slices equal to 66. Also for the brains, spectral fat saturation with non-spectral selective excitation is included in the sequence and the sequence is adapted to output the integrated reverse polarity phase encode acquisition.

Table 3.1: Comparison between the parameters of the sequence acquisition used for the phantoms and for the *in vivo* scans.

	Phantoms	Brain
TR	6000 ms	6000 ms
TE	70.1 ms	71 ms
Diffusion directions	90	90
b-values	1000 mm/s^2	2600 mm/s^2
	1000 mm/s^2	2600 mm/s^2
$b = 0$ images	9	9
Field of view	$240 \times 240\,mm^2$	$240 \times 240\,mm^2$
Matrix size	96×96	96×96
Slice thickness	2.5 mm	2.5 mm
Number of slices	32	66

Chapter 4

Software implementation

This chapter focuses on the practical implementation of the software tools used to analyse diffusion MRI data.

The first part shows how to simply fit the tensor model to the DW-MRI data using the `dtifit` function of the FMRIB Software Library (FSL) [42], a well-used software suite in the neuroimaging community. It also goes into detail about integrating FSL into Python with the `fslpy` library, combining the robust functionalities of FSL with the flexibility and versatility of the Python programming environment.

The second section goes into the Bingham-NODDI model [9] implementation by using the Dmipy library [52], an open-source Python programme built specifically for modelling and analysing diffusion magnetic resonance data by building and constructing multi-compartment modelling methodologies.

The final section delves into the implementation of the AMICO-NODDI model [49] using resources from the AMICO repository on GitHub (`https://github.com/daducci/AMICO`).

4.1 Tensor model

The tensor model was implemented using the FMRIB Software Library (FSL), which is a comprehensive and widely used software package designed for the analysis of functional and structural neuroimaging data, with a major focus on magnetic resonance imaging (MRI) techniques [42, 40, 53]. FSL was developed by the Oxford Centre for Functional MRI of the Brain (FMRIB) at the University of Oxford. Because of its reliability, adaptability, and broad range of capabilities, FSL is widely employed in the neuroscience and medical imaging fields. Although some of its tools include graphical user interfaces (GUIs), it is mostly command-line driven.

FSL provides a variety of tools and utilities for processing and analysing different types of neuroimaging data. Among all the available features, FSL includes tools for processing diffusion-weighted MRI (DW-MRI) data, as well as estimating diffusion tensor metrics by fitting the tensor model to the DW-MRI data. In addition to data analysis capabilities, FSL provides visualisation tools (FSLeyes) for showing and studying neuroimaging data and results.

In FSL, the `dtifit` command is used to fit the diffusion tensor model to diffusion-weighted MRI data. The `dtifit` command's principal function is to estimate the diffusion tensor parameters using DW-MRI data. These parameters include the three eigenvalues of the

tensor λ_1, λ_2 and λ_3, which correspond to the magnitudes of water motion in the tissue microstructure's principal directions. After estimating the three eigenvalues, mean diffusivity and fractional anisotropy can be computed using Equations (2.6) and (2.7), with the ultimate goal of obtaining valuable information about tissue integrity, anisotropy, and other structural properties.

The inputs of the `dtifit` command include a series of diffusion-weighted images acquired with different gradient directions and b-values, as described in Section 2.2 and 3.3. These images capture the diffusion of water molecules in various directions and sensitivities. The input diffusion-weighted images must be in the *.nii* format. In addition, a binary brain mask must be provided as input in the *.nii* format. Moreover, the b-values and gradient directions must be provided in separate *.bval* and *.bvec* files.

The `dtifit` command generates several output files, usually saved in *.nii* format. The MD map, which depicts the average diffusion in each voxel, is the first result delivered. In addition, the FA map, which represents the degree of anisotropy in each voxel, is provided as output.

In this work, FSL was used in Python, thanks to the `fslpy` package. The `fslpy` project is an FSL programming library written in Python. This package contains all the Python functions which can be used to invoke FSL commands. FSL may thus be easily accessed and integrated into the rest of the programming needed to analyse the collected data using Python commands. The `fslpy` complete documentation can be found at `https://open.win.ox.ac.uk/pages/fsl/fslpy/index.html#`.

4.2 The Bingham-NODDI implementation

The first implementation of Neurite Orientation Dispersion and Density Imaging, also known as Watson-NODDI, was accomplished through a package of functions called the 'NODDI toolbox' in MATLAB, created by The Mathworks company in Natick, USA. The toolbox can be accessed at `http://mig.cs.ucl.ac.uk/index.php?n=Download.NODDI`. This toolbox allows users to select from a variety of biophysical models. The input diffusion-weighted images must be in the *.nii* format, and the b-values and gradient directions must be provided in separate *.bval* and *.bvec* files. Additionally, a binary brain mask in *.nii* format is required, and the user must specify the name of the model to be fitted.

The implementation of the Bingham-NODDI model can be facilitated by the use of the Diffusion Microstructure Imaging in Python (Dmipy) package, recently introduced by Fick et al. [52]. Dmipy is an open-source Python package specifically developed for modelling and analysing diffusion magnetic resonance data by designing and developing multi-compartment modelling strategies. It offers a comprehensive set of tools and functions that allows to easily incorporate complex diffusion models, such as the Bingham-NODDI model, into the analysis pipeline. Dmipy is a software that implements biophysical models independently, allowing for multi-compartment modelling that can be customised for the situation at hand. The framework also includes multiple fitting routines that can be selected without hard coding. Figure 4.1 presents the Dmipy workflow, showing how different and distinct models can independently be called at once, building a more complex multicompartment model: different biophysical tissue models are combined in a multi-compartment model and fitted to diffusion data using an

optimisation algorithm. This estimates tissue feature parameters, reconstructs fibre orientation distributions (FODs), and quantifies fitting quality. Dmipy is publicly available (`https://github.com/AthenaEPI/dmipy`) and includes tutorials for fitting multi-compartment models from the literature.

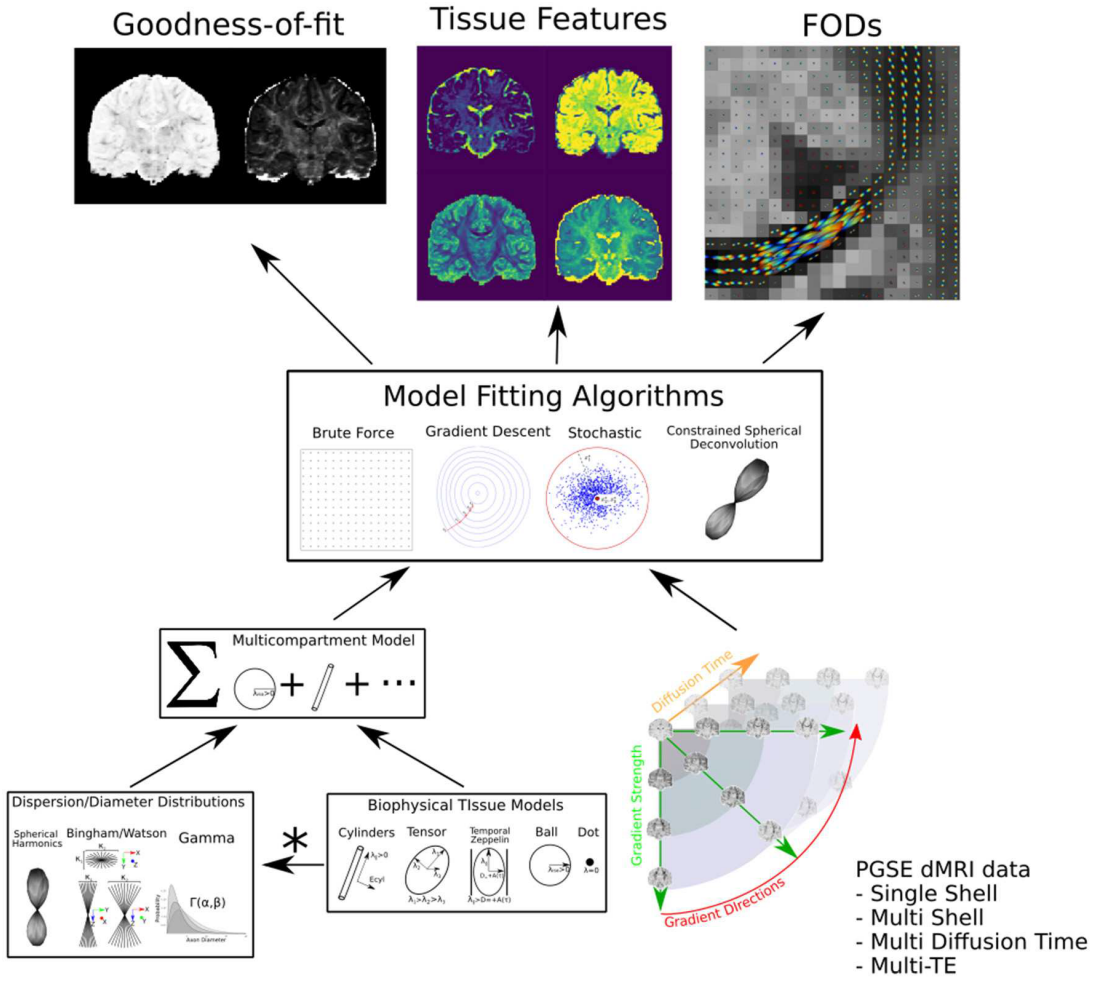

Figure 4.1: Dmipy workflow: Modular microstructure model setup and parameter estimation. Different biophysical tissue models are dispersed and/or distributed and combined together in a multi-compartment model, which is then fit to diffusion data using a chosen optimization algorithm to estimate tissue feature parameters, reconstruct FODs, and quantify the quality of the fitting. Image credit to "*The Dmipy Toolbox: Diffusion MRI Multi-Compartment Modeling and Microstructure Recovery Made Easy*" [52].

Equation (4.1) summarises the implementation of the Bingham-NODDI model, within the Dmipy framework.

$$S = \underbrace{f_{\text{CSF}}\overbrace{S_{\text{iso}}(\cdot|D_{\text{CSF}})}^{\text{Ball}}}_{\text{CSF}} + \overbrace{B(\kappa_1,\kappa_2,\boldsymbol{\mu}_i)}^{\text{Bingham}} *_{\mathbb{S}^2} \left[\underbrace{f_{\text{en}}\overbrace{S_{\text{en}}(\cdot|\lambda_\perp^{\text{tort}},\lambda_\parallel^{\text{tort}})}^{\text{Zeppelin}}}_{\text{Hindered Extra-Axonal}} + \underbrace{f_{\text{in}}\overbrace{S_{\text{in}}(\cdot|\lambda_\parallel)}^{\text{Stick}}}_{\text{Intra-Axonal}}\right] \tag{4.1}$$

The characterisation of the total diffusion signal involves the application of multiple models, each tailored to capture the unique diffusion behaviours observed in different compartments. Specifically, the CSF compartment is represented using the Ball model, an

isotropic Gaussian compartment whose signal attenuation only depends on isotropic diffusivity λ_{iso} [52]. The extra-neurite compartment is described as the Zeppelin component, an axially symmetric Gaussian distribution aligned along orientation $\hat{\mu}$, with parallel and perpendicular diffusivity $\lambda_{\parallel} \geq \lambda_{\perp}$, often used to describe the diffusion signal originating from the oriented, extra-axonal space [52]. Finally, the intra-neurite compartment is modelled as a Stick, a cylinder with a diameter of zero. It has Gaussian diffusivity $\lambda_{\parallel}$ along the cylinder's axis and $\lambda_{\perp} = 0$ perpendicular to the axis [52]. Notably, the orientation distribution function used for the tissue compartment is the Bingham distribution, defined as an anisotropic Gaussian distribution on the sphere with orientation μ and primary and secondary concentration concentrations κ_1 and κ_2. To describe the neurite concentration, the optimisation parameters ODI and β-fraction are used. The ODI is defined in Equation (2.22), while the β-fraction is defined as follows:

$$\kappa_2 = \beta \cdot \kappa_1 \tag{4.2}$$

As described in Equation (4.2), β-fraction is used to characterise the degree of dispersion in the secondary direction within the Bingham distribution.

Figure 4.2 presents a visual depiction of the implementation of the Bingham-NODDI model. Through this combination of different simple models, Dmipy enables a comprehensive analysis of diffusion MRI data, accounting for the distinct diffusion properties exhibited by various compartments.

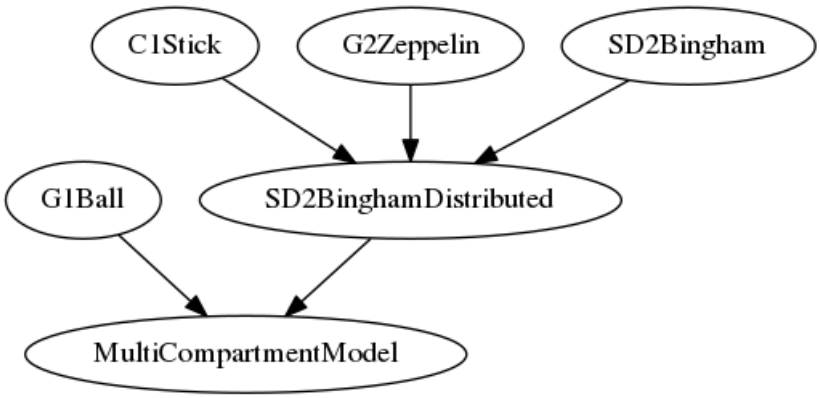

Figure 4.2: Visual representation of the Bingham-NODDI model as the combination of several simpler models.

Fitting Bingham-NODDI requires very similar inputs to the MATLAB toolbox. First of all, the preprocessed diffusion-weighted data in the *.nii* format is required. Then, the diffusion protocol specification in the form of a *.bval* text file for b-values and a *.bvec* text file for gradient directions is required. b-values are usually supplied in s/mm^2, but in this case they have to be converted to s/m^2. Moreover, a binary brain mask needs to be provided in the *.nii* format.

The implementation of the Bingham-NODDI model in Dmipy produces several quantitative maps as output. In particular, the output includes the tissue volume fraction map, indicating the tissue proportion within each voxel. Additionally, the intra-neurite volume fraction map specifies the fraction of the voxel occupied by neurites. Furthermore, Dmipy generates a quantitative map representing the Orientation Dispersion Index (ODI), defined in Equation (2.22). This map quantifies the degree of dispersion or coherence of

neurite orientations within each voxel. Finally, the mean squared error (MSE) and the R^2 maps are provided to assess the goodness of fit.

Fitting Bingham-NODDI is quite time-consuming, with the time required to complete the fitting procedure effectively ranging between 13 and 15 hours for one single acquisition.

4.3 AMICO-NODDI implementation

The AMICO framework includes a linearised version of NODDI in its repository, which is publicly available (`https://github.com/daducci/AMICO`). Although a MATLAB implementation exists (`https://github.com/daducci/AMICO_matlab`), it is outdated and no longer officially supported by the authors. All necessary MATLAB functions have been rewritten in Python.

Before fitting the model, the dataset needs to be organized according to the scheme shown in Figure 4.3. Each subject acquisition needs to be stored in the appropriate subfolder inside the dataset root directory, denoted by a specific diffusion protocol.

```
├─ data
    ├─ Study_01               --> all subjects acquired with protocol "Study_01"
        ├─ Subject_01
        ├─ Subject_02
        ├─ ...
    ├─ Study_02               --> all subjects acquired with protocol "Study_02"
        ├─ Subject_01
        ├─ Subject_02
        ├─ ...
    ├─ ...
```

Figure 4.3: When the fitting procedure begins, AMICO assumes this specific folder layout.

This requirement was made to improve computational efficiency. For a particular b-value, AMICO generates a large number of probable dictionary terms known as 'kernels' with high angular resolution, which are shared among participants scanned with the same b-values, regardless of the number of DW images in the dataset. Once the kernel is produced, the collection of synthetic signals is resampled to match the actual gradient directions and may be used to fit the model in the dictionary. As a result, patients in the same study who were scanned using the same diffusion protocol will have identical pre-computed kernels in memory. This method is particularly useful because kernel computing is one of the most time-consuming processes in the entire procedure.

Fitting AMICO-NODDI requires the following inputs. First of all, the preprocessed diffusion-weighted data in the *.hdr / .img* format is required. Then, the diffusion protocol specification in the form of a *.bval* text file for b-values and a *.bvec* text file for gradient directions is necessary. Finally, a *.hdr / .img* file containing the binary image that describes the brain mask needs to be provided.

Fitting NODDI in the AMICO framework takes approximately 5-10 minutes for each acquisition, which is a dramatically reduced time extent with respect to the original version of the model.

Chapter 5

Data analysis method

This chapter illustrates the data analysis method, starting from the preprocessing of the acquired images to the statistical analysis of the obtained results, given as output from the fit of the models to the preprocessed data. Python scripts were written on purpose to process and analyse the DW-MRI data collected at the Oxford Centre for Clinical Magnetic Resonance Research (OCMR) with the 3 T GE Premier scanner. All the in-house Python scripts used in this work for processing and analysing the acquired data can be found on the GitHub page Oxford Molecular Imaging.

The first part of the chapter focuses on the analysis of the phantom data, illustrating each step of the processing and analysis pipeline. In the second and last part of the chapter, the *in vivo* data analysis is presented and described.

5.1 Phantom data analysis

Two phantoms are used in this work, as described in Section 3.1, to evaluate the stability of the diffusion results across time. These phantoms are scanned four times on different days, over a period of one month. The sequence acquisition is described in Section 3.3. Several preprocessing steps are required before fitting the tensor model and the NODDI model to the collected diffusion MRI data to correct for distortions caused by field inhomogeneities and eddy currents during the acquisition process. Thanks to the use of the `fslpy` library, all of the preprocessing steps are integrated into one Python script that can be employed to analyse phantom data.

The first step in the preprocessing pipeline is the correction of the artefacts caused by the local inhomogeneities of the B_0 field. This can be achieved by using the TOPUP tool [39] of FSL, as explained in Section 2.3. TOPUP is available in the `fslpy` library with the Python command `topup`.

The generation of a binary mask to locate the phantom in the image, particularly the anisotropic diffusion ring, is the second stage in the preprocessing pipeline. The binary mask is designed using a Python function that, given the 3D picture provided by TOPUP as input, iteratively calculates the mean noise value from a subset of the input data, incrementally increasing the kernel size until a valid mean noise value is found. This noise level is used to normalise the original input array, thereby scaling it in relation to noise. The normalised data is then thresholded using the given signal-to-noise ratio (SNR) threshold. Areas in the normalised data below the threshold are assigned to 0 in the mask, indicating areas with a low signal-to-noise ratio, whilst regions above the threshold are put to 1,

indicating areas with sufficient signal intensity compared to noise.

The created binary mask is then used in the third step of the preprocessing pipeline, that is the correction of distortions due to the presence of eddy currents, as introduced in Section 2.3. To do this, the EDDY tool [41] of FSL can be exploited using the `fslpy` Python command `eddy`. EDDY takes up to 4 hours to run and its primary output is the corrected 4D DW-MRI image.

Figure 5.1a depicts the original diffusion-weighted image of the basic phantom, in which the phantom appears to be deformed, particularly along the direction of the phase encoding gradient. In Figure 5.1b, the binary mask created using the SNR threshold is shown. This is necessary to correct the data from eddy currents using EDDY. Finally, Figure 5.1c shows the corrected DW-image, which is now ready to fit the tensor and NODDI models.

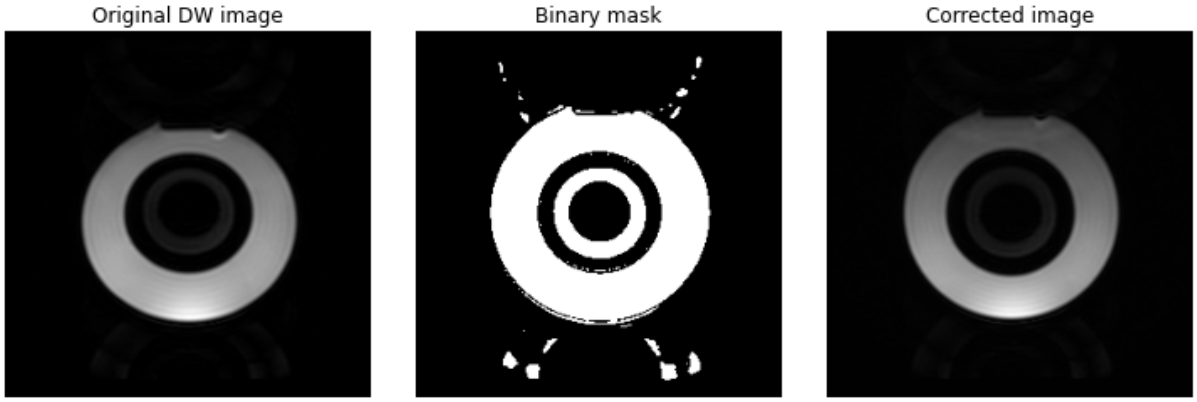

(a) (b) (c)

Figure 5.1: (a) Image of the original diffusion-weighted image of the basic phantom, in which it appears to be warped, notably along the phase encoding gradient direction. (b) The binary mask constructed using the SNR threshold is displayed. (c) The corrected DW-image.

After correcting for distortions in the images, the tensor model may be fitted to the diffusion data to get the final quantitative maps of mean diffusivity (MD) and fractional anisotropy (FA). Because the region of interest in the phantom is the section of the phantom that contains the fibre bundles, another binary mask is created in which only the voxel containing the fibre bundles is set to 1, while the rest are set to zero. Only the region of the fibre bundles is fitted to the models of interest in this way. This step is carried out manually for both the basic and crossing phantoms using the FSLeyes viewer tool. The two masks designed prior to model fitting are depicted in Figure 5.2.
The tensor model can be fitted to the EDDY-corrected data using the `dtifit` function in Python, as well as the binary mask that was just constructed. The fitting process takes about 5 minutes and the desired quantitative maps of MD and FA are finally obtained.

The FSL commands `fslmaths` and `fslstats` are used to extract the mean value of MD and FA from the fibre rings. For the basic phantom, the MD and FA mean values are derived from the entire fibre ring. The mean value and standard deviation for the MD and FA are directly extracted using the `fslstats` command in Python, provided by `fslpy`. Instead, for the crossing phantom, two additional binary masks are constructed to extract the mean value of MD and FA from the phantom's rings region and crossing region independently. These binary masks, shown in Figure 5.3, are designed manually

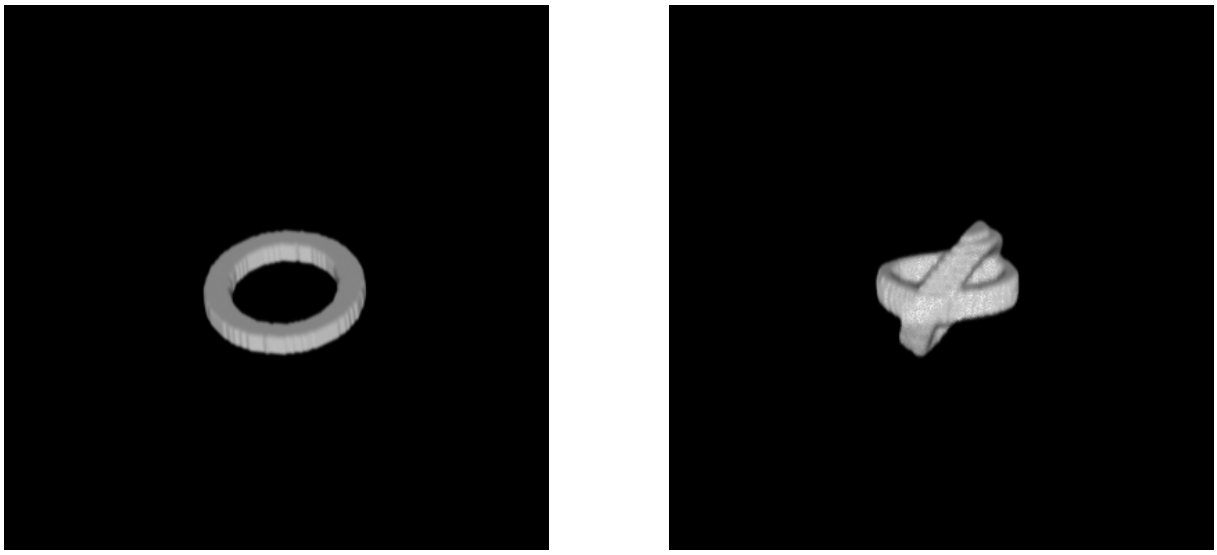

(a) (b)

Figure 5.2: Binary masks have been created for the regions in the phantoms with fibre bundles. This includes (a) a ring mask for the basic phantom and (b) rings mask for the crossing phantom.

using the FSLeyes viewer by FSL.

The quantitative maps are multiplied to the rings binary mask, Figure 5.3a, to extract the tensor model results from the rings region of the crossing phantom using the FSL command `fslmaths` in Python. The mean value and standard deviation of MD and FA are then calculated in Python using the FSL tool `fslstats`. The same approach is used to extract the results from the crossing region of the crossing phantom, with the exception that the quantitative maps are multiplied by the crossing region binary mask, shown in Figure 5.3b.

(a) (b)

Figure 5.3: Two binary masks were designed to extract diffusion results separately from the rings region and the crossing region of the crossing phantom: (a) mask with only the two rings, and (b) mask for the region where the two fibres cross eachother.

In addition to the tensor model, the data is fitted to the Bingham-NODDI and AMICO-NODDI models. The Bingham-NODDI model is implemented using the Dmipy Python module, as stated in Section 4.2, and the fitting method can take up to 15 hours to complete. The AMICO-NODDI is implemented using the publicly accessible GitHub repository, as described in Section 4.3. The quantitative maps of interest for both models are the tissue volume fraction, intra-neurite volume fraction, and ODI defined in Equation (2.22), to characterise neurite dispersion. These results are extracted using the same ROIs and procedure as the MD and FA values.

As previously stated, the two phantoms are scanned four times on separate days using the same scanner and sequence acquisition to examine the repeatability of the DTI fit results over time. The data is analysed using the previously described approach, obtaining multiple values for all the quantities of interest. The coefficient of variation (CV) is calculated to determine whether there is variance in the results over time. It is defined as follows:

$$CV = \frac{\text{Standard deviation}}{\text{Mean}} \cdot 100 \tag{5.1}$$

The coefficient of variation (CV) is a statistical measure that expresses a dataset's relative variability or dispersion in relation to its mean. It is calculated as the ratio of the standard deviation (a measure of dispersion) to the mean and is commonly given as a percentage, as specified in Equation (5.1). A higher CV indicates more relative variability, whereas a lower CV indicates less relative variability. In Equation (5.1), the Mean represents the average metric value from ROIs measured on four different days. Similarly, the Standard deviation is the standard deviation computed considering the results of the measurements performed on four different days.

5.2 Brain data analysis

Four healthy participants are scanned using the identical scanner and acquisition protocol outlined in Section 3.3 to assess the consistency of the diffusion data *in vivo*. Each subject is scanned twice, with a roughly 10-minute gap in between the scans. A structural T1-weighted scan (MP-RAGE) and a diffusion-weighted protocol comprise the data acquisition. The pipeline of processing is fairly similar to that given for the phantoms.

The first step in the processing pipeline is to correct the distortion of diffusion-weighted images using FSL's TOPUP [39] and EDDY [41], implemented in Python with `fslpy`. For the *in vivo* data, a brain mask is required for EDDY to define the brain tissue from non-brain structures such as the skull, scalp, and other tissues. The brain mask is obtained using FSL's BET (Brain Extraction Tool), callable in Python with the `fslpy` command `bet`. After correcting for distortion, the tensor and NODDI models can be fitted to the diffusion data to produce the desired quantitative maps: MD, FA, tissue volume fraction, intra-neurite volume fraction, and ODI.

The acquired quantitative maps must be registered to a standard space, the MNI152, before the results can be extracted. The MNI152 space is a commonly used coordinate system in neuroimaging. It is based on the Montreal Neurological Institute (MNI) reference brain, which is a template brain made up of an average of 152 healthy brains. It serves as a reference space against which individual brain scans can be compared and analysed across participants and studies.

In order to perform the registration of the acquired images to the MNI152, there are a few steps that need to be completed. First of all, the b0 volume, the volume acquired with a b-value = 0, is aligned to the T1-weighted scan. This registration can be done with the tool offered by FSL called FLIRT (FMRIB's Linear Image Registration Tool) [54, 55, 56], which is a fully automated robust and accurate tool for linear intra- and inter-modal brain image registration. Image registration involves aligning two images by applying transformations to one of the images, such as translation, rotation, scaling, and shearing transformations so that it closely matches the other image. FLIRT employs a cost function to assess the similarity of the source and reference images after the transformation. The goal is to identify the transformation parameters that minimise this cost function, suggesting improved image alignment. In this work, the cost function that is employed is the mutual information with 6 degrees of freedom (DOF). This number of degrees of freedom determines that only rigid body transformations are used to register the b0 image to the structural T1.

The T1-weighted image must then be registered to the MNI152 space. To accomplish this, first perform a linear registration of the T1 to the MNI using FLIRT with 12 degrees of freedom. Then, using the linear transformation matrix generated by executing FLIRT, a non-linear registration of the T1 to the MNI space can be performed. This is accomplished through the employment of the FSL's tool FNIRT (FMRIB's Nonlinear Image Registration Tool) [57, 58], a nonlinear image registration tool used when the relationship between two pictures involves complicated deformations that cannot be correctly represented by linear transformations.

Along with the T1-weighted image registered to the MNI space, FNIRT generates a coefficient file containing the nonlinear spatial transformation used in each voxel to align the T1 to the MNI space, with the intensity value in each voxel representing the amount that this voxel has been shifted by the transformation. In addition to the T1, this warp file can be used to register other volumes to the MNI space. By using the FSL's command APPLYWARP, all the quantitative maps of interest can be aligned to the MNI152 space by simply applying the transformations contained in the warp file generated by FNIRT.

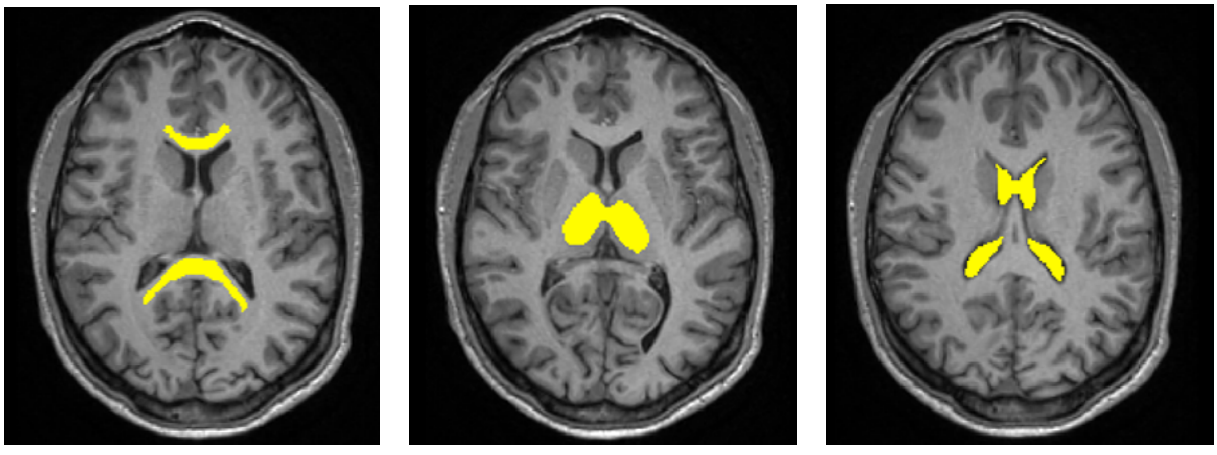

(a) (b) (c)

Figure 5.4: ROIs in the brain used to extract the values of mean diffusivity (MD), fractional anisotropy (FA) and non-tissue volume fraction. One ROI per tissue type has been chosen: (a) Genu and Splenium of Corpus Callosum for white matter, (b) Thalamus for grey matter, (c) Ventricles for CSF.

Several ROIs have been created to extract values from the quantitative maps produced by fitting the tensor and NODDI models to the diffusion data. The binary masks are generated by extracting from the brain atlases available in FSL the regions of interest. Additionally, an erosion is applied to the binary masks in order to avoid possible partial volume effects when extracting the results. The ROIs presented in Figure 5.4 have been created to extract the values of fractional anisotropy (FA) and mean diffusivity (MD). One ROI was chosen for each tissue type: Genu and Splenium of Corpus Callosum for white matter, Thalamus for grey matter, and Ventricles for CSF. These ROIs are designed in the MNI space, and the results are derived from the quantitative maps using FSLMATHS and FSLSTATS.

To obtain more insightful information from the NODDI fit results, particularly the intra-neurite volume fraction and the ODI, because the CFS signal is suppressed in the NODDI model's tissue volume fraction, new ROIs are designed to extract the results from the just mentioned quantitative maps. These ROIs are shown in Figure 5.5 and are the Caudate and Putamen for grey matter, and the anterior and posterior limbs of the Internal Capsule for white matter. Overall, the results of the Bingham component of the NODDI model were extracted from the anterior and posterior limbs of the Internal Capsule and from the Genu and Splenium of the Corpus Callosum for white matter, while for grey matter from the Thalamus, Caudate and Putamen.

Since all ROIs are defined in the MNI space, it is possible to extract results from quantitative maps in the same regions for every acquisition by aligning the maps to MNI152 space. This ensures that ROIs remain consistent between scans and across subjects.

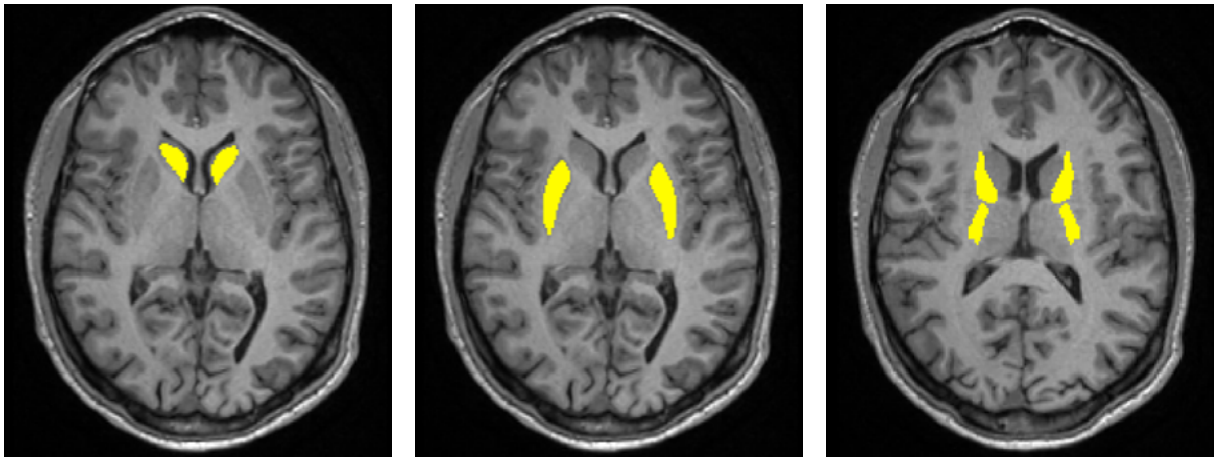

(a) (b) (c)

Figure 5.5: ROIs in the brain used to extract the values of intra-neurite volume fraction and ODI. (a) Caudate for grey matter, (b) Putamen for grey matter, (c) anterior and posterior limbs of the Internal Capsule for white matter.

After the data acquisition and the image processing to obtain all diffusion metrics, a critical step is to conduct a statistical analysis to assess the temporal consistency of the results. A paired t-test is used to determine whether there are statistically significant differences in diffusion parameters between the first and the second scans. This method is ideal for paired data collected from the same participants during different scanning sessions. The paired t-test improves sensitivity to detect important changes in diffusion parameters over time by accounting for inter-subject variability and focusing on within-

subject changes. The null hypothesis in the paired samples t-test is that the average of the differences between the paired observations in the two samples is zero. If the estimated p-value is less than 0.05, the conclusion is that the mean difference between the paired observations is statistically significant different from zero.

Finally, Bland-Altman analysis [59] is performed to assess the consistency and reproducibility of the obtained diffusion metric measurements, derived from both the tensor model and the NODDI model. With the Bland and Altman analysis, it is possible to obtain the Bland-Altman Bias, which represents the median of the differences between the measurements from the two scans and indicates the presence or absence of a consistent offset or bias. A Bland-Altman Bias close to zero suggests that, on average, there is little to no systematic difference between the measurements obtained from the two scans. In addition to the Bland-Altman Bias, the repeatability coefficient (RC) at a 95% confidence interval is obtained. The RC is an estimate of the maximum difference that one would expect to observe between two measurements taken on the same subject under the same conditions. A smaller RC value signifies lower measurement variability and, consequently, higher consistency between the two measurement techniques. The 95% Confidence Interval for the RC provides a range within which the true RC value is likely to fall with a certain level of confidence. If this interval includes zero, it implies that the observed differences between measurements are not statistically significant, reinforcing the notion of agreement between the two models.

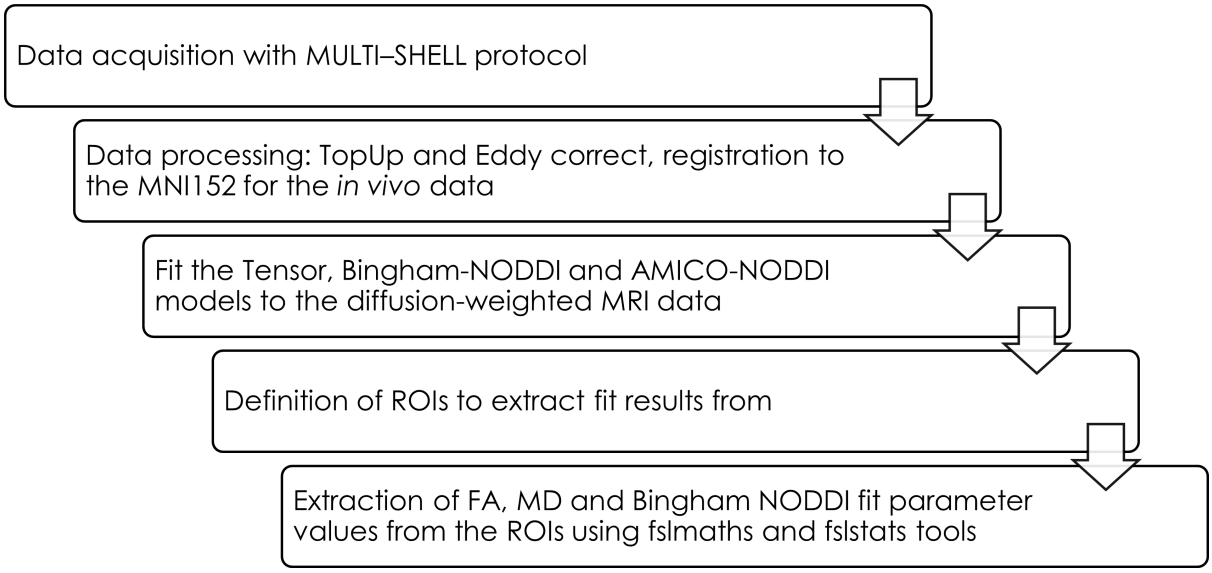

Figure 5.6: Flowchart of the processing pipeline of the diffusion data for the phantoms and the brains.

Results and Discussion

Chapter 6

Phantom results

This chapter presents the results of the analysis performed on the two phantoms. Fitting methods were performed on the collected diffusion-weighted data using either the Tensor and NODDI models, which included both the Bingham and AMICO formulations. The obtained results were determined from the obtained quantitative maps using the binary masks defined in Chapter 5.

The chapter is divided into two sections: the first delves into the results collected from the basic phantom, while the second part focuses on the crossing phantom. In all portions, a detailed explanation of the achieved results is thoughtfully presented.

6.1 Basic phantom repeatability over time

In order to assess the consistency of the diffusion metrics over time, four scans of the basic phantom were acquired. The basic phantom is described in Section 3.1 and illustrated in Figure 3.2. The scans were spread out over a time period of one month and performed at the Oxford Centre for Clinical Magnetic Resonance Research (OCMR) - University of Oxford, using the GE Premier 3 T scanner and a 21 channel head coil, as discussed in Chapter 3.

The acquired data was then fitted with the Tensor and NODDI models, both in the Bingham and AMICO formulations. In the case of the basic phantom, the mean and the standard deviation of the diffusion metrics were extracted from the whole fibre ring using the binary mask shown in Figure 5.2a. Finally, the coefficient of variation (CV) was computed to assess the consistency of the obtained results over time.

Table 6.1: FA and MD results for the basic phantom to look for the consistency of the results over time.

Tensor model		
	FA	MD ($\cdot 10^{-3}\,\mathrm{mm}^2/\mathrm{s}$)
Scan 1	0.79 ± 0.05	0.85 ± 0.08
Scan 2	0.78 ± 0.10	0.80 ± 0.11
Scan 3	0.81 ± 0.04	0.81 ± 0.08
Scan 4	0.81 ± 0.05	0.82 ± 0.08
CV	1.63 %	2.28 %

The tensor model's outcomes from four separate acquisitions on distinct days are pre-

sented in Table 6.1. The key metrics of interest include fractional anisotropy (FA) and mean diffusivity (MD), as well as the coefficient of variation (CV). Table 6.1 demonstrates that both FA and MD exhibit CVs well below 5 %. This indicates that there is minimal variation in diffusion tensor metrics over time, ensuring their reliability and consistency.

The basic phantom's MD and FA maps are displayed in Figure 6.1. From the images, it is clear that the MD and FA values remain constant throughout the entire fibre ring, indicating a uniform distribution of the diffusion properties.

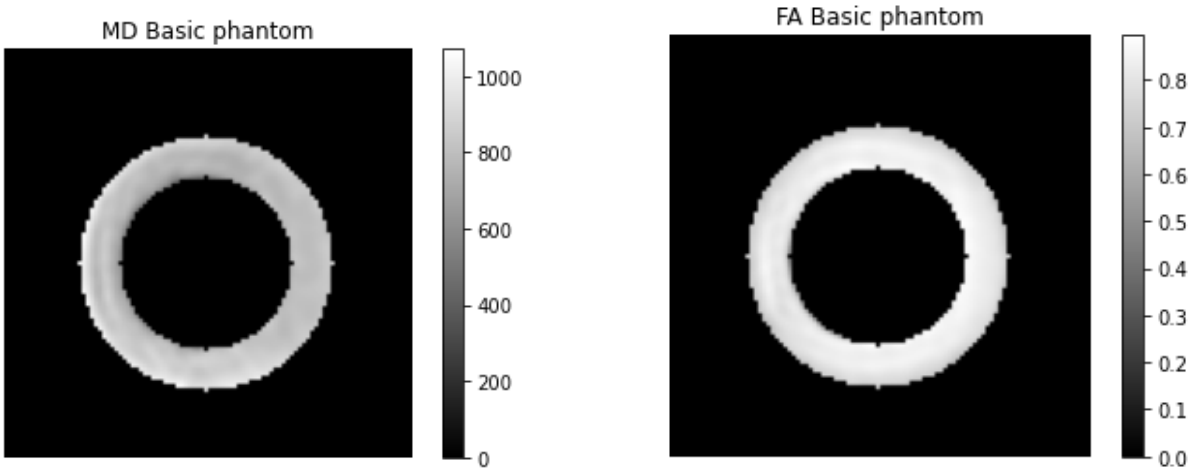

(a) (b)

Figure 6.1: (a) MD expressed in $10^{-6}\,\mathrm{mm}^2/\mathrm{s}$ and (b) FA quantitative maps for the basic phantom. The images show a uniform distribution of the tensor model parameters along the whole fibre ring.

In Table 6.2 the results of the Bingham-NODDI fit parameters for the four acquisitions are presented along with the CV associated to each metric. In Figure 6.2, all the quantitative maps given as output from the Bingham-NODDI fit are shown. These images show a fairly uniform distribution of the parameter of interest within the fibre ring, except for the β-fraction.

To assess the level of dispersion or spread of neurite orientation within a specific brain tissue volume, the orientation dispersion index (ODI) can be analysed. Low ODI values suggest a well-organized structure of neural fibres within the voxel, indicating a relatively uniform alignment of neurites - consistent with the phantom's manufacturing. The obtained results, illustrated in Figure 6.2a, show a strong reproducibility of the ODI value over time, with a CV of 1.36 %.

To better understand the concentration of neurites within a voxel, it is important to consider the β-fraction. This parameter measures the proportion of a voxel's volume that is occupied by neurites, specifically axons and dendrites, in relation to the total volume of the voxel. A higher β-fraction indicates a greater concentration of neurites within the voxel. When the β-fraction is close to 1, it indicates a significant presence of neurites within the voxel and a more anisotropic distribution of neurite orientations. Table 6.2 displays the β-fraction values, which indicate a greater concentration of fibres in the ring compared to other components and the quantitative map is shown in Figure 6.2b. The CV of 6.5 % is slightly above the desired threshold of 5 %. This could be due to the

non-uniform distribution of the β-fraction values in the fibre ring, resulting in a higher standard deviation of the measurements.

Another important NODDI parameter is the tissue volume fraction. This measures the amount of brain tissue, including neurites and other cellular structures, occupying a voxel's volume. It is complementary to the non-tissue volume fraction, which measures the portion of the voxel filled by CSF or other non-tissue components. The values obtained for the basic phantom are very close to 1 as shown by the quantitative map in Figure 6.2c, indicating that the fibre ring is able to mimic the brain tissue, excluding the CSF. Moreover, the results obtained are consistent over time with a CV equal to 1.47 %.

Table 6.2: Bingham-NODDI metrics extracted from the fibre ring of the basic phantom. The metrics of interest are the orientation dispersion index (ODI), the β-fraction, the tissue volume fraction, the intra-neurite volume fraction and the parameters to assess the goodness of fit. The CV is computed to assess the reproducibility of the results over time.

Bingham-NODDI model						
	ODI	β-fraction	Tissue v.f.	Intra-neurite v.f.	R^2	MSE
Scan 1	0.021 ± 0.002	0.36 ± 0.22	0.98 ± 0.04	0.45 ± 0.08	0.985 ± 0.007	0.0011 ± 0.0005
Scan 2	0.0202 ± 0.0015	0.41 ± 0.25	0.96 ± 0.05	0.46 ± 0.08	0.980 ± 0.018	0.0016 ± 0.0016
Scan 3	0.0202 ± 0.0009	0.37 ± 0.25	0.94 ± 0.09	0.44 ± 0.08	0.982 ± 0.007	0.0014 ± 0.0006
Scan 4	0.0201 ± 0.0007	0.42 ± 0.21	0.96 ± 0.04	0.45 ± 0.07	0.985 ± 0.004	0.0012 ± 0.0004
CV	1.36 %	6.5 %	1.47 %	1.57 %	0.22 %	14.5 %

In addition to the tissue volume fraction, the intra-neurite volume fraction refers to the proportion of the voxel's volume that is occupied by the fibres of the phantom, without considering other tissue components. Also in the case of the intra-neurite volume fraction, the results in Figure 6.2d are repeatable over time with a coefficient of variation of 1.57 %.

Finally, to evaluate the goodness of fit, two measures are available - the mean squared error (MSE) and the R^2. The obtained values for the two indices indicate that the model fits well the data, with a very low MSE, in Figure 6.2f, and an R^2 coefficient very close to 1, as shown in Figure 6.2e. Additionally, the CV for the R^2 is extremely low, equal to 0.22 %, while for the MSE is 14.5 %. The quite high CV for the MSE can be due to the very low values of the MSE itself, in some cases also equal to its standard deviation.

Table 6.3: The table shows the mean and standard deviation of metrics extracted from the basic phantom's fibre ring. These include the orientation dispersion (OD) index, isotropic volume fraction (ISOVF), and intra-cellular volume fraction (ICVF). CV indicates result reproducibility over time.

AMICO-NODDI model			
	OD	ISOVF	ICVF
Scan 1	0.0300 ± 0.0005	0.05 ± 0.04	0.45 ± 0.07
Scan 2	0.0300 ± 0.0007	0.06 ± 0.05	0.47 ± 0.09
Scan 3	0.0300 ± 0.0002	0.06 ± 0.04	0.44 ± 0.08
Scan 4	0.0300 ± 0.0003	0.08 ± 0.06	0.44 ± 0.10
CV	0 %	17.4 %	2.72 %

The acquired diffusion data was also fitted to the linear formulation of the Watson-NODDI model, referred to as the AMICO-NODDI model, illustrated in Section 2.5. The implementation of the AMICO-NODDI model is explained in Section 4.3. The parameters of

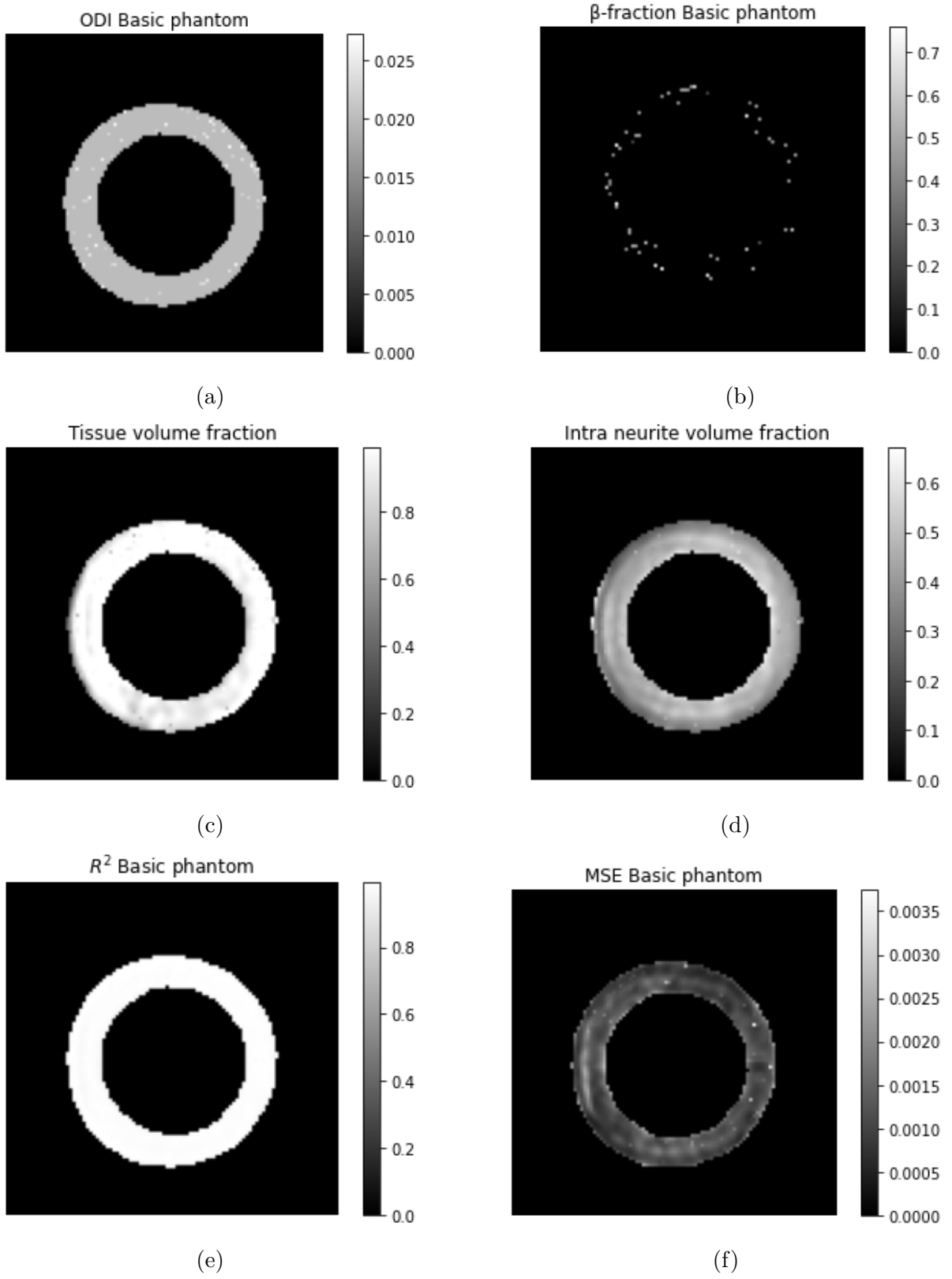

Figure 6.2: Quantitative maps of the parameters given as output by the Bingham-NODDI model. The images represent (a) the ODI, (b) the β-fraction, (c) the tissue volume fraction, (d) the intra-neurite volume fraction, (e) R^2 coefficient and (f) the mean squared error.

interest in the case of the AMICO-NODDI model are the orientation dispersion (OD) index, the isotropic volume fraction (ISOVF) and the intra-cellular volume fraction (ICVF), which corresponds to the intra-neurite volume fraction in the Bingham formulation of the NODDI model. Table 6.3 presents the results for the AMICO-NODDI model in the case of the repeated measurements over time of the basic phantom, while the quantitative maps are shown in Figure 6.3.

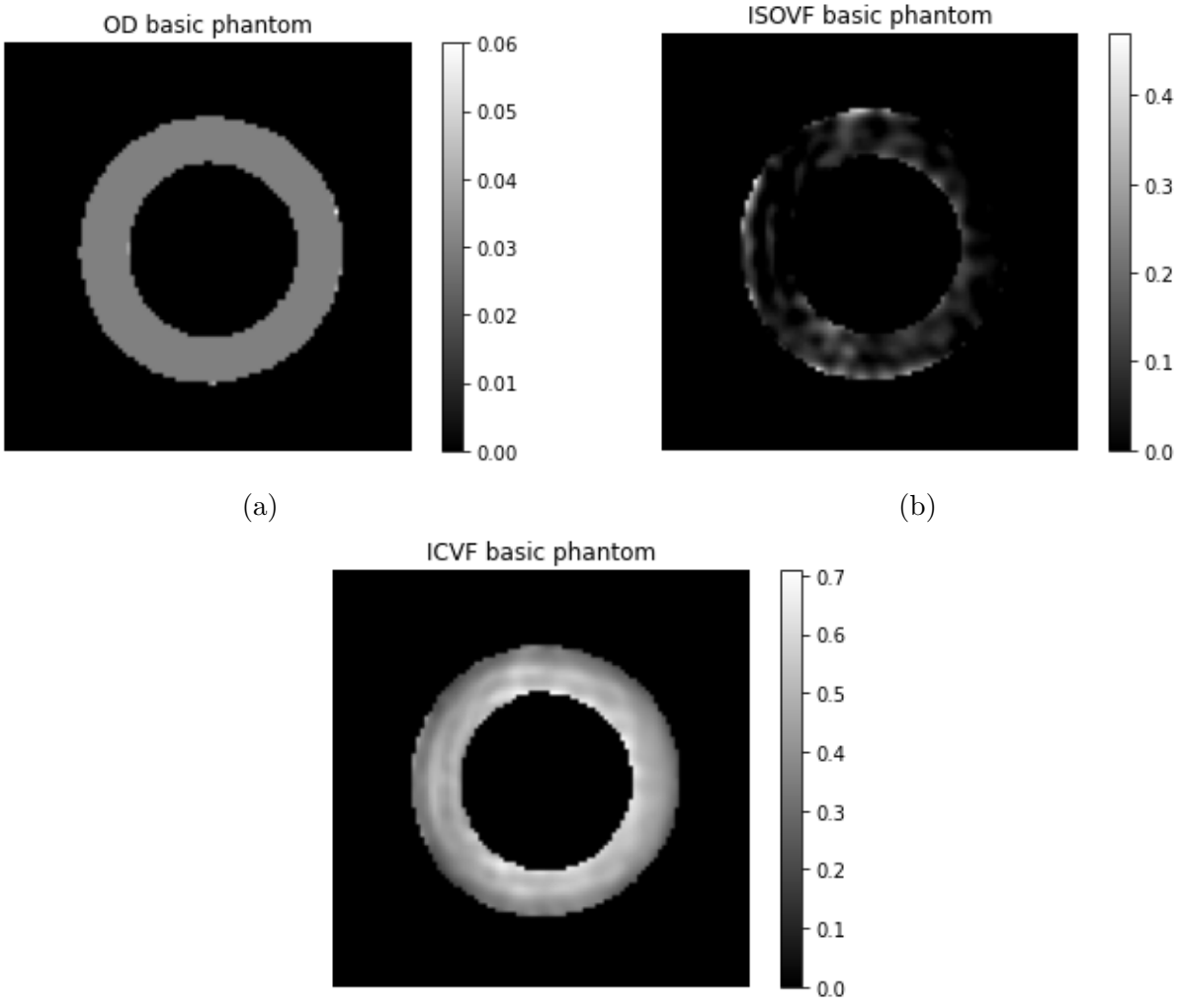

Figure 6.3: (a) orientation dispersion (OD) index, (b) isotropic volume fraction (ISOVF) and (c) intra-cellular volume fraction (ICVF) quantitative maps for the basic phantom given by the AMICO-NODDI model. The images show how the parameters are distributed over the fibre ring.

The OD index, which indicates the level of neurite orientation dispersion, has a perfectly constant value across time, with a CV of 0 %. The OD index is similarly nearly perfectly constant across the whole fibre ring, as shown in Figure 6.3a. Furthermore, the OD index of the AMICO model is slightly higher than the ODI of the Bingham-NODDI model. This might be due to the fact that the AMICO formulation adopts the Watson distribution rather than the Bingham distribution to model neurite orientation dispersion.

The ISOVF, shown in Figure 6.3b, as expected, has a very low value, emphasising how the phantom was created with the goal of mimicking neurite fibres in the human brain.

On the other hand, the standard deviation associated with the values of this parameter is almost as high as the value itself, bringing to a CV equal to 17.4 %. Finally, the ICVF, shown in Figure 6.3c, presents a low coefficient of variation of 2.72 %, indicating the strong consistency and reliability of this parameter over time. Moreover, the values obtained in the AMICO formulation are consistent with the values obtained for the intra-neurite volume fraction in the Bingham-NODDI model, reported in Table 6.2.

Overall, the results obtained for the basic phantom, in all three cases of the tensor model, the Bingham-NODDI model and the AMICO-NODDI model, are consistent and repeatable in time, assessing in this way the stability and reliability of the NODDI model in both formulations.

To investigate whether the repeated acquisition of data could impact the accuracy of measurements, an analysis was conducted using the basic phantom. Specifically, the study aimed to assess whether the heating of the magnetic field gradient coil and variations in the main magnetic field due to heating after multiple acquisitions had any effect on the results. To do this, the phantom was scanned eight times, with one acquisition right after the other and the acquired data was fitted with both the Bingham and AMICO formulations of the NODDI model.

Table 6.4: Bingham-NODDI metrics of the basic phantom from eight scans in a row. The metrics of interest are the orientation dispersion index (ODI), the β-fraction, the tissue volume fraction, the intra-neurite volume fraction and the parameters to assess the goodness of fit. The CV is computed to assess whether the magnetic field gradient coils heating could affect in any way the measurements.

Bingham-NODDI model						
	ODI	β-fraction	Tissue v.f.	Intra-neurite v.f.	R^2	MSE
Scan 1	0.0202 ± 0.0009	0.37 ± 0.25	0.94 ± 0.09	0.44 ± 0.08	0.982 ± 0.007	0.0014 ± 0.0006
Scan 2	0.0202 ± 0.0009	0.37 ± 0.24	0.97 ± 0.05	0.43 ± 0.07	0.983 ± 0.006	0.0014 ± 0.0005
Scan 3	0.0202 ± 0.0009	0.37 ± 0.24	0.97 ± 0.05	0.43 ± 0.07	0.983 ± 0.006	0.0013 ± 0.0005
Scan 4	0.0202 ± 0.0009	0.36 ± 0.25	0.97 ± 0.05	0.42 ± 0.07	0.983 ± 0.006	0.0013 ± 0.0005
Scan 5	0.0202 ± 0.0009	0.35 ± 0.24	0.97 ± 0.04	0.42 ± 0.07	0.983 ± 0.006	0.0013 ± 0.0005
Scan 6	0.0202 ± 0.0009	0.38 ± 0.24	0.96 ± 0.05	0.42 ± 0.07	0.982 ± 0.006	0.0014 ± 0.0005
Scan 7	0.0202 ± 0.0009	0.36 ± 0.24	0.97 ± 0.05	0.42 ± 0.07	0.983 ± 0.006	0.0014 ± 0.0005
Scan 8	0.0201 ± 0.0008	0.37 ± 0.23	0.96 ± 0.05	0.43 ± 0.07	0.983 ± 0.006	0.0014 ± 0.0005
CV	0.16 %	2.34 %	1.03 %	1.63 %	0.044 %	3.55 %

Table 6.4 presents the analysis results, demonstrating a remarkable level of stability exhibited by the Bingham-NODDI metrics across all eight successive acquisitions. This is evidenced by the conspicuously low coefficients of variation associated with each parameter. This observation conclusively verifies the Bingham-NODDI analytical method's consistency, showcasing its robustness against potential distortion caused by magnetic field gradient coil heating. As a result, this not only confirms the method's reliability but also offers the opportunity to conduct multiple consecutive scans without compromising metric accuracy.

Similarly, Table 6.5 illustrates the AMICO-NODDI model analysis results, indicating a notable degree of consistency across all eight subsequent acquisitions. The AMICO-NODDI analytical approach's robustness is highlighted by the significantly low CV for each parameter, even in the presence of possible magnetic field gradient coil heating-induced distortions. This result demonstrates the scanner's stability and the method's reliability,

providing an opportunity to do several successive scans without impacting the validity of the produced metrics.

Table 6.5: AMICO-NODDI results for the basic phantom in the case of eight consecutive measurements. The table reports the mean and standard deviation for each metric extracted from the fibre ring of the basic phantom. The metrics of interest are the orientation dispersion (OD) index, the isotropic volume fraction (ISOVF) and the intra-cellular volume fraction (ICVF). The CV is calculated to determine whether the magnetic field gradient coil heating has any effect on the measurements.

AMICO-NODDI model			
	OD	ISOVF	ICVF
Scan 1	0.0300 ± 0.0002	0.06 ± 0.04	0.44 ± 0.08
Scan 2	0.0300 ± 0.0007	0.06 ± 0.05	0.43 ± 0.08
Scan 3	0.0300 ± 0.0001	0.05 ± 0.05	0.43 ± 0.07
Scan 4	0.0300 ± 0.0006	0.06 ± 0.05	0.43 ± 0.07
Scan 5	0.0300 ± 0.0001	0.05 ± 0.04	0.43 ± 0.07
Scan 6	0.0300 ± 0.0003	0.06 ± 0.05	0.43 ± 0.07
Scan 7	0.0300 ± 0.0001	0.06 ± 0.05	0.43 ± 0.07
Scan 8	0.0300 ± 0.0001	0.06 ± 0.05	0.43 ± 0.07
CV	0 %	7.53 %	0.77 %

6.2 Crossing phantom repeatability over time

The second phantom employed in the study is the crossing phantom, described in Section 3.1 and shown in Figure 3.3. The phantom is used to mimic restricted diffusion in the brain in areas in which crossing fibres are present, as it comprises two fibre rings that cross each other at 60°. The analysis pipeline is analogous to the one used for the basic phantom with the only difference being that the results are extracted from two distinct ROIs, shown in Figure 5.3. These two masks are used to extract the results from the rings and crossing region separately.

Table 6.6: FA and MD results for the crossing phantom both in the region of the rings (Table a) and in the crossing region (Table b). Together with the FA and MD metrics, the CV is shown to assess the consistency of the results over time.

Rings region		
	FA	MD ($\cdot 10^{-3}$ mm^2/s)
Scan 1	0.71 ± 0.06	0.86 ± 0.07
Scan 2	0.71 ± 0.07	0.93 ± 0.09
Scan 3	0.71 ± 0.07	0.93 ± 0.09
Scan 4	0.71 ± 0.08	0.93 ± 0.10
CV	0 %	3.32 %

(a)

Crossing region		
	FA	MD ($\cdot 10^{-3}$ mm^2/s)
Scan 1	0.52 ± 0.05	0.65 ± 0.06
Scan 2	0.51 ± 0.06	0.70 ± 0.08
Scan 3	0.50 ± 0.06	0.70 ± 0.09
Scan 4	0.51 ± 0.06	0.75 ± 0.11
CV	1.39 %	5.05 %

(b)

Table 6.6 presents the results for the tensor model metrics, FA and MD together with the CV to assess the consistency over time. The results show great repeatability, especially

for the fractional anisotropy with a CV equal to 0 % in the rings and 1.39 % in the crossing region, demonstrating the great stability of the tensor model. It is interesting to highlight the fact that the fractional anisotropy is sensibly low in the region in which the two fibre rings cross each other. Also, the mean diffusivity results are repeatable in time with a CV of 3.32 % in the rings region and 5.05 % in the crossing region.

Figure 6.4 shows the quantitative maps for MD and FA in the case of the crossing phantom. It is particularly interesting to notice how the FA and MD values are fairly constant over the fibre ring but drastically change in the region in which the two fibres cross each other, decreasing FA and MD values. This great difference is the main reason why the results were extracted separately from the two regions.

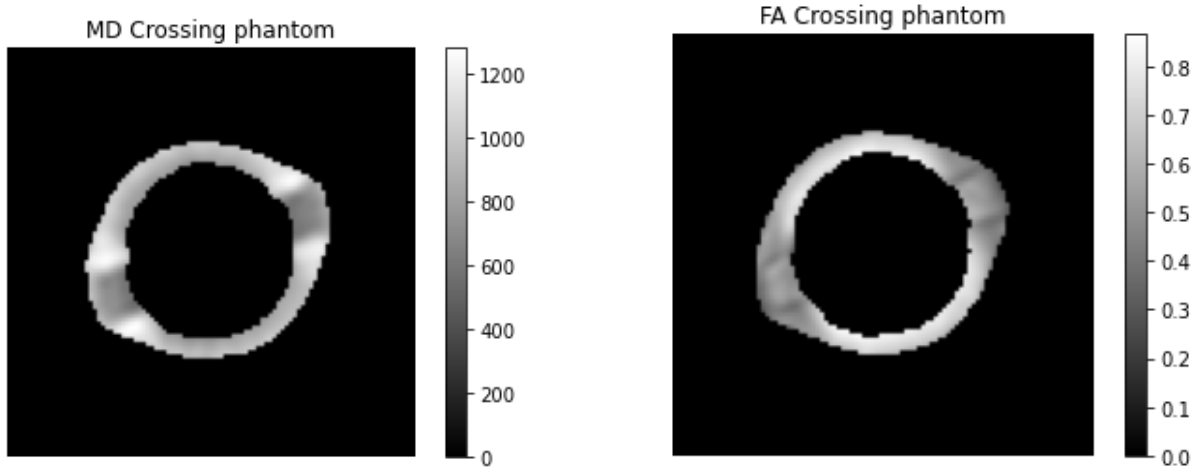

(a) (b)

Figure 6.4: (a) MD expressed in $10^{-6}\,\mathrm{mm}^2/\mathrm{s}$ and (b) FA quantitative maps for the crossing phantom. The images show a uniform distribution of the tensor model parameters along the fibre rings but different values in the crossing region, especially in the case of FA.

The Bingham-NODDI fit results for the crossing phantom are presented in Table 6.7 for the ring region, excluding the fibre crossing area. The ODI value is close to zero, indicating minimal neurite dispersion, while the β-fraction highlights a significant presence of neurites within the rings. The ODI consistency is confirmed with a coefficient of variation of 5.43 %, while the β-fraction presents a higher CV of 16.5 %, suggesting possible variation over time due to its high standard deviation compared to the mean value. This non-uniform distribution of β-fraction can be observed in Figure 6.5b, which displays the quantitative map.

In Table 6.7, the tissue volume fraction is shown to be almost equal to 1, indicating the absence of any water component in the fibre rings. This parameter is highly stable and consistent, evidenced by the CV of only 0.86 %. Furthermore, the study reveals a slightly lower intra-neurite volume fraction when compared to the basic phantom, a result that could be due to how the phantom was manufactured. However, the analysis shows that the intra-neurite volume fraction remains consistent over time with a coefficient of variation of only 3.60 %. The quantitative maps of these two parameters are shown in Figure 6.5c and 6.5d. Finally, the two indices to evaluate the goodness of fit are reported in Table 6.7. The R^2 and MSE show that the Bingham-NODDI model fits well the acquired data with an R^2 coefficient very close to 1 and a mean squared error close to 0.

Table 6.7: Bingham-NODDI metrics extracted from the fibre rings of the crossing phantom. The metrics of interest are the orientation dispersion index (ODI), the β-fraction, the tissue volume fraction, the intra-neurite volume fraction and the parameters to assess the goodness of fit. The CV is computed to assess the reproducibility of the results over time.

Bingham-NODDI – Rings region						
	ODI	β-fraction	Tissue v.f.	Intra-neurite v.f.	R^2	MSE
Scan 1	0.023 ± 0.015	0.49 ± 0.22	0.98 ± 0.05	0.36 ± 0.07	0.987 ± 0.015	0.001 ± 0.001
Scan 2	0.0204 ± 0.0015	0.33 ± 0.25	0.96 ± 0.06	0.33 ± 0.08	0.988 ± 0.004	0.0008 ± 0.0003
Scan 3	0.0203 ± 0.0035	0.34 ± 0.25	0.96 ± 0.05	0.34 ± 0.09	0.986 ± 0.012	0.0010 ± 0.0009
Scan 4	0.0204 ± 0.0013	0.38 ± 0.27	0.97 ± 0.05	0.33 ± 0.08	0.985 ± 0.009	0.0011 ± 0.0007
CV	5.43 %	16.5 %	0.86 %	3.60 %	0.11 %	11.2 %

The same analysis was performed also for the region of the crossing phantom in which the two fibre rings cross each other. In this case, the mean and standard deviation for the parameter of interest were extracted from the ROI defined by the binary mask in Figure 5.3b. The results are reported in Table 6.8

Table 6.8: Bingham-NODDI metrics extracted from the region in which the two fibre rings of the crossing phantom cross each other. The metrics of interest are the orientation dispersion index (ODI), the β-fraction, the tissue volume fraction, the intra-neurite volume fraction and the parameters to assess the goodness of fit. The CV is shown as a metric to assess the reproducibility of the results over time.

Bingham-NODDI – Crossing region						
	ODI	β-fraction	Tissue v.f.	Intra-neurite v.f.	R^2	MSE
Scan 1	0.10 ± 0.05	0.79 ± 0.13	0.990 ± 0.003	0.44 ± 0.07	0.97 ± 0.03	0.002 ± 0.003
Scan 2	0.09 ± 0.05	0.81 ± 0.18	0.986 ± 0.017	0.40 ± 0.07	0.972 ± 0.012	0.0018 ± 0.0008
Scan 3	0.08 ± 0.06	0.83 ± 0.20	0.988 ± 0.008	0.40 ± 0.07	0.972 ± 0.011	0.0019 ± 0.0007
Scan 4	0.06 ± 0.05	0.80 ± 0.17	0.985 ± 0.018	0.38 ± 0.08	0.979 ± 0.009	0.0014 ± 0.0006
CV	17.9 %	1.83 %	0.19 %	5.38 %	0.35 %	12.8 %

The crossing region of the phantom showed a slight increase in ODI compared to the rings region. As it can be seen from the quantitative map in Figure 6.5a, the ODI presents with an uneven distribution in the crossing region, resulting in a CV of 17.9 % as reported in Table 6.8. This high CV is also related to the fact that the Bingham-NODDI model is not able to fully resolve crossing fibres, as shown in the literature. In contrast, the density of fibres in the crossing region of the phantom is greater than in the rings. This is evidenced by the higher β-fraction values, compared to the rings region, which reaches up to 0.83 ± 0.20 with a CV of 1.83 %.

The study revealed that the tissue volume fraction remained consistent over time, with a high level of uniformity even in regions where fibres intersect. The coefficient of variation is 0.19 %, indicating remarkable consistency. The intra-neurite volume fraction is slightly higher in the areas where the fibres cross each other, thus with a higher concentration of fibres, resulting in a coefficient of variation of 5.38 %. The model's fit to the data can be evaluated through the R^2 coefficient and the mean squared error. These parameters show that the Bingham-NODDI model fitted well to the diffusion data, also in the case of the crossing fibres. However, in Figure 6.5f it can be clearly seen how the MSE is higher in the crossing region with respect to its value along the fibre rings.

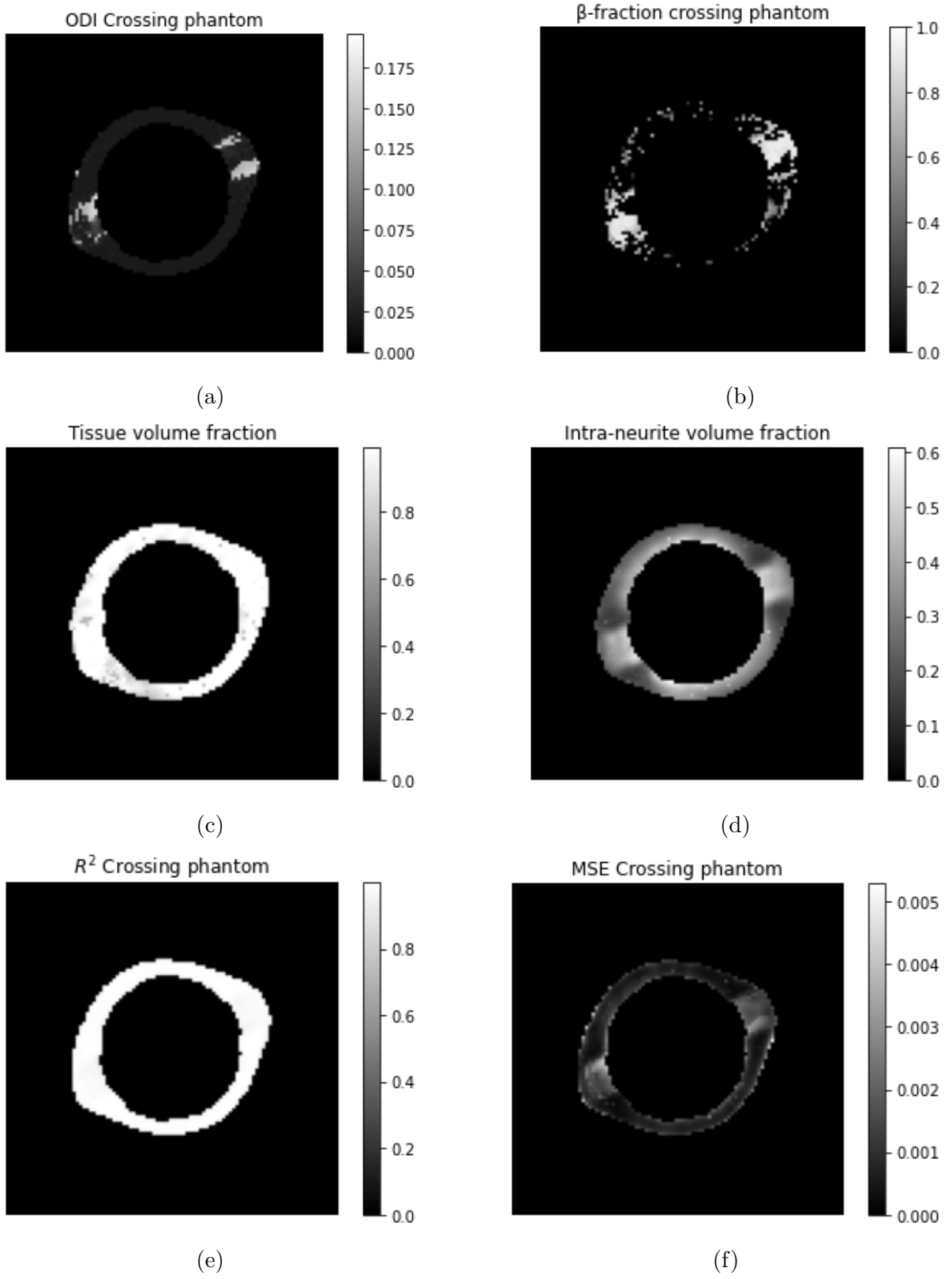

Figure 6.5: Quantitative maps of the parameters given as output by the Bingham-NODDI model. The images represent (a) the ODI, (b) the β-fraction, (c) the tissue volume fraction, (d) the intra-neurite volume fraction, (e) R^2 coefficient and (f) the MSE.

In addition to the Bingham-NODDI mode, the acquired diffusion data of the crossing phantom was also fitted to the AMICO-NODDI model. Table 6.9 presents the results extracted from the two rings of the crossing phantom, while the quantitative maps are shown in Figure 6.6. It can be clearly seen that the OD and the ICVF presents with a strong consistency over time, with CV respectively of 0 % and 2.08 %. As in the case of the basic phantom, the obtained OD values are slighlty lower that the ODI values obtained with the Bingham-NODDI model. This could be due to the fact that the AMICO-NODDI model employes the Watson distribution instead of the Bingham distribution to model neurite orientation dispersion. Moreover, the OD values in the rings of the crossing phantom are consistent with the values obtained in the fibre ring of the basic phantom, showed in Table 6.3. In Figure 6.6c it can be noticed how the ICVF is high and constant along the fibre rings but it substantially decreases when approaching the crossing region, probably due to a fanning of the fibres, leading to a lower neurite density within the single voxel.

Table 6.9: AMICO-NODDI results for the region of the rings of the crossing phantom. The table reports the mean and standard deviation for each metric extracted from the fibre ring of the basic phantom. The metrics of interest are the orientation dispersion (OD) index, the isotropic volume fraction (ISOVF) and the intra-cellular volume fraction. The CV is computed to assess the reproducibility of the results over time.

AMICO-NODDI – Rings region			
	OD	ISOVF	ICVF
Scan 1	0.030 ± 0.002	0.03 ± 0.02	0.35 ± 0.06
Scan 2	0.0300 ± 0.0002	0.06 ± 0.06	0.33 ± 0.08
Scan 3	0.0300 ± 0.0001	0.06 ± 0.04	0.34 ± 0.08
Scan 4	0.0300 ± 0.0006	0.05 ± 0.04	0.34 ± 0.08
CV	0 %	24.5 %	2.08 %

Table 6.10: AMICO-NODDI results for the crossing region of the crossing phantom. The table reports the mean and standard deviation for each metric extracted from the region of the crossing phantom in which the two fibre rings cross each other. The metrics of interest are the orientation dispersion (OD) index, the isotropic volume fraction (ISOVF) and the intra-cellular volume fraction. The CV is computed to assess the reproducibility of the results over time.

AMICO-NODDI – Crossing region			
	OD	ISOVF	ICVF
Scan 1	0.14 ± 0.02	0.0 ± 0.0	0.44 ± 0.06
Scan 2	0.13 ± 0.02	0.04 ± 0.04	0.39 ± 0.07
Scan 3	0.13 ± 0.02	0.04 ± 0.02	0.39 ± 0.07
Scan 4	0.11 ± 0.03	0.04 ± 0.03	0.36 ± 0.08
CV	8.55 %	57.7 %	7.27 %

The results of the AMICO metrics in the region of the crossing phantom in which the two fibre rings cross each other are reported in Table 6.10. In this case, it can be clearly seen that all the metrics present higher CVs, highlighting the fact that the NODDI model cannot correctly resolve crossing fibres. Specifically, the OD has a CV of 8.55 % with a mean

value of 0.13 ± 0.01, higher with respect to the rings region indicating lower compactness of fibres and a higher orientation dispersion. The higher OD value in the crossing region with respect to the rings region can be clearly seen in the quantitative map in Figure 6.6a. The ISOVF results with a high CV, equal to 57.7 %. This could be because the values are comparable to zero due to how the phantom was built. Additionally, in Figure 6.6b it can be noted how the ISOVF is not constant over the fibre rings, contributing to an increase in the CV.

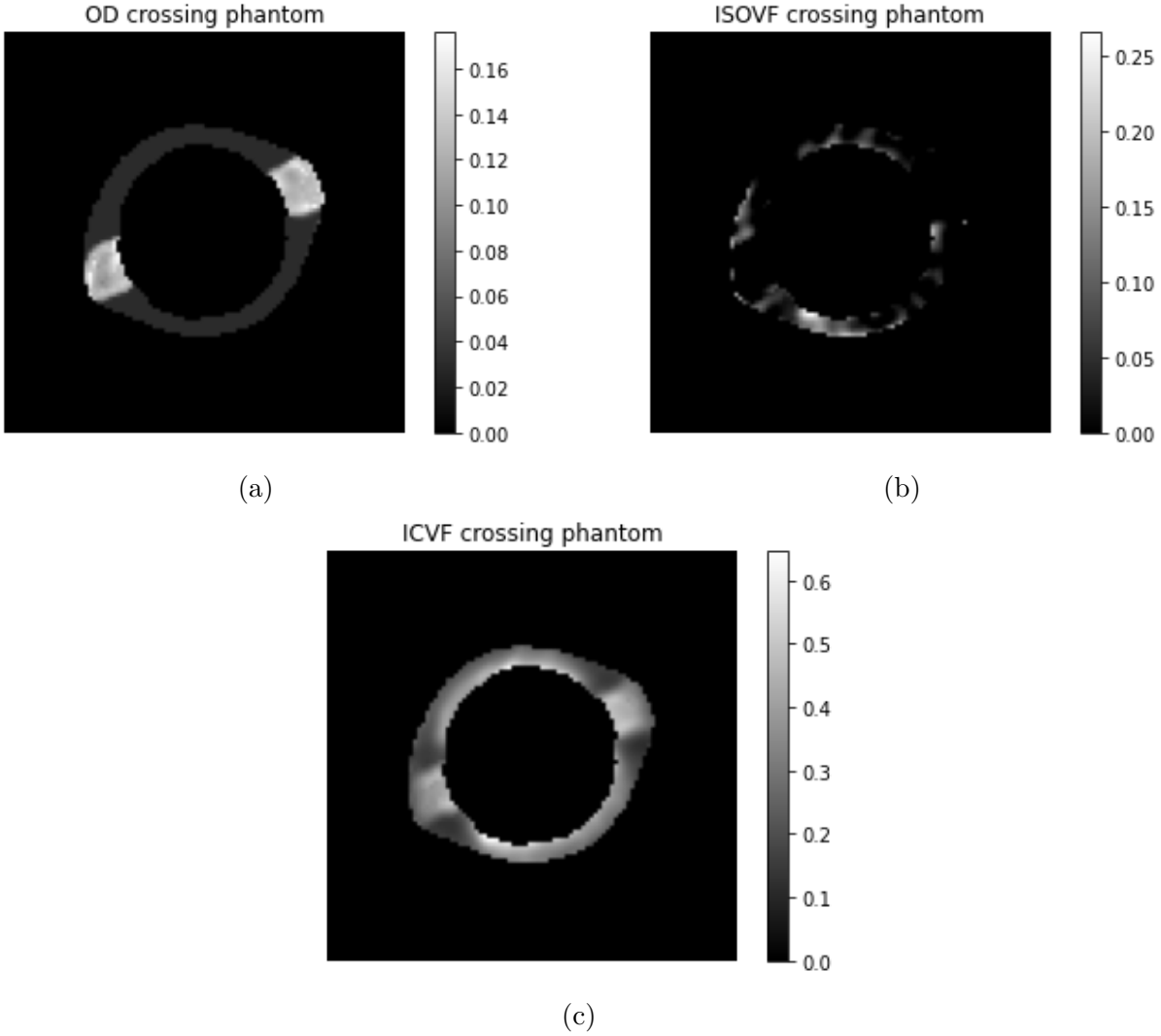

Figure 6.6: (a) orientation dispersion (OD) index, (b) isotropic volume fraction (ISOVF) and (c) intra-cellular volume fraction (ICVF) quantitative maps for the crossing phantom given by the AMICO-NODDI model. The images show how the parameters are distributed over the fibre rings.

Overall, the results of the crossing phantom measurements show that the NODDI metrics have a high degree of temporal stability with consistently low coefficients of variation associated with each parameter. These findings not only confirm the NODDI methodology's robustness but also demonstrate its suitability for longitudinal studies. The measures' inherent consistency contributes to the growing body of evidence proving the applicability of NODDI in a number of research and clinical applications.

Also in the case of the crossing phantom, an investigation was performed to see whether

repetitive data acquisitions could affect measurement accuracy. The study specifically focused on finding out whether the heating of the magnetic field gradient coil after several acquisitions had any effect on the results. To do this, the phantom was scanned eight times, one after the other. The diffusion data was fitted with the Bingham-NODDI and AMICO-NODDI models and the results were extracted from the obtained quantitative maps, in Figure 6.5 and 6.6, using the two binary masks for the rings and crossing region.

In Table 6.11 are displayed the findings derived from the ring region. The table demonstrates that the coefficients of variation are remarkably low, indicating the robustness of the NODDI model outcomes. This means that the Bingham-NODDI results are not influenced by the possible changes in the main magnetic field B_0 caused by the heating of the magnetic field gradient coils, supporting the result already found with the measurements performed with the basic phantom.

Table 6.11: Bingham-NODDI metrics extracted from the region of the rings in the case of eight consecutive measurements. The metrics of interest are the orientation dispersion index (ODI), the β-fraction, the tissue volume fraction, the intra-neurite volume fraction and the parameters to assess the goodness of fit. The CV is computed to assess the stability and robustness of the results.

Bingham-NODDI – Rings region						
	ODI	β-fraction	Tissue v.f.	Intra-neurite v.f.	R^2	MSE
Scan 1	0.0203 ± 0.0035	0.34 ± 0.25	0.96 ± 0.05	0.34 ± 0.09	0.986 ± 0.012	0.0010 ± 0.0009
Scan 2	0.0205 ± 0.0041	0.39 ± 0.25	0.96 ± 0.05	0.34 ± 0.09	0.987 ± 0.013	0.0010 ± 0.0010
Scan 3	0.0203 ± 0.0016	0.38 ± 0.26	0.96 ± 0.05	0.34 ± 0.09	0.986 ± 0.013	0.0010 ± 0.0011
Scan 4	0.0203 ± 0.0014	0.33 ± 0.25	0.96 ± 0.05	0.33 ± 0.09	0.987 ± 0.009	0.0010 ± 0.0007
Scan 5	0.0203 ± 0.0012	0.37 ± 0.25	0.96 ± 0.05	0.34 ± 0.09	0.986 ± 0.012	0.0010 ± 0.0009
Scan 6	0.0204 ± 0.0032	0.34 ± 0.24	0.95 ± 0.05	0.34 ± 0.09	0.987 ± 0.013	0.0010 ± 0.0010
Scan 7	0.0203 ± 0.0015	0.36 ± 0.25	0.96 ± 0.05	0.34 ± 0.09	0.987 ± 0.011	0.0010 ± 0.0009
Scan 8	0.0203 ± 0.0013	0.38 ± 0.24	0.95 ± 0.05	0.34 ± 0.09	0.986 ± 0.012	0.0010 ± 0.0011
CV	0.34 %	5.78 %	0.45 %	0.98 %	0.051 %	0 %

Table 6.12 presents the results obtained from the crossing region of the phantom for the Bingham-NODDI model. It is important to note that these results are consistent and repeatable across all eight acquisitions, with the coefficients of variation for all parameters are below 3 %.

In Table 6.13 are presented the AMICO-NODDI model results of the eight repeated acquisitions for fibre rings of the crossing phantom. These results show a remarkable stability of the AMICO-NODDI model despite the heating of the magnetic field gradient coils. The consistency of the AMICO metrics is by the obtained CVs, which are all below 1 %.

Similarly, Table 6.14 shows the results of the eight repeated acquisitions in the case of the AMICO-NODDI model, extracted from the region in which the two fibre rings intersect. In this case, the OD and the ICVF are consistent with time, having a CV of respectively 0.39 % and 1.12 %. On the other hand, the ISOVF presents with a CV equal to 27.4 %. This high CV may be due to its uneven distribution in the crossing region and also to its low value.

Table 6.12: Bingham-NODDI metrics in the case of eight consecutive measurements extracted from the region of the phantom in which the two fibres cross each other. The metrics of interest are presented together with the CV to assess the consistency of the results despite magnetic field gradient coil heating.

Bingham-NODDI – Crossing region						
	ODI	β-fraction	Tissue v.f.	Intra-neurite v.f.	R^2	MSE
Scan 1	0.08 ± 0.06	0.83 ± 0.20	0.988 ± 0.008	0.40 ± 0.07	0.972 ± 0.011	0.0019 ± 0.0007
Scan 2	0.08 ± 0.05	0.84 ± 0.17	0.987 ± 0.009	0.40 ± 0.07	0.973 ± 0.010	0.0018 ± 0.0007
Scan 3	0.08 ± 0.05	0.84 ± 0.17	0.988 ± 0.010	0.40 ± 0.07	0.972 ± 0.011	0.0019 ± 0.0007
Scan 4	0.08 ± 0.05	0.84 ± 0.18	0.986 ± 0.029	0.38 ± 0.07	0.974 ± 0.010	0.0018 ± 0.0007
Scan 5	0.08 ± 0.06	0.86 ± 0.13	0.987 ± 0.014	0.39 ± 0.07	0.972 ± 0.011	0.0019 ± 0.0007
Scan 6	0.08 ± 0.06	0.83 ± 0.19	0.988 ± 0.007	0.40 ± 0.07	0.972 ± 0.010	0.0019 ± 0.0007
Scan 7	0.08 ± 0.06	0.84 ± 0.17	0.987 ± 0.011	0.39 ± 0.07	0.973 ± 0.010	0.0018 ± 0.0007
Scan 8	0.08 ± 0.06	0.83 ± 0.19	0.986 ± 0.012	0.39 ± 0.07	0.973 ± 0.011	0.0018 ± 0.0007
CV	0 %	1.11 %	0.05 %	1.78 %	0.07 %	2.70 %

Table 6.13: AMICO-NODDI metrics extracted from the region of the rings in the case of eight consecutive measurements. The mean and standard deviation for each metric of interest, including the orientation dispersion (OD) index, isotropic volume fraction (ISOVF), and intra-cellular volume fraction (ICVF), are presented. The coefficient of variation (CV) is calculated to determine whether the magnetic field gradient coil heating affected the measurements.

AMICO-NODDI – Rings region			
	OD	ISOVF	ICVF
Scan 1	0.0300 ± 0.0001	0.06 ± 0.04	0.34 ± 0.09
Scan 2	0.0300 ± 0.0007	0.06 ± 0.04	0.34 ± 0.09
Scan 3	0.0300 ± 0.0005	0.06 ± 0.04	0.34 ± 0.09
Scan 4	0.0300 ± 0.0013	0.06 ± 0.04	0.33 ± 0.09
Scan 5	0.0300 ± 0.0001	0.06 ± 0.04	0.34 ± 0.09
Scan 6	0.0300 ± 0.0002	0.06 ± 0.05	0.34 ± 0.09
Scan 7	0.0300 ± 0.0004	0.06 ± 0.05	0.34 ± 0.09
Scan 8	0.0300 ± 0.0001	0.06 ± 0.05	0.34 ± 0.09
CV	0 %	0 %	0.98 %

Overall, the obtained results demonstrate the stability of the Bingham-NODDI parameters despite the heating of the magnetic field gradient coils. This is of significant importance for several reasons. To begin, when doing neuroimaging investigations, ensuring that the data obtained is reliable and reproducible is critical. If the acquired data were susceptible to magnetic field gradient coil heating and B_0 field changes due to heating, it could cause the NODDI model to not fit the data well, possibly leading to variations in measurements across scans, resulting in inconsistent results. The stability of the data under such conditions ensures accurate interpretations and comparisons between different subjects or time points can be made with confidence.

Furthermore, it is typical in clinical settings to do numerous successive scans on the same person for longitudinal investigations or to evaluate treatment progress. If the NODDI imaging process were to be influenced by heating in the magnetic field gradient coil, it could significantly complicate the interpretation of observed changes between scanning

Table 6.14: The table shows the mean and standard deviation of AMICO-NODDI metrics extracted from the crossing region of the crossing phantom. Metrics of interest include OD index, ISOVF, and ICVF. The CV is calculated to detect magnetic field gradient coil heating effects on measurements.

AMICO-NODDI – Crossing region			
	OD	ISOVF	ICVF
Scan 1	0.128 ± 0.016	0.04 ± 0.02	0.39 ± 0.07
Scan 2	0.127 ± 0.016	0.03 ± 0.02	0.39 ± 0.07
Scan 3	0.127 ± 0.016	0.02 ± 0.02	0.39 ± 0.07
Scan 4	0.128 ± 0.018	0.05 ± 0.03	0.38 ± 0.07
Scan 5	0.128 ± 0.017	0.04 ± 0.03	0.39 ± 0.07
Scan 6	0.127 ± 0.016	0.03 ± 0.02	0.39 ± 0.07
Scan 7	0.127 ± 0.018	0.05 ± 0.03	0.38 ± 0.07
Scan 8	0.128 ± 0.017	0.03 ± 0.03	0.39 ± 0.07
CV	0.39 %	27.4 %	1.12 %

sessions. Because these indicators are stable, physicians and researchers can accurately examine and track neurological disorders or treatment responses without the danger of confounding factors.

Additionally, stability in varying conditions can lead to more efficient use of resources, such as MRI scanner time. Researchers and clinicians can perform more scans in a given time period without affecting data quality, enhancing data collecting efficiency.

In summary, the stability of NODDI parameters despite magnetic field gradient coil heating is crucial for maintaining data quality, enabling reliable longitudinal studies, enhancing scientific validity, and optimizing resource utilization in both clinical and research contexts.

To conclude, the consistent and reliable NODDI results across multiple days have significant implications for both research and clinical applications. This stability is important for detecting changes in brain structure over time and making appropriate patient care decisions. It also increases NODDI's credibility as a tool, enhancing its significance in understanding complicated brain processes. Researchers may confidently examine data and test new hypotheses, and efficient resource management becomes more realistic. In summary, the consistent NODDI results ensure its reliability and promise to expand the knowledge of brain health and illness.

Chapter 7

In vivo Results

In order to assess the repeatability of the diffusion metrics over time, four healthy volunteers were scanned with the $3\,T$ GE Premier scanner and the 21 channels head coil available at OCMR - University of Oxford. The acquisition protocol is described in Section 3.3.

This chapter presents the results of the analysis performed on the healthy volunteers. The acquired *in vivo* diffusion data was fitted with the Tensor and NODDI models, both in the Bignham and AMICO formulations to extract the diffusion metrics with the final aim of assessing the consistency of these results over time. The participants were scanned twice on the same day, with a 10-minute break between the two scans. The results were extracted from specific ROIs, as described in Section 5.2. The ROIs binary masks are shown in Figure 5.4 and Figure 5.5.

The first part of the chapter focuses on the Tensor model results, assessing the repeatability of MD and FA over time. Then, the second part of the chapter presents the Bingham-NODDI results, studying the consistency of the obtained metrics in time. Lastly, the third part of the chapter deals with the results of the AMICO-NODDI model.

7.1 *In vivo* Tensor model results

The acquired data was first fitted with the Tensor model, to obtain the FA and MD quantitative maps. These images are shown in Figure 7.1 together with the structural T1-weighted image to be used as a reference. The shown quantitative maps are registered to the standard space MNI152 in order to be able to extract the results always from the same ROIs, defined in Section 5.2 and shown in Figure 5.4. Specifically, FA and MD values were extracted from the Corpus Callosum, representing white matter, the Thalamus for grey matter and the Ventricles to look at the metrics in the CSF.

The results of FA and MD for the four participants are reported in Table 7.1. As can be observed from the table, as expected, the Corpus Callosum exhibits a higher FA compared to the Thalamus and the Ventricles, remarking the highly organised structure of white matter. On the other hand, the FA in the Ventricles is quite low, reflecting the more isotropic water diffusion in CSF. Table 7.1 also reports the p-values obtained from the paired t-test of FA and MD over time. As it can be clearly seen, all the obtained p-values are sensibly greater than the significance level of 0.05. This implies that the null hypothesis H_0 cannot be rejected, meaning that there is no statistically significant difference between the two values of FA and MD obtained in the first and second scans. In other

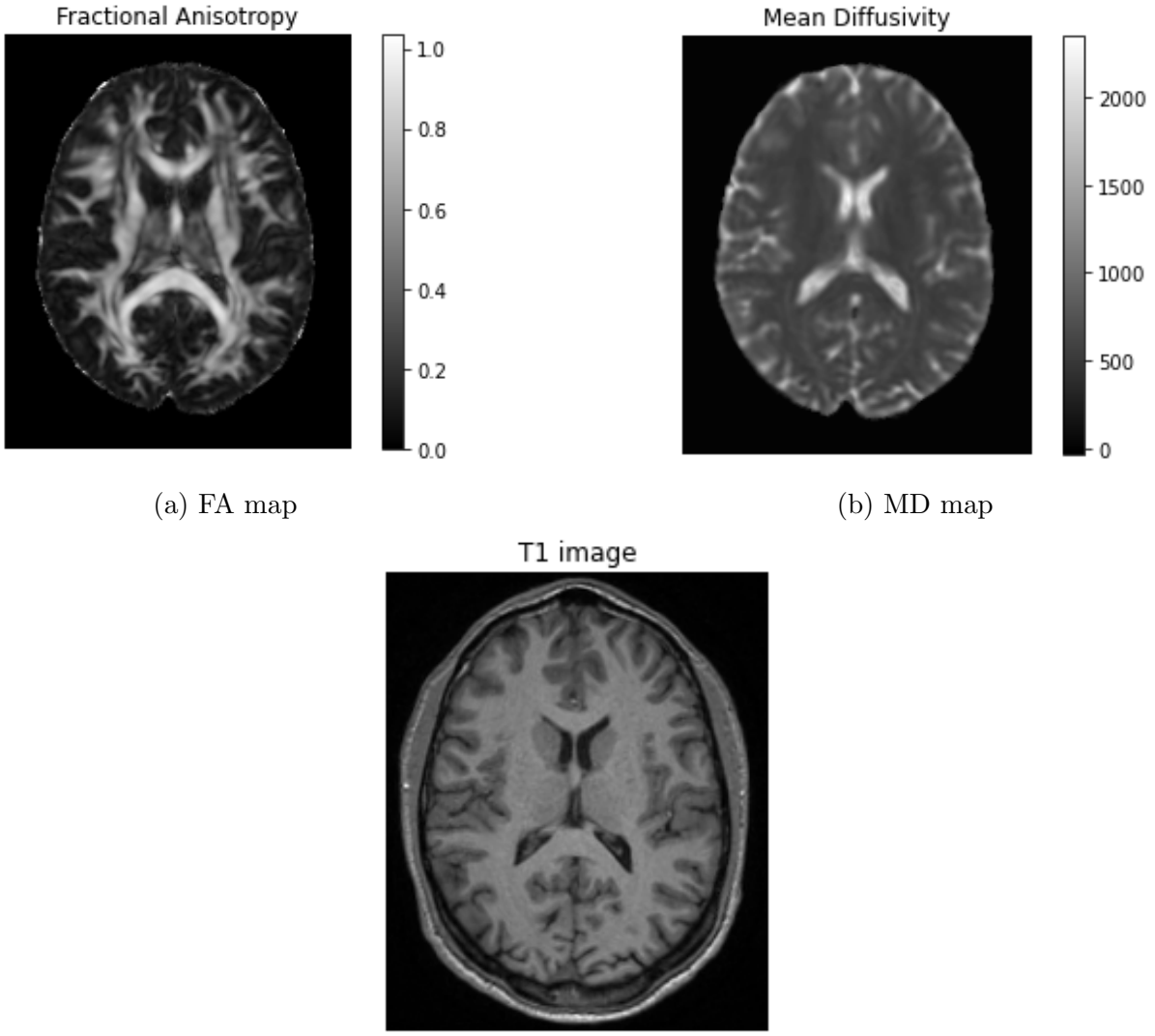

(a) FA map

(b) MD map

(c) Structural T1 image

Figure 7.1: (a) FA and (b) MD expressed in $10^{-6}\,\mathrm{mm}^2/\mathrm{s}$ quantitative maps obtained by fitting the diffusion *in vivo* data to the Tensor model. In (c) the structural T1 weighted image is shown as a reference.

words, there is no strong statistical evidence to claim a significant difference between the FA and MD values from the first and the second scans, ensuring the consistency of the tensor model metrics over time.

In addition to the paired t-test to obtain the p-value, the Bland-Altman analysis is carried out to obtain the Bland-Altman bias, so the median of the differences between the values obtained in the first and second scan, the repeatability coefficient (RC) and the 95% confidence interval (CI). The results of the analysis are shown in Table 7.1. The Bland-Altman bias, representing the median difference between the measurement results obtained from the two scans, both for FA and MD, in all the ROIs is close to zero, indicating that the two measurements being compared, the first and second scans, are in good agreement, on average. This suggests that the measurements from both scans tend to be quite similar, with little to no systematic difference between them.

Moreover, the results reported in Table 7.1 show very low RC for both FA and MD in

Table 7.1: Tensor model results for the four healthy volunteers. The table shows the FA and MD results together with the p-value from the paired t-test, the Bland-Altman Bias, the repeatability coefficient (RC) and the 95% confidence interval (CI) to assess the reproducibility of the results over time.

Tensor model – Brain				
			FA	MD ($\cdot 10^{-3}\,\mathrm{mm}^2/\mathrm{s}$)
Healthy Volunteer 1	Corpus Callosum	Scan 1	0.63 ± 0.17	0.67 ± 0.14
		Scan 2	0.65 ± 0.17	0.64 ± 0.14
	Thalamus	Scan 1	0.28 ± 0.05	0.63 ± 0.06
		Scan 2	0.30 ± 0.06	0.60 ± 0.06
	Ventricles	Scan 1	0.23 ± 0.11	1.68 ± 0.24
		Scan 2	0.24 ± 0.12	1.67 ± 0.24
Healthy Volunteer 2	Corpus Callosum	Scan 1	0.63 ± 0.18	0.65 ± 0.18
		Scan 2	0.63 ± 0.18	0.65 ± 0.18
	Thalamus	Scan 1	0.28 ± 0.06	0.59 ± 0.06
		Scan 2	0.28 ± 0.06	0.60 ± 0.06
	Ventricles	Scan 1	0.20 ± 0.10	1.93 ± 0.27
		Scan 2	0.20 ± 0.10	1.95 ± 0.28
Healthy Volunteer 3	Corpus Callosum	Scan 1	0.62 ± 0.16	0.68 ± 0.12
		Scan 2	0.63 ± 0.17	0.67 ± 0.12
	Thalamus	Scan 1	0.29 ± 0.06	0.63 ± 0.05
		Scan 2	0.30 ± 0.06	0.62 ± 0.05
	Ventricles	Scan 1	0.27 ± 0.13	1.46 ± 0.31
		Scan 2	0.27 ± 0.13	1.47 ± 0.32
Healthy Volunteer 4	Corpus Callosum	Scan 1	0.60 ± 0.18	0.68 ± 0.14
		Scan 2	0.60 ± 0.19	0.65 ± 0.13
	Thalamus	Scan 1	0.29 ± 0.07	0.66 ± 0.10
		Scan 2	0.29 ± 0.07	0.64 ± 0.09
	Ventricles	Scan 1	0.18 ± 0.08	1.96 ± 0.28
		Scan 2	0.19 ± 0.09	1.93 ± 0.27
p-value	Corpus Callosum		0.2152	0.1018
	Thalamus		0.2152	0.2394
	Ventricles		0.1817	0.8361
Bland-Altman Bias	Corpus Callosum		0.0050	−0.0175
	Thalamus		0.0050	−0.0150
	Ventricles		0.0050	0
RC	Corpus Callosum		0.0200	0.0050
	Thalamus		0.0200	0.0100
	Ventricles		0.0100	0.0200
95% CI	Corpus Callosum		0-0.02	−0.03-0.005
	Thalamus		0-0.02	−0.03-0.01
	Ventricles		0-0.01	−0.03-0.02

all the ROIs taken into consideration, assessing the consistency and reproducibility of the FA and MD results over time.

Finally, the 95% Confidence Interval for the repeatability coefficient (RC) presents a range

within which a high level of confidence can be expressed regarding the true value of RC. In this study, the obtained 95% Confidence Intervals are very narrow and they include zero, meaning that the measurements obtained from the two scans being compared are not significantly different from each other within the given level of confidence.

Overall, the obtained p-values from the results consistently show that the null hypothesis cannot be rejected, indicating no significant difference in FA and MD values between the first and second scans. Moreover, the Bland-Altman bias, close to zero for all ROIs, underscores the strong agreement between measurements obtained from both scans. The low values of the RC in conjunction with narrow 95% confidence intervals further reinforce the high level of confidence in the consistency of measurements. These findings suggest that the diffusion metrics obtained from the Tensor model are stable and mere indicators of brain microstructure, making them suitable for longitudinal studies and clinical applications.

7.2 Bingham-NODDI *in vivo* results

The data obtained from the scans of the four healthy volunteers were fitted also with the Bingham-NODDI diffusion model with the final aim of assessing its repeatability and stability over time. The metrics of interest are the same as for the phantoms. The obtained quantitative maps are shown in Figure 7.2.

The results were extracted from the quantitative maps by using the ROIs shown in Figure 5.4 and 5.5, excluding the Ventricles since in the tissue component of the Bingham model, the signal from the CSF is suppressed. Specifically, results were extracted from the Genu and Splenium of the Corpus Callosum (CC) and from the anterior and posterior limbs of the Internal Capsule (IC) for white matter. Instead, results were extracted from the Thalamus, Caudate and Putamen regions for grey matter.

In Figure 7.2b, a great contrast can be observed between white and grey matter in the ODI quantitative map. This contrast arises from the difference in the ODI index between the two tissue types, with white matter having a significantly lower ODI than grey matter. The lower index value indicates a more structured neurite arrangement in white matter, with very little neurite dispersion. On the other hand, the relatively higher ODI in grey matter suggests a greater level of neurite orientation dispersion. Additionally, Figure 7.2c shows how in the Ventricles the tissue volume fraction is very close to zero, indicating the absence of cells. On the other hand, white and grey matter presents with a tissue volume fraction almost equal to one, highlighting the very low presence of inter-cellular water, water that fills the spaces between adjacent cells in a tissue. As shown in Figure 7.2d, it is evident that the intra-neurite volume fraction is greater in white matter than in grey matter. This indicates that white matter has a higher density of neurites when compared to grey matter.

Figure 7.2e and 7.2f respectively show the R^2 and the MSE in the case of the *in vivo* acquisitions. Ideally, the MSE and R^2 should not show any structure of the underlying data, meaning the model can at least fit the data equally well everywhere. However, the structure of different brain structures in Bingham-NODDI can still be seen, but they are becoming less obvious to see than in Ball and Stick or Watson-NODDI, the original formulation of the NODDI model. The much lower R^2 in white matter could be due to several factors. In its current formulation, the Bingham-NODDI models the neurite orientation

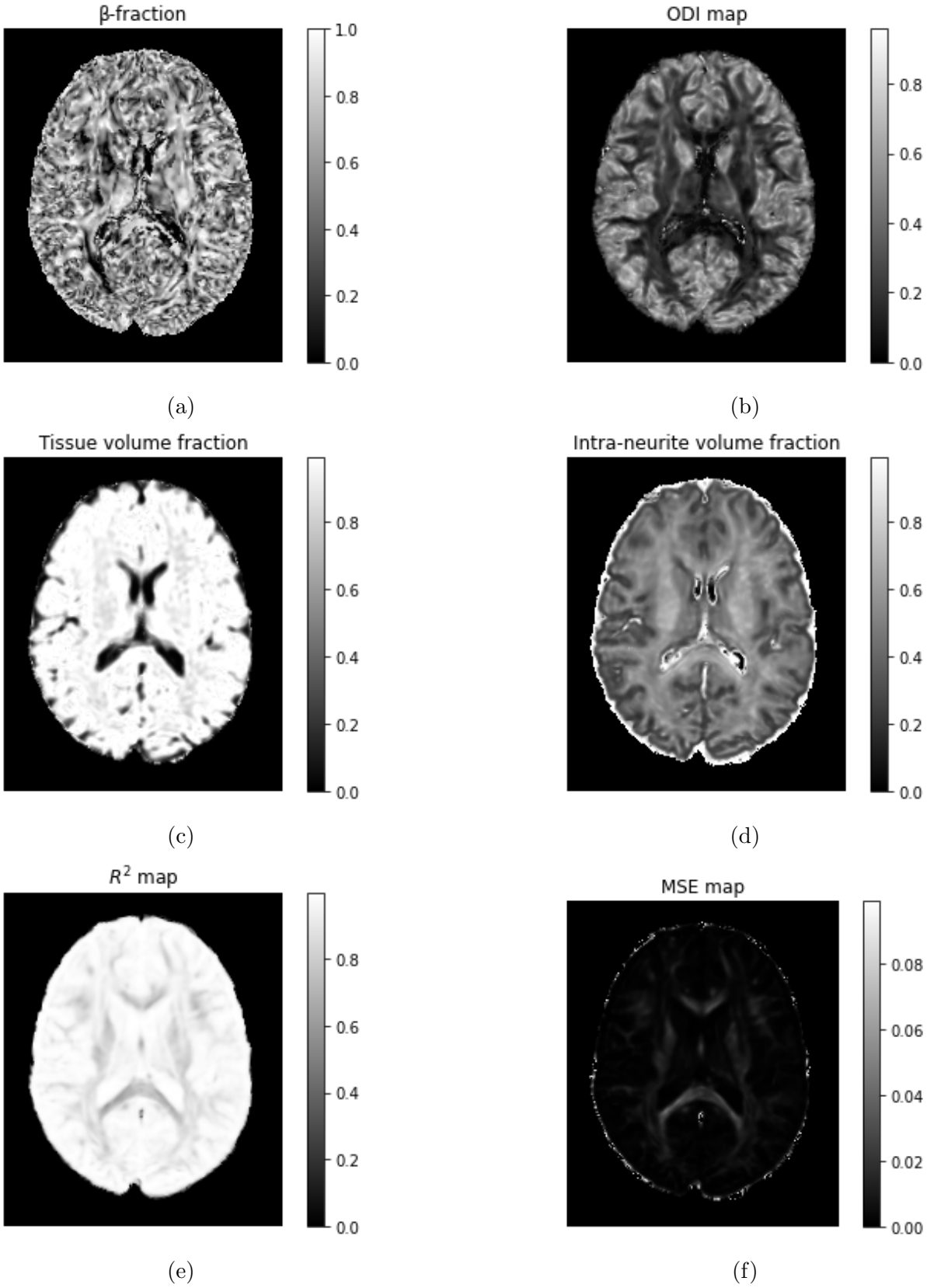

Figure 7.2: Brain Bingham-NODDI quantitative maps obtained by fitting the diffusion *in vivo* data to the Bingham-NODDI model. The maps represent (a) β-fraction, (b) ODI, (c) tissue volume fraction, (d) intra-neurite volume fraction, (e) R^2 coefficient and (f) the mean squared error.

distribution with a single Watson density and hence ignores fibre crossings which are a distinctive feature of human connectional neuroanatomy. According to [60], the majority of white matter voxels feature multiple fibre bundles whose accurate representation requires two or more Bingham distributions. In addition, NODDI assumes a single and fixed intrinsic diffusivity λ, which in human *in vivo* studies is set equal to $1.7\,\mu\text{m}^2/\text{ms}$. Kaden et al. [60] demonstrated how λ actually varies significantly over the brain white matter, with an average value that is considerably higher than the one assumed in NODDI. This underestimation of λ in NODDI gives rise to a systematic overestimation of free-water content in the cerebral white matter and may adversely affect the recovery of other parameters such as their neurite density index.

The results extracted from the white matter ROIs are presented in Table 7.2, together with the p-value, the Bland-Altman Bias, the repeatability coefficient, and the 95% confidence interval for each ROI.

As evident from Table 7.2, the β-fraction demonstrates remarkable stability by maintaining an identical value across both initial and subsequent scans. Consequently, the p-value remains undefined, indicated as "//" in the table, due to the absence of variation, and all metrics derived from the Bland-Altman analysis register as zero.
Turning attention to the Orientation Dispersion Index (ODI), its p-values are significantly higher than the significance level of 0.05, indicating a lack of statistically significant differences. Reinforcing this finding, the Bland-Altman biases and repeatability coefficients converge close to zero, affirming the robust stability of the ODI metric across time.
Likewise, similar observations apply to the tissue volume fraction. The values closely approach unity within white matter, indicating minimal presence of intercellular water in this tissue. The p-values across all regions of interest exceed the threshold of 0.05, implying the inability to reject the null hypothesis H_0. This non-rejection underscores the absence of statistically significant fluctuations in the tissue volume fraction, thereby pointing out the consistency of the Bingham-NODDI metrics across temporal intervals. This coherence is furthermore sustained by the low Bland-Altman biases and the small values characterising the repeatability coefficients, collectively highlighting the strong stability of the tissue volume fraction across time.
Finally, high p-values and very low Bland-Altman biases and repeatability coefficients are obtained also for the intra-neurite volume fraction. This means that also this metric can be considered stable and consistent over time, without any statistically relevant variation between the two scans.

Overall, the analysis highlights the inherent stability of NODDI metrics over time in white matter. The repeated measurements consistently reveal minimal fluctuations in metrics such as the β-fraction, Orientation Dispersion Index (ODI), tissue volume fraction, and intra-neurite volume fraction. This steadiness is further substantiated by the high p-values and negligible deviations in the computed values. As a result, these metrics present a dependable and enduring measurement framework, well-suited for situations that demand consistent and accurate results across multiple scans over time.

Similarly to the discussion made for the results extracted from white matter regions, Table 7.3 presents the Bingham-NODDI metrics results extracted from grey matter ROIs, being the Thalamus, the Caudate and the Putamen.

Grey matter presents with a higher ODI with respect to white matter. This is related to the fact that grey matter does not exhibit organised fibre tracts like white matter, meaning that the neurite fibres are less packed and organised in coherent paths, resulting

Table 7.2: Bingham-NODDI model results for the four healthy volunteers in white matter. The table shows the Bingham-NODDI metrics extracted from four ROIs: the Genu and Splenium of the Corpus Callosum and the anterior and posterior limbs of the Internal Capsule. The p-value from the paired t-test, the Bland-Altman Bias, the repeatability coefficient (RC) and the 95% confidence interval are shown to assess the reproducibility of the results over time. The p-value is not defined when measurements show no variation over time, indicated by "//".

Bingham-NODDI model – White Matter								
			β-fraction	ODI	Tissue v.f.	Intra-neurite v.f.	R^2	MSE
HV 1	Genu CC	Scan 1	0.5 ± 0.2	0.15 ± 0.09	0.84 ± 0.18	0.52 ± 0.09	0.87 ± 0.07	0.009 ± 0.006
		Scan 2	0.5 ± 0.2	0.15 ± 0.08	0.87 ± 0.17	0.53 ± 0.08	0.86 ± 0.08	0.010 ± 0.006
	Splenium CC	Scan 1	0.6 ± 0.3	0.12 ± 0.08	0.88 ± 0.13	0.59 ± 0.08	0.82 ± 0.08	0.013 ± 0.007
		Scan 2	0.6 ± 0.3	0.11 ± 0.08	0.91 ± 0.12	0.59 ± 0.08	0.81 ± 0.08	0.014 ± 0.007
	Anterior limb IC	Scan 1	0.4 ± 0.2	0.21 ± 0.08	0.92 ± 0.07	0.56 ± 0.08	0.88 ± 0.05	0.007 ± 0.004
		Scan 2	0.4 ± 0.3	0.21 ± 0.09	0.95 ± 0.04	0.58 ± 0.07	0.87 ± 0.06	0.008 ± 0.004
	Posterior limb IC	Scan 1	0.5 ± 0.2	0.20 ± 0.08	0.88 ± 0.05	0.64 ± 0.07	0.86 ± 0.06	0.009 ± 0.004
		Scan 2	0.5 ± 0.2	0.20 ± 0.08	0.93 ± 0.04	0.66 ± 0.07	0.84 ± 0.07	0.009 ± 0.005
HV 2	Genu CC	Scan 1	0.5 ± 0.3	0.14 ± 0.08	0.85 ± 0.19	0.54 ± 0.08	0.87 ± 0.07	0.009 ± 0.006
		Scan 2	0.5 ± 0.3	0.14 ± 0.08	0.85 ± 0.19	0.53 ± 0.08	0.87 ± 0.08	0.009 ± 0.006
	Splenium CC	Scan 1	0.6 ± 0.3	0.13 ± 0.09	0.90 ± 0.13	0.59 ± 0.09	0.82 ± 0.09	0.014 ± 0.008
		Scan 2	0.6 ± 0.3	0.13 ± 0.09	0.90 ± 0.13	0.59 ± 0.08	0.82 ± 0.09	0.013 ± 0.008
	Anterior limb IC	Scan 1	0.4 ± 0.2	0.21 ± 0.07	0.95 ± 0.04	0.60 ± 0.07	0.87 ± 0.06	0.008 ± 0.004
		Scan 2	0.4 ± 0.2	0.20 ± 0.07	0.94 ± 0.04	0.60 ± 0.06	0.87 ± 0.05	0.008 ± 0.004
	Posterior limb IC	Scan 1	0.5 ± 0.2	0.19 ± 0.08	0.92 ± 0.04	0.68 ± 0.06	0.84 ± 0.05	0.009 ± 0.003
		Scan 2	0.5 ± 0.2	0.19 ± 0.08	0.92 ± 0.04	0.67 ± 0.06	0.84 ± 0.05	0.009 ± 0.003
HV 3	Genu CC	Scan 1	0.5 ± 0.3	0.14 ± 0.08	0.90 ± 0.11	0.47 ± 0.09	0.87 ± 0.07	0.009 ± 0.005
		Scan 2	0.5 ± 0.3	0.14 ± 0.08	0.90 ± 0.11	0.48 ± 0.09	0.87 ± 0.07	0.009 ± 0.005
	Splenium CC	Scan 1	0.6 ± 0.3	0.12 ± 0.09	0.90 ± 0.12	0.55 ± 0.07	0.84 ± 0.07	0.012 ± 0.006
		Scan 2	0.6 ± 0.3	0.12 ± 0.09	0.90 ± 0.12	0.55 ± 0.07	0.83 ± 0.08	0.012 ± 0.008
	Anterior limb IC	Scan 1	0.5 ± 0.3	0.19 ± 0.08	0.94 ± 0.05	0.56 ± 0.06	0.88 ± 0.04	0.007 ± 0.003
		Scan 2	0.5 ± 0.3	0.20 ± 0.08	0.94 ± 0.04	0.57 ± 0.06	0.88 ± 0.05	0.007 ± 0.003
	Posterior limb IC	Scan 1	0.6 ± 0.2	0.20 ± 0.08	0.91 ± 0.05	0.63 ± 0.06	0.88 ± 0.05	0.007 ± 0.003
		Scan 2	0.6 ± 0.2	0.20 ± 0.08	0.92 ± 0.04	0.64 ± 0.06	0.87 ± 0.05	0.008 ± 0.003
HV 4	Genu CC	Scan 1	0.5 ± 0.3	0.14 ± 0.09	0.90 ± 0.14	0.49 ± 0.08	0.87 ± 0.07	0.009 ± 0.006
		Scan 2	0.5 ± 0.3	0.14 ± 0.09	0.90 ± 0.15	0.50 ± 0.08	0.86 ± 0.07	0.009 ± 0.006
	Splenium CC	Scan 1	0.5 ± 0.3	0.13 ± 0.11	0.91 ± 0.13	0.53 ± 0.07	0.84 ± 0.08	0.012 ± 0.007
		Scan 2	0.5 ± 0.3	0.14 ± 0.10	0.92 ± 0.11	0.54 ± 0.07	0.83 ± 0.08	0.012 ± 0.008
	Anterior limb IC	Scan 1	0.4 ± 0.2	0.21 ± 0.08	0.94 ± 0.05	0.54 ± 0.06	0.89 ± 0.05	0.007 ± 0.003
		Scan 2	0.4 ± 0.2	0.22 ± 0.07	0.95 ± 0.04	0.55 ± 0.06	0.88 ± 0.05	0.007 ± 0.004
	Posterior limb IC	Scan 1	0.5 ± 0.2	0.19 ± 0.08	0.91 ± 0.05	0.61 ± 0.06	0.86 ± 0.05	0.009 ± 0.003
		Scan 2	0.5 ± 0.2	0.19 ± 0.08	0.92 ± 0.04	0.63 ± 0.06	0.85 ± 0.05	0.009 ± 0.004
p-value	Genu Corpus Callosum		//	//	0.3910	0.3910	0.1817	0.3910
	Splenium Corpus Callosum		//	1.000	0.2522	0.3910	0.1817	1.000
	Anterior limb IC		//	0.6376	0.4444	0.0917	0.1817	0.3910
	Posterior limb IC		//	//	0.2126	0.2522	0.0917	0.3910
B-A Bias	Genu Corpus Callosum		0	0	0.0075	0.005	−0.005	0.0003
	Splenium Corpus Callosum		0	0	0.010	0.0025	−0.0075	0
	Anterior limb IC		0	0.0025	0.0075	0.010	−0.005	0.0003
	Posterior limb IC		0	0	0.0175	0.010	−0.010	0.0003
RC	Genu Corpus Callosum		0	0	0.0225	0.010	0	0.0008
	Splenium Corpus Callosum		0	0.0075	0.025	0.0075	−0.0025	0.0008
	Anterior limb IC		0	0.010	0.0225	0.0175	0	0.0008
	Posterior limb IC		0	0	0.040	0.020	−0.0025	0.0008
95% CI	Genu Corpus Callosum		0-0	0-0	0-0.0225	−0.005-0.010	−0.0100-0	0-0.0008
	Splenium Corpus Callosum		0-0	−0.0075-0.0075	0-0.025	0-0.0075	−0.010- − 0.0025	−0.0008-0.0008
	Anterior limb IC		0-0	−0.005-0.01	−0.005-0.0225	0.0025-0.0175	−0.010-0	0-0.0008
	Posterior limb IC		0-0	0-0	0.0025-0.040	−0.0026-0.0200	−0.0175- − 0.0025	0-0.0008

in a lower ODI. Moreover, the intra-neurite volume fraction is lower when compared to the values obtained for white matter, indicating a slightly lower density of neurites in this tissue. On the other hand, grey matter exhibits a higher tissue volume fraction, meaning that grey matter contains less inter-cellular water than white matter. This could be related to the fact that in grey matter, the cellular elements are packed more closely together, leaving less extracellular space for water: neuronal cell bodies are densely arranged, which can restrict the amount of extracellular fluid.

As it can be seen from Table 7.3, all the Bingham-NODDI metrics show great stability

Table 7.3: Bingham-NODDI model results for the four healthy volunteers in grey matter. The table shows the Bingham-NODDI metrics extracted from three ROIs: the Thalamus, Caudate and Putamen, which are deep grey matter structures. The p-value from the paired t-test, the Bland-Altman Bias, the repeatability coefficient (RC) and the 95% confidence interval are shown to assess the reproducibility of the results over time. The p-value is not defined when measurements show no variation over time, indicated by "//".

Bingham-NODDI model – Grey Matter								
			β-fraction	ODI	Tissue v.f.	intra-neurite v.f.	R^2	MSE
HV 1	Thalamus	Scan 1	0.6 ± 0.2	0.29 ± 0.08	0.95 ± 0.09	0.43 ± 0.06	0.96 ± 0.01	0.0019 ± 0.0006
		Scan 2	0.58 ± 0.19	0.29 ± 0.08	0.95 ± 0.09	0.46 ± 0.06	0.95 ± 0.02	0.003 ± 0.001
	Caudate	Scan 1	0.6 ± 0.2	0.49 ± 0.13	0.94 ± 0.11	0.43 ± 0.06	0.97 ± 0.01	0.0019 ± 0.0006
		Scan 2	0.6 ± 0.2	0.48 ± 0.13	0.95 ± 0.10	0.44 ± 0.06	0.97 ± 0.01	0.0019 ± 0.0007
	Putamen	Scan 1	0.5 ± 0.2	0.51 ± 0.13	0.99 ± 0.01	0.45 ± 0.03	0.96 ± 0.02	0.0022 ± 0.0012
		Scan 2	0.5 ± 0.2	0.51 ± 0.14	0.99 ± 0.01	0.45 ± 0.03	0.96 ± 0.02	0.0024 ± 0.0012
HV 2	Thalamus	Scan 1	0.6 ± 0.2	0.29 ± 0.08	0.94 ± 0.13	0.47 ± 0.06	0.95 ± 0.02	0.003 ± 0.001
		Scan 2	0.6 ± 0.2	0.29 ± 0.08	0.94 ± 0.11	0.46 ± 0.06	0.95 ± 0.02	0.0028 ± 0.0009
	Caudate	Scan 1	0.65 ± 0.19	0.45 ± 0.13	0.89 ± 0.19	0.46 ± 0.08	0.97 ± 0.02	0.0021 ± 0.0009
		Scan 2	0.62 ± 0.19	0.44 ± 0.13	0.89 ± 0.18	0.46 ± 0.08	0.97 ± 0.02	0.0021 ± 0.0010
	Putamen	Scan 1	0.50 ± 0.19	0.53 ± 0.11	0.99 ± 0.01	0.50 ± 0.04	0.95 ± 0.02	0.0027 ± 0.0011
		Scan 2	0.5 ± 0.2	0.53 ± 0.12	0.99 ± 0.01	0.49 ± 0.04	0.95 ± 0.02	0.0026 ± 0.0011
HV 3	Thalamus	Scan 1	0.6 ± 0.2	0.27 ± 0.08	0.97 ± 0.06	0.43 ± 0.05	0.96 ± 0.01	0.0027 ± 0.0007
		Scan 2	0.6 ± 0.2	0.27 ± 0.08	0.97 ± 0.06	0.44 ± 0.05	0.95 ± 0.01	0.0028 ± 0.0007
	Caudate	Scan 1	0.58 ± 0.19	0.49 ± 0.13	0.97 ± 0.06	0.42 ± 0.07	0.97 ± 0.01	0.0019 ± 0.0008
		Scan 2	0.6 ± 0.2	0.49 ± 0.13	0.97 ± 0.06	0.43 ± 0.08	0.97 ± 0.01	0.0019 ± 0.0008
	Putamen	Scan 1	0.5 ± 0.2	0.54 ± 0.12	0.99 ± 0.01	0.46 ± 0.03	0.97 ± 0.02	0.0020 ± 0.0009
		Scan 2	0.51 ± 0.19	0.54 ± 0.12	0.99 ± 0.01	0.48 ± 0.03	0.96 ± 0.02	0.0022 ± 0.0009
HV 4	Thalamus	Scan 1	0.6 ± 0.2	0.28 ± 0.08	0.97 ± 0.07	0.43 ± 0.06	0.95 ± 0.01	0.0029 ± 0.0009
		Scan 2	0.6 ± 0.2	0.29 ± 0.08	0.97 ± 0.06	0.45 ± 0.06	0.95 ± 0.02	0.0031 ± 0.0009
	Caudate	Scan 1	0.6 ± 0.2	0.46 ± 0.12	0.93 ± 0.13	0.41 ± 0.07	0.97 ± 0.01	0.0016 ± 0.0007
		Scan 2	0.6 ± 0.2	0.45 ± 0.12	0.94 ± 0.12	0.43 ± 0.08	0.97 ± 0.01	0.0019 ± 0.0007
	Putamen	Scan 1	0.5 ± 0.2	0.52 ± 0.12	0.99 ± 0.01	0.46 ± 0.03	0.96 ± 0.01	0.0023 ± 0.0011
		Scan 2	0.5 ± 0.2	0.51 ± 0.12	0.99 ± 0.01	0.48 ± 0.03	0.96 ± 0.02	0.0025 ± 0.0011
p-value	Thalamus		0.3910	0.3910	//	0.2394	0.1817	0.3623
	Caudate		0.8240	0.1817	0.1817	0.4950	//	0.3910
	Putamen		0.3910	0.3910	//	0.3910	0.3910	0.1942
B-A Bias	Thalamus		−0.0050	0.0025	0	0.0125	−0.005	0.0003
	Caudate		−0.0025	−0.0075	0.0050	0.010	0	0.0001
	Putamen		0.0025	−0.0025	0	0.0075	−0.0025	0.0001
RC	Thalamus		0	0.0075	0	0.025	0	0.0009
	Caudate		0.0100	−0.0025	0.010	0.0175	0	0.0002
	Putamen		0.0075	0	0	0.020	0	0.0002
95% CI	Thalamus		−0.015-0	0-0.0075	0-0	−0.0025-0.025	−0.01-0	−0.0001-0.0009
	Caudate		−0.02-0.01	−0.01-0.0025	0-0.01	0.0025-0.0175	0-0	0-0.0002
	Putamen		0-0.075	−0.0075-0	0-0	−0.005-0.02	−0.0075-0	0-0.0002

and repeatability over time, with p-values of the paired t-test sensibly greater than 0.05, meaning the observed differences in the results between the first and second scans are not statistically significant. Moreover, the Bland-Altman biases are all very close to zero, which indicates that there is good agreement and minimal systematic difference between the two scans.

Another result that supports the stability of the Bingham-NODDI metrics over time is the repeatability coefficient, which presents values very close to zero for all the metrics and ROIs analysed. When the repeatability coefficient is close to zero, it suggests that the variability between measurements is minimal, and the measurements are consistent and highly repeatable. In other words, a repeatability coefficient close to zero signifies that the measurements are very consistent and that the method is producing highly reproducible results.

Finally, all the Bingham-NODDI metrics present a narrow 95% confidence interval for the

repeatability coefficient, indicating high agreement and precision between the two measurements. This suggests that the two scans being compared are in strong agreement, with consistent and repeatable measurements.

To summarise, the Bingham-NODDI diffusion model was carefully tested using *in vivo* data from four healthy volunteers. The quantitative maps produced, which include measures like β-fraction, ODI, tissue volume fraction, and intra-neurite volume fraction, show exceptional repeatability and stability over time in both white and grey matter regions of interest. Significantly, the estimated p-values, which indicate the model's reliability, were consistently greater than 0.05, confirming the Bingham-NODDI approach's robustness. Furthermore, the Bland-Altman analysis demonstrated low bias and tight limits of agreement between the two acquisitions for every participant of the study. These consistent findings highlight the Bingham-NODDI model's stability and reliability over time as a tool for evaluating tissue microstructure in different brain areas.

7.3 AMICO-NODDI *in vivo* results

The same diffusion-weighted MRI data was also fitted to the linear implementation of the NODDI model. In this case, the model employs the Watson distribution to model the neurite dispersion, instead of the Bingham distribution. The analysis pipeline is the same one used in the case of the Bingham-NODDI model, with the final aim of assessing the stability and repeatability of the NODDI model.

The quantitative maps obtained from the AMICO-NODDI fit are shown in Figure 7.3, and they represent the OD (orientation dispersion) index, the ICVF (intra-cellular volume fraction), which corresponds to the intra-neurite volume fraction of the Bingham-NODDI, and the ISOVF (isotropic volume fraction) representing the CSF in the brain.

The obtained OD map, shown in Figure 7.3a, is very similar to the one obtained with the Bingham-NODDI model, shown in Figure 7.2b. One great difference is related to the ventricles: while the Bingham-NODDI model suppresses the signal of the CSF compartment, in the AMICO-NODDI model the ventricles present an OD index very close to one, representing the total absence of a compact and coherent neurite structure in the CSF.

The second quantitative map is the ICVF, shown in Figure 7.3b. This map represents the volume fraction occupied by neurites in each voxel. Also, this map looks very similar to the intra-neurite volume fraction map obtained with the Bingham-NODDI model and shown in Figure 7.2d. One difference between the two maps that can be observed is, again, the values obtained in the ventricles: in the case of the AMICO-NODDI model, the ventricles have an ICVF equal to zero, highlighting the absence of neurites in the CSF.

The last quantitative map obtained as a result of the fitting of the AMICO-NODDI to the acquired data is the ISOVF map, which represents the voxel's fraction occupied by CSF in the brain. This map, shown in Figure 7.3c, is complementary with respect to one to the tissue volume fraction map of the Bingham-NODDI model, shown in Figure 7.2c. In the ISOVF map can be clearly seen that the ventricles appear bright, with a voxel value very close to one indicating the complete absence of cells organised into tissues in the CSF.

The AMICO-NODDI metrics were extracted from the same ROIs used to extract the Bingham-NODDI results. These ROIs are displayed in Figure 5.4 and Figure 5.5, with

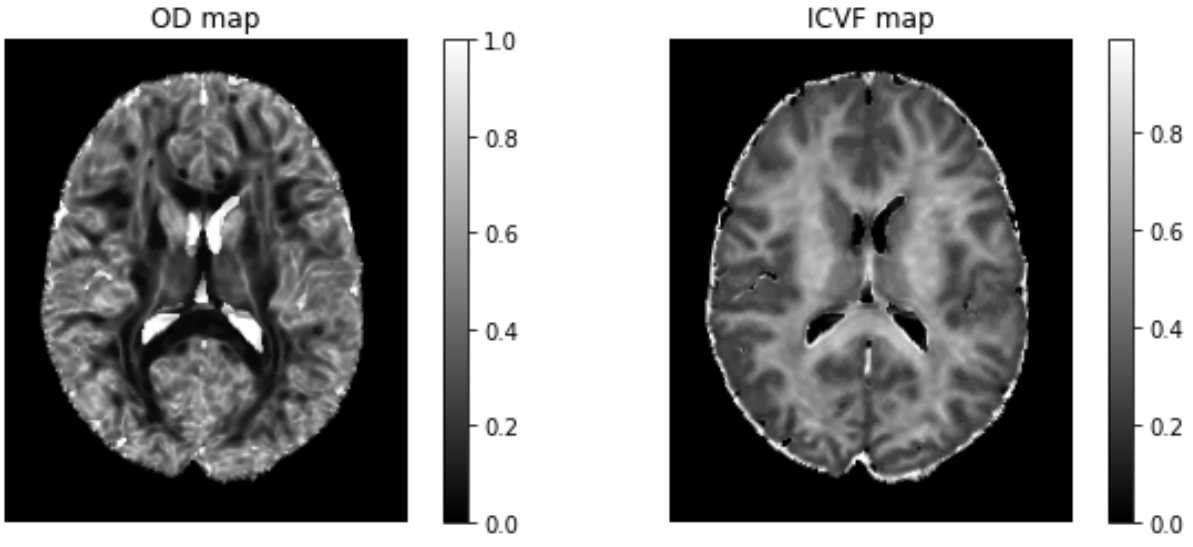

(a)

(b)

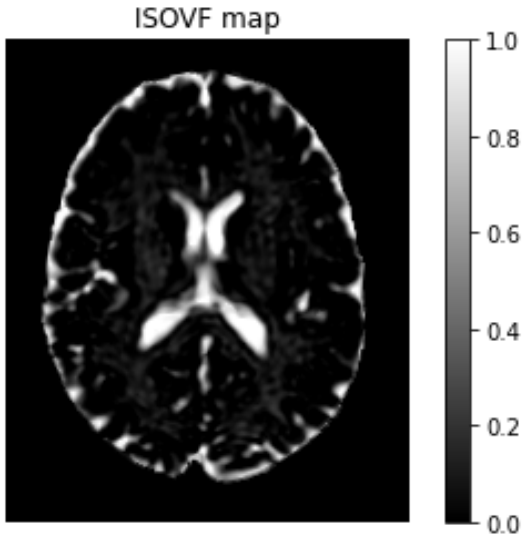

(c)

Figure 7.3: AMICO-NODDI quantitative maps for the brain: (a) OD map representing the orientation dispersion of the neurites, (b) ICVF map representing the intra-neurite volume fraction in each voxel, and (c) ISOVF map depicting the CSF component in each voxel.

the exclusion of the ventricles. Table 7.4 presents the AMICO-NODDI results in white matter. It can be seen that the OD values are slightly lower compared to the values obtained for the ODI in the Bingham-NODDI model. However, there is a high standard deviation associated with these OD values, sometimes even equal to the mean values themselves. Overall, the low OD values indicate the organised white matter structure which contains compact fibre bundles. The obtained p-values for the OD index show that the observed differences in values between the first and second scans are not statistically significant, ensuring the repeatability of the results over time. Additionally, the repeatability of the OD results over time is confirmed by the very low Bland-Altman bias in the four ROIs, together with the very low repeatability coefficient and the narrow 95%

Table 7.4: AMICO-NODDI model results for the four healthy volunteers in white matter. The table shows the AMICO-NODDI metrics in white matter together with the p-value from the paired t-test, the Bland-Altman Bias, the repeatability coefficient (RC) and the 95% confidence interval (CI) to assess the reproducibility of the results over time. The p-value is not defined when measurements show no variation over time, indicated by "//".

AMICO-NODDI model – White matter					
			OD	ICVF	ISOVF
Healthy Volunteer 1	Genu CC	Scan 1	0.13 ± 0.13	0.54 ± 0.12	0.19 ± 0.18
		Scan 2	0.13 ± 0.11	0.55 ± 0.11	0.16 ± 0.19
	Splenium CC	Scan 1	0.09 ± 0.08	0.63 ± 0.10	0.15 ± 0.14
		Scan 2	0.09 ± 0.08	0.63 ± 0.10	0.12 ± 0.13
	Anterior limb IC	Scan 1	0.15 ± 0.10	0.57 ± 0.09	0.08 ± 0.06
		Scan 2	0.16 ± 0.10	0.59 ± 0.08	0.05 ± 0.05
	Posterior limb IC	Scan 1	0.16 ± 0.09	0.65 ± 0.08	0.12 ± 0.06
		Scan 2	0.17 ± 0.09	0.66 ± 0.07	0.08 ± 0.04
Healthy Volunteer 2	Genu CC	Scan 1	0.14 ± 0.14	0.56 ± 0.12	0.18 ± 0.21
		Scan 2	0.14 ± 0.14	0.55 ± 0.12	0.17 ± 0.21
	Splenium CC	Scan 1	0.11 ± 0.10	0.63 ± 0.11	0.13 ± 0.13
		Scan 2	0.11 ± 0.09	0.63 ± 0.10	0.13 ± 0.14
	Anterior limb IC	Scan 1	0.15 ± 0.08	0.60 ± 0.08	0.05 ± 0.04
		Scan 2	0.15 ± 0.08	0.61 ± 0.07	0.05 ± 0.05
	Posterior limb IC	Scan 1	0.16 ± 0.07	0.70 ± 0.07	0.08 ± 0.04
		Scan 2	0.16 ± 0.07	0.69 ± 0.07	0.09 ± 0.04
Healthy Volunteer 3	Genu CC	Scan 1	0.10 ± 0.09	0.50 ± 0.11	0.13 ± 0.11
		Scan 2	0.10 ± 0.08	0.51 ± 0.10	0.12 ± 0.11
	Splenium CC	Scan 1	0.10 ± 0.09	0.59 ± 0.09	0.13 ± 0.12
		Scan 2	0.10 ± 0.09	0.60 ± 0.09	0.13 ± 0.12
	Anterior limb IC	Scan 1	0.15 ± 0.09	0.56 ± 0.07	0.06 ± 0.05
		Scan 2	0.15 ± 0.09	0.57 ± 0.07	0.06 ± 0.05
	Posterior limb IC	Scan 1	0.19 ± 0.08	0.64 ± 0.07	0.10 ± 0.05
		Scan 2	0.19 ± 0.09	0.65 ± 0.06	0.09 ± 0.04
Healthy Volunteer 4	Genu CC	Scan 1	0.11 ± 0.10	0.52 ± 0.11	0.14 ± 0.15
		Scan 2	0.12 ± 0.10	0.53 ± 0.10	0.14 ± 0.16
	Splenium CC	Scan 1	0.11 ± 0.10	0.56 ± 0.09	0.12 ± 0.14
		Scan 2	0.11 ± 0.10	0.57 ± 0.09	0.11 ± 0.11
	Anterior limb IC	Scan 1	0.16 ± 0.10	0.55 ± 0.07	0.06 ± 0.05
		Scan 2	0.16 ± 0.10	0.56 ± 0.07	0.05 ± 0.04
	Posterior limb IC	Scan 1	0.15 ± 0.07	0.62 ± 0.07	0.09 ± 0.05
		Scan 2	0.15 ± 0.07	0.64 ± 0.07	0.08 ± 0.04
p-value	Genu of Corpus Callosum		0.3910	0.6376	0.1411
	Splenium of Corpus Callosum		//	0.1817	0.2522
	Anterior limb of Internal Capsule		0.3910	0.0577	0.2522
	Posterior limb of Internal Capsule		0.3910	0.3189	0.3120
Bland-Altman Bias	Genu CC		0.0025	0.005	−0.0125
	Splenium CC		0	0.005	−0.010
	Anterior limb IC		0.0025	0.0125	−0.010
	Posterior limb IC		0.0025	0.0075	−0.0125
RC	Genu CC		0.0075	0.010	−0.0025
	Splenium CC		0	0.010	0
	Anterior limb IC		0.0075	0.0175	0
	Posterior limb IC		0.0075	0.0175	0.005
95% CI	Genu CC		0-0.0075	−0.005-0.01	−0.025- − 0.0025
	Splenuim CC		0-0	0-0.01	−0.0225-0
	Anterior limb IC		0-0.0075	0.01-0.0175	−0.0225-0
	Posterior limb IC		0-0.0075	−0.005-0.0175	−0.0325-0.005

confidence interval. All of these results contribute to ensuring the consistency of the OD index in time, stating that no significant difference between the two scanned is detected.

The values obtained for ICVF are very close to the intra-cellular volume fraction values of the Bingham-NODDI model, reported in Table 7.2. This result proves the agreement between the two formulations of the NODDI model. In the case of ICVF, the results are also consistent over time, with p-values of the paired t-test higher than the significant level of 0.05. Moreover, the Bland-Altman analysis revealed a bias, so the average difference between the two scans, very close to zero, indicating no significant difference between the two scans. In addition, a very low repeatability coefficient was obtained together with a narrow 95% confidence interval, ensuring the repeatability of the results over time.

Similarly, the very low ISOVF values obtained in white matter prove that in white matter intercellular water is very rare, a result already obtained with the analysis of the Bingham-NODDI model. Also in the case of the ISOVF, the results are stable in time, with p-values way greater than the significant level. The stability over time of the ISOVF is also confirmed by the outcomes of the Bland-Altman analysis, which resulted in small Bland-Altman bias, small repeatability coefficient and narrow 95% confidence interval.

The same study is carried out in grey matter, with the results extracted from the Thalamus, Caudate, and Putamen. Table 7.5 displays the results.

The first distinction between grey and white matter is the substantially higher OD, which highlights the greater dispersion or spread of neurite orientations within grey matter. This indicates that the neurites are misaligned and oriented in different directions, indicating a more complicated and disorganised neurite structure. Overall, the OD is characterised by great stability in time, with p-values of the paired t-test much higher than 0.05. Moreover, the Bland-Altman bias and the repeatability coefficient are close to zero in all the ROIs, indicating a notable stability of the OD index in time.

In addition to the OD, the ICVF presents with a lower value in grey matter with respect to white matter, indicating a lower neurite density in this tissue type. On the other hand, the ICVF results are stable in time with a p-value greater than 0.05 in all the ROIs. The consistency of the ICVF is also confirmed by the Bland-Altmann analysis outcomes, with low biases and repeatability coefficients in all the ROIs. Finally, the ISOVF has also been analysed, resulting in very low values in grey matter. These values are characterised by a high standard deviation, probably indicating that the CSF signal in grey matter is only given by noise. This evidences the absence of fluid and extracellular water in this tissue type. Despite its high standard deviation, also the ISOVF presents with a very low variability in time, allowing to conclude that all the AMICO-NODDI metrics exhibit great stability and consistency in time.

This investigation demonstrated the AMICO-NODDI model's consistency, stability, and repeatability across time. This finding has important implications for neuroimaging research and clinical applications. A stable AMICO-NODDI model assures that changes in neurite density and orientation dispersion in different brain areas properly represent real biological variations rather than measurement noise. This characteristic is crucial for longitudinal research in which measuring changes in brain microstructure over time is critical, particularly in ageing, disease progression, and treatment response contexts. Furthermore, the consistency of AMICO-NODDI measurements improves study reproducibility, allowing for partnerships across labs and institutions while also adding to the overall robustness of neuroimaging investigations.

Table 7.5: AMICO-NODDI model results for the four healthy volunteers in grey matter. The table shows the AMICO-NODDI metrics in grey matter together with the p-value from the paired t-test, the Bland-Altman Bias, the repeatability coefficient (RC) and the 95% confidence interval (CI) to assess the reproducibility of the results over time.

AMICO-NODDI model – White matter					
			OD	ICVF	ISOVF
Healthy Volunteer 1	Thalamus	Scan 1	0.31 ± 0.07	0.41 ± 0.06	0.08 ± 0.12
		Scan 2	0.31 ± 0.08	0.43 ± 0.07	0.10 ± 0.13
	Caudate	Scan 1	0.50 ± 0.12	0.35 ± 0.05	0.13 ± 0.16
		Scan 2	0.49 ± 0.12	0.36 ± 0.05	0.12 ± 0.14
	Putamen	Scan 1	0.49 ± 0.14	0.40 ± 0.05	0.02 ± 0.03
		Scan 2	0.48 ± 0.15	0.42 ± 0.05	0.02 ± 0.02
Healthy Volunteer 2	Thalamus	Scan 1	0.33 ± 0.08	0.44 ± 0.08	0.12 ± 0.18
		Scan 2	0.33 ± 0.07	0.44 ± 0.07	0.10 ± 0.15
	Caudate	Scan 1	0.49 ± 0.12	0.37 ± 0.08	0.22 ± 0.24
		Scan 2	0.48 ± 0.12	0.36 ± 0.08	0.21 ± 0.24
	Putamen	Scan 1	0.51 ± 0.12	0.44 ± 0.05	0.01 ± 0.02
		Scan 2	0.52 ± 0.12	0.44 ± 0.05	0.01 ± 0.02
Healthy Volunteer 3	Thalamus	Scan 1	0.29 ± 0.07	0.41 ± 0.06	0.05 ± 0.08
		Scan 2	0.30 ± 0.08	0.42 ± 0.06	0.06 ± 0.09
	Caudate	Scan 1	0.48 ± 0.12	0.34 ± 0.06	0.06 ± 0.09
		Scan 2	0.49 ± 0.12	0.35 ± 0.06	0.06 ± 0.09
	Putamen	Scan 1	0.54 ± 0.13	0.40 ± 0.04	0.02 ± 0.03
		Scan 2	0.53 ± 0.13	0.41 ± 0.05	0.01 ± 0.02
Healthy Volunteer 4	Thalamus	Scan 1	0.31 ± 0.06	0.41 ± 0.07	0.07 ± 0.11
		Scan 2	0.31 ± 0.07	0.42 ± 0.07	0.07 ± 0.11
	Caudate	Scan 1	0.46 ± 0.11	0.33 ± 0.06	0.15 ± 0.19
		Scan 2	0.46 ± 0.10	0.34 ± 0.06	0.15 ± 0.18
	Putamen	Scan 1	0.50 ± 0.14	0.40 ± 0.04	0.01 ± 0.02
		Scan 2	0.49 ± 0.14	0.42 ± 0.05	0.02 ± 0.03
p-value	Thalamus		0.3910	0.0917	0.7888
	Caudate		0.6376	0.3910	0.1817
	Putamen		0.3910	0.0796	1.000
Bland-Altman Bias	Thalamus		0.0025	0.0100	0.0025
	Caudate		−0.0025	0.005	−0.005
	Putamen		−0.005	0.0125	0
RC	Thalamus		0.0075	0.0175	0.015
	Caudate		0.005	0.0100	0
	Putamen		0.005	0.0200	0.0075
95% CI	Thalamus		0-0.0075	0.0025-0.0175	−0.0126-0.015
	Caudate		−0.01-0.0075	−0.005-0.01	−0.01-0
	Putamen		−0.01-0.005	0.005-0.02	−0.0075-0.0075

7.4 Impact of the hydration level of the participant

In order to understand whether the hydration level of the participant could influence in any way the outcome of the analysis, a final study was carried out on a single healthy volunteer. The participant underwent a first scan after fasting and refraining from drinking water during the night before. The acquisition protocol is the same used for the other

participants. After the first scan, the volunteer was given 500 mL of water and, after waiting roughly 10 minutes, a second scan was performed. The acquired data was then fit to the Tensor and NODDI models, both in the Bignham and AMICO formulations.

The results of the Tensor model are presented in Table 7.6. This table shows the FA and MD values extracted from the Corpus Callosum, Thalamus and Ventricles. As can be clearly observed, no difference between the dehydrated and hydrated states can be appreciated. This result brings to the conclusion that the Tensor model metrics are not influenced by the hydration level of a healthy participant.

Table 7.6: Tensor model results for the hydration study. The table shows the FA and MD results in the case of the single healthy volunteers who underwent a first scan in a dehydration state, and a second scan after drinking 500 mL of water.

Tensor model – Hydration study			
		FA	MD ($\cdot 10^{-3}\,\mathrm{mm}^2/\mathrm{s}$)
Corpus Callosum	Dehydrated	0.66 ± 0.16	0.58 ± 0.09
	Hydrated	0.65 ± 0.17	0.59 ± 0.12
Thalamus	Dehydrated	0.30 ± 0.06	0.58 ± 0.04
	Hydrated	0.31 ± 0.06	0.58 ± 0.04
Ventricles	Dehydrated	0.22 ± 0.10	1.67 ± 0.29
	Hydrated	0.22 ± 0.11	1.73 ± 0.33

The analysis of the Bingham-NODDI model results, under different hydration levels, are presented in Table 7.7. The model was fitted to the data acquired from a healthy volunteer in both dehydrated and hydrated states. The results demonstrate that the hydration level of the participant does not have any significant impact on the model's performance, as there is no noticeable difference between the first and second scans. This finding suggests that the Bingham-NODDI model is robust enough to provide accurate results regardless of the hydration level of the participant. Thus, these results highlight the potential of the Bingham-NODDI model as a valuable tool for investigating brain function and pathology in a variety of contexts.

Table 7.7: Bingham-NODDI model results for the hydration study. The table shows the Bingham-NODDI metrics in the case of the healthy volunteer who underwent two scans: the first in a dehydration condition while the second after drinking 500 mL of water.

Bingham-NODDI model – Hydration study							
		β-fraction	ODI	Tissue v.f.	Intra-neurite v.f.	R^2	MSE
Genu CC	Dehydrated	0.5 ± 0.2	0.14 ± 0.07	0.92 ± 0.10	0.58 ± 0.07	0.82 ± 0.07	0.013 ± 0.006
	Hydrated	0.5 ± 0.3	0.14 ± 0.08	0.93 ± 0.10	0.57 ± 0.09	0.82 ± 0.08	0.012 ± 0.006
Splenium CC	Dehydrated	0.5 ± 0.3	0.14 ± 0.09	0.91 ± 0.10	0.63 ± 0.07	0.80 ± 0.08	0.014 ± 0.007
	Hydrated	0.5 ± 0.3	0.14 ± 0.08	0.90 ± 0.13	0.63 ± 0.07	0.81 ± 0.08	0.014 ± 0.007
Anterior limb IC	Dehydrated	0.4 ± 0.3	0.21 ± 0.09	0.94 ± 0.05	0.62 ± 0.08	0.85 ± 0.06	0.009 ± 0.005
	Hydrated	0.4 ± 0.3	0.20 ± 0.09	0.95 ± 0.04	0.61 ± 0.07	0.86 ± 0.06	0.009 ± 0.004
Posterior limb IC	Dehydrated	0.5 ± 0.2	0.19 ± 0.09	0.92 ± 0.04	0.69 ± 0.07	0.82 ± 0.06	0.011 ± 0.004
	Hydrated	0.6 ± 0.3	0.18 ± 0.09	0.92 ± 0.03	0.69 ± 0.06	0.83 ± 0.06	0.011 ± 0.005
Thalamus	Dehydrated	0.58 ± 0.19	0.28 ± 0.08	0.96 ± 0.09	0.47 ± 0.05	0.93 ± 0.02	0.004 ± 0.001
	Hydrated	0.6 ± 0.2	0.28 ± 0.07	0.97 ± 0.07	0.47 ± 0.05	0.94 ± 0.02	0.0033 ± 0.0009
Caudate	Dehydrated	0.62 ± 0.19	0.48 ± 0.12	0.94 ± 0.12	0.46 ± 0.07	0.96 ± 0.02	0.002 ± 0.001
	Hydrated	0.61 ± 0.19	0.51 ± 0.12	0.96 ± 0.08	0.46 ± 0.06	0.96 ± 0.01	0.0021 ± 0.0007
Putamen	Dehydrated	0.53 ± 0.18	0.50 ± 0.12	0.99 ± 0.01	0.51 ± 0.04	0.94 ± 0.03	0.004 ± 0.002
	Hydrated	0.5 ± 0.2	0.54 ± 0.13	0.99 ± 0.02	0.50 ± 0.03	0.95 ± 0.02	0.003 ± 0.001

Similarly, Table 7.8 show the results of the AMICO-NODDI model in the case of the

hydration study. In particular, the table is useful to compare the results obtained in the dehydrated state of the participant and the ones obtained after letting the volunteer drink 500 mL of water. Also in the case of the AMICO-NODDI model, no variation is observed between the first and second scans, bringing to the conclusion that the linear formulation of the NODDI model is robust to different hydration levels in healthy subjects.

Table 7.8: AMICO-NODDI model results for the hydration study. The table shows the AMICO-NODDI metrics in the case of the healthy volunteer who underwent two scans: the first in a dehydration condition while the second after drinking 500 mL of water.

AMICO-NODDI model – Hydration study				
		OD	ICVF	ISOVF
Genu CC	Dehydrated	0.11 ± 0.08	0.62 ± 0.09	0.10 ± 0.10
	Hydrated	0.11 ± 0.08	0.60 ± 0.11	0.10 ± 0.11
Splenium CC	Dehydrated	0.11 ± 0.09	0.68 ± 0.10	0.12 ± 0.10
	Hydrated	0.11 ± 0.08	0.69 ± 0.09	0.13 ± 0.13
Anterior limb IC	Dehydrated	0.15 ± 0.10	0.63 ± 0.09	0.05 ± 0.05
	Hydrated	0.15 ± 0.10	0.62 ± 0.09	0.05 ± 0.04
Posterior limb IC	Dehydrated	0.17 ± 0.09	0.70 ± 0.08	0.08 ± 0.05
	Hydrated	0.16 ± 0.08	0.70 ± 0.07	0.08 ± 0.04
Thalamus	Dehydrated	0.31 ± 0.07	0.45 ± 0.06	0.07 ± 0.12
	Hydrated	0.30 ± 0.07	0.45 ± 0.06	0.06 ± 0.10
Caudate	Dehydrated	0.50 ± 0.11	0.38 ± 0.06	0.13 ± 0.19
	Hydrated	0.52 ± 0.10	0.37 ± 0.05	0.11 ± 0.14
Putamen	Dehydrated	0.50 ± 0.14	0.46 ± 0.05	0.01 ± 0.02
	Hydrated	0.52 ± 0.15	0.44 ± 0.05	0.01 ± 0.02

In conclusion, the hydration study demonstrates that diffusion MRI analysis using the Tensor, Bingham-NODDI, and AMICO-NODDI models is robust and unaffected by changes in the hydration level of healthy subjects. This has significant implications for both clinical and research applications, as it guarantees the consistency of these models in analysing brain microstructure across situations. These findings highlight their potential for neurological investigations and imply that they can be used confidently in clinical settings, contributing to more accurate assessments of brain health and pathology in various medical diseases. Future studies may explore broader applications and extreme hydration conditions for further validation.

Conclusions

This thesis is the result of the work carried out at the Oxford Centre for Clinical Magnetic Resonance Research (OCMR) - University of Oxford. The purpose of this study was to assess the consistency and repeatability of the NODDI (neurite orientation dispersion and density imaging) model over time, which is a useful diffusion MRI technique for estimating the microstructural complexity of dendrites and axons *in vivo* on clinical magnetic resonance scanners. In particular, the study examined the Bingham-NODDI model, which employs the Bingham distribution to model the neurite dispersion, and the AMICO-NODDI model, a linear implementation of the NODDI model which requires much less time to fit the diffusion data compared to its original formulation.

To assess the repeatability of the results, the study employed two DTI phantoms that mimic restricted anisotropic diffusion in the brain, in particular in white matter, also in the case of crossing fibres. The two phantoms, described in Section 3.1, were scanned four times on different days, over a period of a month, with the acquisition protocol described in Section 3.3. The acquired diffusion data were then fitted with the tensor, Bingham-NODDI and AMICO-NODDI models, and the final results were extracted from ROIs contoured onto the quantitative maps. The ROIs are shown in Figure 5.2a and 5.2b. To assess the stability of the obtained results over time, the coefficient of variation (CV) was computed considering the mean and standard deviation of the four acquisitions. This was performed for every diffusion metric of the models taken into account.

The final results of the two phantom cases are presented in Chapter 6. The models considered in the analysis include the Tensor model, the Bingham-NODDI, and the AMICO-NODDI model, which have all proven to be stable and repeatable. The consistency of the models is highlighted by the very low coefficients of variation obtained for all the metrics characterising each model, indicating that there is no significant variation in the analysed metrics between the four scans of the DTI phantoms. These findings confirm the robustness of the NODDI methodology and its suitability for longitudinal studies.

This study also aimed to investigate the stability of the NODDI model over time and determine if repetitive data acquisitions could impact measurement accuracy. The focus was on whether the heating of the magnetic field gradient coil after several acquisitions affected the results. To test this, phantoms were scanned eight times consecutively. The results demonstrated remarkable stability of the Tensor and NODDI models, despite the heating of the magnetic field gradient coils. There are several reasons why this is highly important. Firstly, in neuroimaging studies, it's crucial to ensure that the data obtained is both reliable and reproducible. If the NODDI parameters were affected by magnetic field gradient coil heating, it would lead to inconsistent measurements across scans, ultimately resulting in unreliable results. However, the stability of NODDI parameters under such conditions ensures that accurate interpretations and comparisons can be made with confidence, either between different subjects or time points. Furthermore, stability in varying situations might lead to more efficient resource utilisation, such as MRI scanner time. Researchers and physicians can run more scans in the same amount of time without sacrificing data quality, increasing data acquisition efficiency.

In addition to the phantom study, four healthy volunteers were scanned twice with the final aim of assessing the stability of the NODDI model over time, also in *in vivo* acquisitions. Each volunteer was scanned twice, with a 10-minute break in between the two scans. In the case of the *in vivo* acquisitions, a statistical analysis was performed to assess whether a significant variation in the results between the two measurements for each participant was observed. The obtained results are presented in Chapter 7.

The obtained results are associated with p-values of the paired t-test that are way above the significant threshold of 0.05. This implies that the null hypothesis H_0 cannot be rejected, meaning that there is no statistically significant difference between the values obtained in the first and second acquisitions, ensuring the consistency and stability of the Tensor and NODDI models, both in the Bignham and AMICO formulations. In addition to the paired t-test, the Bland-Altman analysis was carried out to compare the measurements obtained from the two scans. The analysis resulted in low Bland-Altman biases and repeatability coefficients close to zero, reinforcing the consistency of the NODDI model over time.

Moreover, a final study was performed to assess whether the hydration state of the participant could affect in any way the NODDI metrics, possibly cofounding the final results. Thus, a single healthy volunteer was scanned twice: the first time in a dehydrated condition, after fasting and refraining from drinking water all night, while the second scan was performed after letting the participant drink 500 mL of water. The results show no variation between the two scans, bringing to the conclusion that the hydration state of a healthy participant does not influence in any way the NODDI metrics. However, this result was obtained with just one volunteer. Thus, a deeper study needs to be carried out in order to better understand whether the hydration state of the participant does not really affect the analysis results.

The consistency of the measures contributes to the growing body of evidence proving the applicability of NODDI in various research and clinical applications. This stability is crucial for detecting changes in brain structure over time and making informed patient care decisions. Additionally, it enhances the credibility of NODDI as a tool, making it more valuable for understanding complex brain processes. In summary, the consistent NODDI results ensure its reliability and promise to expand knowledge of brain health and illness. This advancement has the potential to improve patient care and increase the accuracy of research findings. The consistent, reliable nature of the NODDI methodology will continue to contribute to the growth of knowledge in the field of neuroscience and open new avenues for exploration.

In conclusion, this study represents a comprehensive exploration of the NODDI model's consistency, stability, and robustness. The research has not only confirmed the reliability of the Tensor, Bingham-NODDI, and AMICO-NODDI models through phantom and *in vivo* acquisitions but has also shed light on the potential impact of participant hydration on NODDI metrics, reassuring its applicability in diverse research and clinical scenarios. The remarkable stability observed, even in the face of challenges such as magnetic field gradient coil heating and participant hydration differences, demonstrates the reliability of the NODDI framework. Its reliability serves as a solid foundation for detecting minor changes in brain microstructure over time, giving physicians and researchers the confidence they need to make appropriate decisions. Additionally, NODDI's growing legitimacy as a versatile tool for understanding the complexities of the human brain increases its importance in both neuroscience and therapeutic practice. The next stage in the research will be to undertake a multi-centre study to see how different MRI scanners produce varied outcomes. This project will validate the NODDI approach, also in the case different scanners are used, potentially leading to slightly different results. If successful, this study may lead to the integration of phantoms into a calibration protocol. Such a protocol would ensure consistent results across different MRI scanners, transcending the boundaries of individual equipment and opening new possibilities for collaborative research and clinical

applications.

Bibliography

[1] E.M. Haacke et al. *Magnetic Resonance Imaging: Physical Principles and Sequence Design*. Wiley, 1999. ISBN: 9780471351283. URL: https://books.google.it/books?id=BnOvQgAACAAJ.

[2] W. D. Foltz and D. A. Jaffray. "Principles of Magnetic Resonance Imaging". In: *Radiation Research* 177.4 (2012), pp. 331–348. DOI: 10.1667/RR2620.1. URL: https://doi.org/10.1667/RR2620.1.

[3] Peter J. Basser. "Inferring microstructural features and the physiological state of tissues from diffusion-weighted images". In: *NMR in Biomedicine* 8 (1995). URL: https://api.semanticscholar.org/CorpusID:28483431.

[4] P.J. Basser, J. Mattiello, and D. Lebihan. "Estimation of the Effective Self-Diffusion Tensor from the NMR Spin Echo". In: *Journal of Magnetic Resonance, Series B* 103.3 (1994), pp. 247–254. ISSN: 1064-1866. DOI: https://doi.org/10.1006/jmrb.1994.1037. URL: https://www.sciencedirect.com/science/article/pii/S1064186684710375.

[5] PJ Basser, J Mattiello, and D LeBihan. "MR diffusion tensor spectroscopy and imaging". In: *Biophysical journal* 66.1 (Jan. 1994), pp. 259–267. ISSN: 0006-3495. DOI: 10.1016/s0006-3495(94)80775-1.

[6] Carlo Pierpaoli et al. "Water Diffusion Changes in Wallerian Degeneration and Their Dependence on White Matter Architecture". In: *NeuroImage* 13.6 (2001), pp. 1174–1185. ISSN: 1053-8119. DOI: https://doi.org/10.1006/nimg.2001.0765. URL: https://www.sciencedirect.com/science/article/pii/S1053811901907657.

[7] C Pierpaoli et al. "Diffusion tensor MR imaging of the human brain." In: *Radiology* 201.3 (1996). PMID: 8939209, pp. 637–648. DOI: 10.1148/radiology.201.3.8939209. eprint: https://doi.org/10.1148/radiology.201.3.8939209. URL: https://doi.org/10.1148/radiology.201.3.8939209.

[8] Hui Zhang et al. "NODDI: Practical in vivo neurite orientation dispersion and density imaging of the human brain". In: *NeuroImage* 61.4 (2012), pp. 1000–1016. ISSN: 1053-8119. DOI: https://doi.org/10.1016/j.neuroimage.2012.03.072. URL: https://www.sciencedirect.com/science/article/pii/S1053811912003539.

[9] Maira Tariq et al. "Bingham–NODDI: Mapping anisotropic orientation dispersion of neurites using diffusion MRI". In: *NeuroImage* 133 (2016), pp. 207–223. ISSN: 1053-8119. DOI: https://doi.org/10.1016/j.neuroimage.2016.01.046. URL: https://www.sciencedirect.com/science/article/pii/S1053811916000616.

[10] EV Sullivan et al. "Equivalent disruption of regional white matter microstructure in ageing healthy men and women". In: *Neuroreport* 12.1 (Jan. 2001), pp. 99–104. ISSN: 0959-4965. DOI: 10.1097/00001756-200101220-00027.

[11] Uzma Zahid et al. "Impact of physiological factors on longitudinal structural MRI measures of the brain". In: *Psychiatry Research: Neuroimaging* 321 (2022), p. 111446. ISSN: 0925-4927. DOI: https://doi.org/10.1016/j.pscychresns.2022.111446. URL: https://www.sciencedirect.com/science/article/pii/S0925492722000075.

[12] Lejian Huang et al. "Reproducibility of Structural, Resting-State BOLD and DTI Data between Identical Scanners". In: *PLOS ONE* 7.10 (Oct. 2012), pp. 1–8. DOI: 10.1371/journal.pone.0047684. URL: https://doi.org/10.1371/journal.pone.0047684.

[13] Xiaopeng Zhou et al. "Scan-rescan repeatability and cross-scanner comparability of DTI metrics in healthy subjects in the SPRINT-MS multicenter trial". In: *Magnetic Resonance Imaging* 53 (2018), pp. 105–111. ISSN: 0730-725X. DOI: https://doi.org/10.1016/j.mri.2018.07.011. URL: https://www.sciencedirect.com/science/article/pii/S0730725X18303187.

[14] Ullamari Hakulinen et al. "Repeatability and variation of region-of-interest methods using quantitative diffusion tensor MR imaging of the brain". In: *BMC medical imaging* 12 (Oct. 2012), p. 30. DOI: 10.1186/1471-2342-12-30.

[15] E. M. Purcell, H. C. Torrey, and R. V. Pound. "Resonance Absorption by Nuclear Magnetic Moments in a Solid". In: *Phys. Rev.* 69 (1-2 Jan. 1946), pp. 37–38. DOI: 10.1103/PhysRev.69.37. URL: https://link.aps.org/doi/10.1103/PhysRev.69.37.

[16] I. I. Rabi et al. "A New Method of Measuring Nuclear Magnetic Moment". In: *Phys. Rev.* 53 (4 Feb. 1938), pp. 318–318. DOI: 10.1103/PhysRev.53.318. URL: https://link.aps.org/doi/10.1103/PhysRev.53.318.

[17] F. Bloch. "Nuclear Induction". In: *Phys. Rev.* 70 (7-8 Oct. 1946), pp. 460–474. DOI: 10.1103/PhysRev.70.460. URL: https://link.aps.org/doi/10.1103/PhysRev.70.460.

[18] Liang Xu et al. "Application of nuclear magnetic resonance technology in geologic carbon dioxide utilization and storage: A review". In: *Journal of Rock Mechanics and Geotechnical Engineering* 11 (Jan. 2019), pp. 1–12. DOI: 10.1016/j.jrmge.2019.01.003.

[19] Cyrus Eierud. *Dissertation: Developing Neuroimaging Methods to Disentangle Mild Traumatic Brain Injury*. June 2014.

[20] *MRI Basics*. URL: https://case.edu/med/neurology/NR/MRI%20Basics.htm.

[21] Ferruccio Balestra et al. "$\overline{p}^4He$ reaction cross section at 610 MeV/c". In: (July 2023).

[22] Anil Kumar, Dieter Welti, and Richard R Ernst. "NMR Fourier zeugmatography". In: *Journal of Magnetic Resonance (1969)* 18.1 (1975), pp. 69–83. ISSN: 0022-2364. DOI: https://doi.org/10.1016/0022-2364(75)90224-3. URL: https://www.sciencedirect.com/science/article/pii/0022236475902243.

[23] Jason Filos. "Parallel Transmission MRI". PhD thesis. Oct. 2008.

[24] P. Mukherjee et al. "Diffusion Tensor MR Imaging and Fiber Tractography: Theoretic Underpinnings". In: *American Journal of Neuroradiology* 29.4 (2008), pp. 632–641. ISSN: 0195-6108. DOI: 10.3174/ajnr.A1051. eprint: https://www.ajnr.org/content/29/4/632.full.pdf. URL: https://www.ajnr.org/content/29/4/632.

[25] Andrew L. Alexander et al. "Diffusion Tensor Imaging of the Brain". In: *Neurotherapeutics: The Journal of the American Society for Experimental NeuroTherapeutics* 4 (2007), pp. 316–329.

[26] Bryan Kolb abd Ian Q. Whishaw. *Fundamentals of Human Neuropsychology*. Worth Publishers, 2008. ISBN: 978-0-7167-9586-5.

[27] P Douek et al. "MR color mapping of myelin fiber orientation". In: *Journal of computer assisted tomography* 15.6 (1991), pp. 923–929. ISSN: 0363-8715. DOI: 10.1097/00004728-199111000-00003.

[28] Lauren O'Donnell and Carl-Fredrik Westin. "An Introduction to Diffusion Tensor Image Analysis". In: *Neurosurgery clinics of North America* 22 (Apr. 2011), pp. 185–96, viii. DOI: 10.1016/j.nec.2010.12.004.

[29] D Le Bihan et al. "Diffusion tensor imaging: concepts and applications". In: *Journal of magnetic resonance imaging : JMRI* 13.4 (Apr. 2001), pp. 534–546. ISSN: 1053-1807. DOI: 10.1002/jmri.1076.

[30] Cheng Koay et al. "A unifying theoretical and algorithmic framework for least squares methods of estimation in diffusion tensor imaging". In: *Journal of magnetic resonance (San Diego, Calif. : 1997)* 182 (Oct. 2006), pp. 115–25. DOI: 10.1016/j.jmr.2006.06.020.

[31] Alexander AL et al. "A geometric analysis of diffusion tensor measurements of the human brain". In: *Magnetic resonance in medicine* 44.2 (2000), pp. 283–291. DOI: 10.1002/1522-2594(200008)44:2<283::aid-mrm16>3.0.co;2-v.

[32] Susumu Mori and Jiangyang Zhang. "Principles of diffusion tensor imaging and its applications to basic neuroscience research". In: *Neuron* 51.5 (2006), pp. 527–539. DOI: 10.1016/j.neuron.2006.08.012.

[33] E. O. Stejskal and J. E. Tanner. "Spin Diffusion Measurements: Spin Echoes in the Presence of a Time-Dependent Field Gradient". In: *The Journal of Chemical Physics* 42.1 (July 2004), pp. 288–292. ISSN: 0021-9606. DOI: 10.1063/1.1695690. eprint: https://pubs.aip.org/aip/jcp/article-pdf/42/1/288/11154285/288_1_online.pdf. URL: https://doi.org/10.1063/1.1695690.

[34] Carlo Pierpaoli and Peter J. Basser. "Toward a quantitative assessment of diffusion anisotropy". In: *Magnetic Resonance in Medicine* 36.6 (1996), pp. 893–906. DOI: https://doi.org/10.1002/mrm.1910360612. eprint: https://onlinelibrary.wiley.com/doi/pdf/10.1002/mrm.1910360612. URL: https://onlinelibrary.wiley.com/doi/abs/10.1002/mrm.1910360612.

[35] David G. Norris. "Implications of bulk motion for diffusion-weighted imaging experiments: Effects, mechanisms, and solutions". In: *Journal of Magnetic Resonance Imaging* 13.4 (2001), pp. 486–495. DOI: https://doi.org/10.1002/jmri.1072. eprint: https://onlinelibrary.wiley.com/doi/pdf/10.1002/jmri.1072. URL: https://onlinelibrary.wiley.com/doi/abs/10.1002/jmri.1072.

[36] Robert Turner, Denis Le Bihan, and A. Scott Chesnicks. "Echo-planar imaging of diffusion and perfusion". In: *Magnetic Resonance in Medicine* 19.2 (1991), pp. 247–253. DOI: https://doi.org/10.1002/mrm.1910190210. eprint: https://onlinelibrary.wiley.com/doi/pdf/10.1002/mrm.1910190210. URL: https://onlinelibrary.wiley.com/doi/abs/10.1002/mrm.1910190210.

[37] Derek K. Jones and Mara Cercignani. "Twenty-five pitfalls in the analysis of diffusion MRI data". In: *NMR in Biomedicine* 23.7 (2010), pp. 803–820. DOI: https://doi.org/10.1002/nbm.1543. eprint: https://analyticalsciencejournals.onlinelibrary.wiley.com/doi/pdf/10.1002/nbm.1543. URL: https://analyticalsciencejournals.onlinelibrary.wiley.com/doi/abs/10.1002/nbm.1543.

[38] Jose Soares et al. "A hitchhiker's guide to diffusion tensor imaging". In: *Frontiers in Neuroscience* 7 (2013). ISSN: 1662-453X. DOI: 10.3389/fnins.2013.00031. URL: https://www.frontiersin.org/articles/10.3389/fnins.2013.00031.

[39] Jesper L.R. Andersson, Stefan Skare, and John Ashburner. "How to correct susceptibility distortions in spin-echo echo-planar images: application to diffusion tensor imaging". In: *NeuroImage* 20.2 (2003), pp. 870–888. ISSN: 1053-8119. DOI: https://doi.org/10.1016/S1053-8119(03)00336-7. URL: https://www.sciencedirect.com/science/article/pii/S1053811903003367.

[40] Stephen M. Smith et al. "Advances in functional and structural MR image analysis and implementation as FSL". In: *NeuroImage* 23 (2004). Mathematics in Brain Imaging, S208–S219. ISSN: 1053-8119. DOI: https://doi.org/10.1016/j.neuroimage.2004.07.051. URL: https://www.sciencedirect.com/science/article/pii/S1053811904003933.

[41] Jesper L.R. Andersson and Stamatios N. Sotiropoulos. "An integrated approach to correction for off-resonance effects and subject movement in diffusion MR imaging". In: *NeuroImage* 125 (2016), pp. 1063–1078. ISSN: 1053-8119. DOI: https://doi.org/10.1016/j.neuroimage.2015.10.019. URL: https://www.sciencedirect.com/science/article/pii/S1053811915009209.

[42] Mark Jenkinson et al. "FSL". In: *NeuroImage* 62.2 (2012). 20 YEARS OF fMRI, pp. 782–790. ISSN: 1053-8119. DOI: https://doi.org/10.1016/j.neuroimage.2011.09.015. URL: https://www.sciencedirect.com/science/article/pii/S1053811911010603.

[43] Nikos Evangelou et al. "Quantitative pathological evidence for axonal loss in normal appearing white matter in multiple sclerosis". In: *Annals of Neurology* 47.3 (2000), pp. 391–395. DOI: https://doi.org/10.1002/1531-8249(200003)47:3<391::AID-ANA20>3.0.CO;2-J. eprint: https://onlinelibrary.wiley.com/doi/pdf/10.1002/1531-8249%28200003%2947%3A3%3C391%3A%3AAID-ANA20%3E3.0.CO%3B2-J. URL: https://onlinelibrary.wiley.com/doi/abs/10.1002/1531-8249%28200003%2947%3A3%3C391%3A%3AAID-ANA20%3E3.0.CO%3B2-J.

[44] M.M. Paula-Barbosa et al. "Dendritic degeneration and regrowth in the cerebral cortex of patients with Alzheimer's disease". In: *Journal of the Neurological Sciences* 45.1 (1980), pp. 129–134. ISSN: 0022-510X. DOI: https://doi.org/10.1016/S0022-510X(80)80014-1. URL: https://www.sciencedirect.com/science/article/pii/S0022510X80800141.

[45] Chris A. Clark, Maj Hedehus, and Michael E. Moseley. "Diffusion time dependence of the apparent diffusion tensor in healthy human brain and white matter disease". In: *Magnetic Resonance in Medicine* 45.6 (), pp. 1126–1129. DOI: https://doi.org/10.1002/mrm.1149. eprint: https://onlinelibrary.wiley.com/doi/pdf/10.1002/mrm.1149. URL: https://onlinelibrary.wiley.com/doi/abs/10.1002/mrm.1149.

[46] Maira Tariq et al. “In vivo Estimation of Dispersion Anisotropy of Neurites Using Diffusion MRI”. In: 17 (Sept. 2014), pp. 241–8. DOI: 10.1007/978-3-319-10443-0_31.

[47] Kanti V. Mardia and Peter E. Jupp. *Directional Statistics*. Wiley series in probability and statistics., 1999. DOI: 10.1002/9780470316979.

[48] Rutger Fick. “Advanced dMRI Signal Modeling for Tissue Microstructure Characterization”. PhD thesis. Mar. 2017.

[49] Alessandro Daducci et al. “Accelerated Microstructure Imaging via Convex Optimization (AMICO) from diffusion MRI data”. In: *NeuroImage* 105 (2015), pp. 32–44. ISSN: 1053-8119. DOI: https://doi.org/10.1016/j.neuroimage.2014.10.026. URL: https://www.sciencedirect.com/science/article/pii/S1053811914008519.

[50] Frederik Bernd Laun, Sandra Huff, and Bram Stieltjes. “On the effects of dephasing due to local gradients in diffusion tensor imaging experiments: relevance for diffusion tensor imaging fiber phantoms”. In: *Magnetic Resonance Imaging* 27.4 (2009), pp. 541–548. ISSN: 0730-725X. DOI: https://doi.org/10.1016/j.mri.2008.08.011. URL: https://www.sciencedirect.com/science/article/pii/S0730725X08002920.

[51] Amir Moussavi-Biugui et al. “Novel spherical phantoms for Q-ball imaging under in vivo conditions”. In: *Magnetic Resonance in Medicine* 65.1 (2011), pp. 190–194. DOI: https://doi.org/10.1002/mrm.22602. eprint: https://onlinelibrary.wiley.com/doi/pdf/10.1002/mrm.22602. URL: https://onlinelibrary.wiley.com/doi/abs/10.1002/mrm.22602.

[52] Rutger H. J. Fick, Demian Wassermann, and Rachid Deriche. “The Dmipy Toolbox: Diffusion MRI Multi-Compartment Modeling and Microstructure Recovery Made Easy”. In: *Frontiers in Neuroinformatics* 13 (2019). ISSN: 1662-5196. DOI: 10.3389/fninf.2019.00064. URL: https://www.frontiersin.org/articles/10.3389/fninf.2019.00064.

[53] Mark W. Woolrich et al. “Bayesian analysis of neuroimaging data in FSL”. In: *NeuroImage* 45.1, Supplement 1 (2009). Mathematics in Brain Imaging, S173–S186. ISSN: 1053-8119. DOI: https://doi.org/10.1016/j.neuroimage.2008.10.055. URL: https://www.sciencedirect.com/science/article/pii/S1053811908012044.

[54] Mark Jenkinson and Stephen Smith. “A global optimisation method for robust affine registration of brain images”. In: *Medical Image Analysis* 5.2 (2001), pp. 143–156. ISSN: 1361-8415. DOI: https://doi.org/10.1016/S1361-8415(01)00036-6. URL: https://www.sciencedirect.com/science/article/pii/S1361841501000366.

[55] Mark Jenkinson et al. “Improved Optimization for the Robust and Accurate Linear Registration and Motion Correction of Brain Images”. In: *NeuroImage* 17.2 (2002), pp. 825–841. ISSN: 1053-8119. DOI: https://doi.org/10.1006/nimg.2002.1132. URL: https://www.sciencedirect.com/science/article/pii/S1053811902911328.

[56] Douglas N. Greve and Bruce Fischl. "Accurate and robust brain image alignment using boundary-based registration". In: *NeuroImage* 48.1 (2009), pp. 63–72. ISSN: 1053-8119. DOI: https://doi.org/10.1016/j.neuroimage.2009.06.060. URL: https://www.sciencedirect.com/science/article/pii/S1053811909006752.

[57] Jesper LR Andersson, Mark Jenkinson, Stephen Smith, et al. "Non-linear registration, aka Spatial normalisation FMRIB technical report TR07JA2". In: *FMRIB Analysis Group of the University of Oxford* 2.1 (2007), e21.

[58] Jesper LR Andersson, Mark Jenkinson, and Stephen Smith. "Non-linear optimisation. FMRIB technical report TR07JA1". In: *Practice* (2007).

[59] J. Martin Bland and DouglasG. Altman. "STATISTICAL METHODS FOR ASSESSING AGREEMENT BETWEEN TWO METHODS OF CLINICAL MEASUREMENT". In: *The Lancet* 327.8476 (1986). Originally published as Volume 1, Issue 8476, pp. 307–310. ISSN: 0140-6736. DOI: https://doi.org/10.1016/S0140-6736(86)90837-8. URL: https://www.sciencedirect.com/science/article/pii/S0140673686908378.

[60] Enrico Kaden et al. "Multi-compartment microscopic diffusion imaging". In: *NeuroImage* 139 (2016), pp. 346–359. ISSN: 1053-8119. DOI: https://doi.org/10.1016/j.neuroimage.2016.06.002. URL: https://www.sciencedirect.com/science/article/pii/S1053811916302063.